To the Graduate Council:

I am submitting herewith a dissertation written by Richard Earl Neese entitled "Surface Structure of Deformed Nuclei by Radial and Angular Localization in Heavy-Ion Scattering." I have examined the final copy of this dissertation for form and content and recommend that it be accepted in partial fulfillment of the requirements for the degree of Doctor of Philosophy, with a major in Physics.

M. W. Guidry, Major Professor

We have read this dissertation
and recommend its acceptance:

Carrol R. Bingham

Leo R. Riedinger

Joseph L. Fowler

Li-yang Lee

Noah R. Johnson

G. D. O'Kelley

Accepted for the Council:

Vice Chancellor
Graduate Studies and Research

SURFACE STRUCTURE OF DEFORMED NUCLEI BY RADIAL AND ANGULAR LOCALIZATION IN HEAVY-ION SCATTERING

A Dissertation

Presented for the

Doctor of Philosophy

Degree

The University of Tennessee, Knoxville

Richard Earl Neese

August 1981

3053635

ACKNOWLEDGMENTS

I wish to express my sincere thanks to a member of my thesis committee, Dr. L. L. Riedinger, who with his silver-tongued soliloquy on the "rolling hills of East Tennessee" seduced a young orphaned graduate student into leaving the urban jungle of Georgia Tech. But like many used-car salesmen, he failed to inform me of such important matters as midnight shifts, low-flying cream pies, and Dr. R. D. Present (the revered terror of certain preparatory courses for the dreaded preliminary exams). I survived the minor tribulations and came to appreciate Dr. Present as one of the most demanding, conscientious, and fair professors in my experience as a physics student. His course in electromagnetism is unparalleled anywhere.

I am especially grateful for the amazing abilities of the director of this research, Dr. M. W. Guidry. He provided an extremely interesting and challenging research topic, astounded me with his accurate prognostications of the results, and deeply ingrained in my mind the concept that "wishing does not make it so." Besides, he really always knew that I would eventually finish this project!

To the other members of my thesis committee, Dr. C. R. Bingham, Dr. J. L. Fowler, Dr. G. D. O'Kelley, Dr. N. R. Johnson, and Dr. I. Y. Lee, I extend my heartfelt appreciation for their participation in my development as a nuclear physicist. Often, they took time from playing with lasers, hunting for quarks, or gathering heavy ions two by two to assist me when the physics was more unclear than nuclear.

This research has involved a rather extensive collaboration. Dr. J. O. Rasmussen, a prime instigator of this research topic, on many occasions tendered advice essential to the conquest of impediments. In addition, he graciously supplied prints of some of the figures used in Chapter III. Dr. R. J. Donangelo, another of the founding fathers, played a very active role in the development of this research and kindly consented to read and offer comment on early versions of Chapters II through IV of this dissertation. Dr. G. R. Satchler proved to be a valuable source of information concerning nuclear potentials and related matters of nuclear structure. He generously provided several folding model calculations, as well as Figure II-5. Dr. M. J. Rhoades-Brown, a recent addition to the flock, contributed expertise in quantum-mechanical coupled-channels calculations and enthusiasm in ascertaining the true role and applicability of semiclassical methods and localization effects in heavy-ion collisions. Dr. R. M. Diamond, Dr. F. S. Stephens, and Dr. D. L. Hillis greatly facilitated the experiments at Lawrence Berkeley Laboratory (LBL) with their mastery of exotic local electronics and experimental arrangements.

I wish to express my respect for the operating staffs of the LBL 88" Cyclotron and the Oak Ridge Isochronous Cyclotron (ORIC) for their professional manner in dealing with a budding young nuclear physicist. In particular, a special thanks goes to Dr. D. C. Hensley of the ORIC staff for his digital wizardry which resulted in sorting programs that enabled analysis of the LBL data on the SEL 840-A computer at ORIC.

Dr. J. A. Vrba, my immediate doctoral predecessor from The University of Tennessee (UT) Nuclear Physics Group, is commended for his companionship on several midnight shifts, his remarkable rapport with uncooperative computers, and his valuable help in experimental matters. Dr. R. W. Lide and fellow graduate students T. L. Nichols, W. K. Luk, and R. S. Becker were a source of many jovial conversations near the office coffee pot on topics scientifical, computational, philosophical, and political.

I am indebted to Dr. W. M. Bugg, UT Physics Department Head, for a graduate teaching assistantship during my first year at UT. I gratefully acknowledge the support of the United States Department of Energy (USDOE) (under contract number DE-AS05-76ER04936) in the form of a graduate research assistantship during the remainder of my tenure at UT. As a guest assignee of Dr. N. R. Johnson, I was permitted access to the facilities at Oak Ridge National Laboratory (operated by Union Carbide Corporation under contract number W-7405-eng-26 for the USDOE).

I am particularly thankful for the friendly and helpful faculty and staff of the Physics Department at UT. Extra special thanks are extended to Mrs. Wylene Vrba, who on many occasions saved the day for a desperate graduate student to render him harmless instead of homicidal.

I wish to acknowledge use of the facilities of The University of Tennessee Computing Center. Although I cursed the DEC 10, and IBM 370/3031 often, they still did the bulk of the work of this dissertation, while I merely waited.

Mrs. Sally Nichols is commended for the excellent quality of the figures contained herein. Furthermore, the UT Photographic Center

deserves high marks for the excellent job done in producing prints of the figures. Mrs. Maxine Martin, my typist, is surely a saint and her hands should be blessed!

To those unnamed contributors to my growth as a scientist and person I offer my humble gratitude.

Finally and most importantly, I wish to express my deepest thanks to my closest friend, my wife Kathy-Jo, for her encouragement and support throughout all phases of this research. She always made me stop when I would not stop and would not let me quit when I wanted to quit. The sacrifice she made in companionship and the loneliness she suffered during my personal paper chase are astounding. She was always there, even though I was not.

ABSTRACT

Theoretical and experimental methods for studying heavy-ion inelastic scattering from deformed nuclei are described. The theoretical methods involve classical-limit approximations, while particle-γ-ray spectroscopy techniques are employed experimentally. With these approaches, heavy-ion excitation in the Coulomb-nuclear interference region acquires a transparent interpretation, despite the apparent complexity of the multistep excitation processes involved. Radial and angular localization effects in such collisions are discussed. The sensitivity of the inelastic scattering to details of the surface ion-ion potential due to radial and angular localization is exploited to introduce a method of determining the equipotential contours in a direct manner which bypasses particular model-dependent parametrizations. Adiabatic giant resonance polarization potentials are included explicitly in the prescription.

Experimental inelastic excitation functions for the scattering of ^{40}Ar projectiles from ^{156}Gd, ^{160}Gd, ^{162}Dy, ^{164}Dy, and ^{180}Hf are reported. Ion-ion potential contours for these systems are obtained with the aforementioned method. These contours agree well with calculations which employ deformed double-folding potentials and deformed proximity potentials. Electric quadrupole and hexadecapole moments deduced for ^{180}Hf disagree with previous Coulomb-excitation measurements with α-particle projectiles.

The examples discussed provide a good illustration of the relationship between classical and quantum physics. The general nature

of the localization effects for any system which has dynamical variables which take on large quantum numbers is emphasized.

TABLE OF CONTENTS

CHAPTER		PAGE
I.	INTRODUCTION	1
II.	NUCLEAR STRUCTURE AND HEAVY-ION INTERACTION POTENTIALS	6
	Sizes and Shapes	7
	Nuclear Ion-Ion Interaction Potentials	11
III.	CLASSICAL LIMIT S-MATRIX FORMALISM FOR COULOMB-NUCLEAR INTERFERENCE	23
	Model Assumptions and Coordinates	23
	CLSM Formalism	27
	General Effects of the Coulomb-Nuclear Interference	33
	Comparison of CLSM Calculations to Exact Quantum-Mechanical Coupled-Channels Calculations	44
IV.	LOCALIZATION EFFECTS IN HEAVY-ION COLLISIONS	50
	Radial Localization	50
	Angular Localization	53
V.	EXPERIMENTAL TECHNIQUES AND DATA REDUCTION	64
	The Particle-γ Coincidence Method	64
	The Experimental Excitation Probabilities	79
	The Experimental Excitation Functions	87
VI.	THE ION-ION INTERACTION POTENTIAL IN THE NUCLEAR SURFACE REGION	98
	Nuclear Charge Parameters	98
	Parametrization of the Nuclear Potential	104
	Equations of Motion	106
	Fits to the Experimental Excitation Functions	110
	The Global Ion-Ion Potentials	122
VII.	CONCLUSIONS AND SUGGESTIONS FOR FUTURE STUDY	134
BIBLIOGRAPHY		137
APPENDICES		144
A.	EFFECTIVE POLARIZATION POTENTIALS FOR ADIABATIC COULOMB COUPLING TO GIANT RESONANCES IN HEAVY-ION SCATTERING	145

PAGE

B. JUSTIFICATION FOR NEGLECTING TERMS DUE TO CHARGE DISTRIBUTION OVERLAP IN THE ELECTRIC INTERACTION POTENTIAL 160

C. THICK TARGET KINEMATICAL RELATIONS AND THE CALCULATED BACKSCATTERED HEAVY-ION SPECTRUM 171

D. SAFE-ENERGY FORMALISM 177

E. FEATURES OF THE CLSM COMPUTER CODE KULEXA 182

VITA 190

LIST OF TABLES

TABLE		PAGE
V-1.	Target and Beam-Energy Combinations Used in the Experiments	68
V-2.	Ge(Li) Detector Geometries Used in the Experiments	71
V-3.	The Transition Energies of the Ground-State Rotational Band for Each Rare-Earth Nucleus Studied	77
V-4.	The Isotopic Abundances a for the Targets Used in the Experiments	77
V-5.	Renormalization Factors for the Excitation Functions Determined for Each Experimental Run	92
V-6.	Experimental Excitation Probabilities for the $^{40}Ar + ^{156}Gd$ System	94
V-7.	Experimental Excitation Probabilities for the $^{40}Ar + ^{160}Gd$ System	95
V-8.	Experimental Excitation Probabilities for the $^{40}Ar + ^{162}Dy$ System	96
V-9.	Experimental Excitation Probabilities for the $^{40}Ar + ^{164}Dy$ System	97
V-10.	Experimental Excitation Probabilities for the $^{40}Ar + ^{180}HF$ System	97
VI-1.	Experimental Values of $\langle 0^+ \| \mathcal{M}(E\lambda) \| \lambda^+ \rangle$ and $Q_0^{(\lambda)}(\lambda = 2,4)$ for the Nuclei Studied	100
VI-2.	Best-Fit Parameters for the $^{40}Ar + ^{156}Gd$ Ion-Ion Potential	117
VI-3.	Best-Fit Parameters for the $^{40}Ar + ^{160}Gd$ Ion-Ion Potential	118
VI-4.	Best-Fit Parameters for the $^{40}Ar + ^{162}Dy$ Ion-Ion Potential	119
VI-5.	Best-Fit Parameters for the $^{40}Ar + ^{164}Dy$ Ion-Ion Potential	120
VI-6.	Best-Fit Parameters for the $^{40}Ar + ^{180}Hf$ Ion-Ion Potential	121

TABLE PAGE

VI-7. The Parameters $R_0(V)$, $\alpha_2(V)$, and $\alpha_4(V)$ for the Deformed Ion-Ion Potentials 129

B-1. Values of the Sum $R_1 + R_2$ and D_{min} for the Systems Studied 162

B-2. Parameters Used in the Double-Folding Calculation of Figures B-1 through B-3 165

LIST OF FIGURES

FIGURE		PAGE
II-1.	Plot of a Representative Nuclear Density Distribution . .	9
II-2.	Examples of Pure β_2, β_4, and β_6 Deformations	12
II-3.	The Shapes of Some Deformed Rare-Earth Nuclei	13
II-4.	Shapes of Some Deformed Actinide Nuclei	14
II-5.	Coordinates Used to Define the Double-Folding Potential .	20
III-1.	Coordinate System for Inelastic Backward Scattering from a Deformed Nucleus	25
III-2.	Plot of a Typical Quantum-Number Function	29
III-3.	Coulomb Excitation Probabilities versus Quadrupole Coupling Strength $\bar{q}_2$	34
III-4.	Schematic Illustration of Classical CNI	36
III-5.	Illustration of Classical Angular Momentum Transfer in CNI	37
III-6.	The Real Part of the Phase Difference $\Delta\Phi$ versus Final Spin I	38
III-7.	Excitation Functions for the $^{86}Kr + ^{232}Th$ System which Demonstrate the Simple Rule for Heavy-Ion CNI . . .	41
III-8.	Same as Figure III-7, Except for the $^{16}O + ^{162}Dy$ System	42
III-9.	Excitation Probabilities Calculated with the Potential Described by Eq. III-14	47
IV-1.	Schematic Illustration of Radial and Angular Localization in Heavy-Ion Collisions	54
IV-2.	Typical Plot of Excitation Probability P_I versus Final Spin I_f	56
IV-3.	Comparison of the J = 0 CLSM Excitation Probabilities Calculated for the Deformed Woods-Saxon Potential and the First-Order Expansion Potential	60

FIGURE PAGE

IV-4. Polar Plot of the Nuclear Potential Shapes Considered in the Calculations Presented in Figure IV-3 62

V-1. Schematic Diagram of the Experimental Arrangement 65

V-2. Schematic Diagram of the Scattering Chamber 66

V-3. The Scattering Chamber, Snout, and Beam-Line Plumbing for a Typical Experimental Configuration 67

V-4. Block Diagram of Typical Particle-γ Coincidence Electronics 70

V-5. Schematic Diagram of a Thick-Target Backscattered-Particle Spectrum 73

V-6. Examples of E_{det} versus E_{inc} Curves 74

V-7. Example of a Particle Detector Calibration Curve 76

V-8. Example of a Ge(Li) Detector Efficiency Calibration Curve 82

V-9. Example of Good Agreement between the Experimental Excitation Functions for the Three Ge(Li) Detectors . . . 88

V-10. Example Showing the Worst Case of Splitting of the Experimental Excitation Functions for the Three Ge(Li) Detectors 89

VI-1. Least-Squares Fit to the Experimental Population Signature of ^{180}Hf in the Coulomb Excitation Region . . . 103

VI-2. Fits to the Experimental Excitation Functions for the ^{40}Ar + ^{156}Gd System 112

VI-3. Same as Figure VI-2, Except for the ^{40}Ar + ^{160}Gd System 113

VI-4. Same as Figure VI-2, Except for the ^{40}Ar + ^{162}Dy System 114

VI-5. Same as Figure VI-2, Except for the ^{40}Ar + ^{164}Dy System 115

VI-6. Same as Figure VI-2, Except for the ^{40}Ar + ^{180}Hf System 116

VI-7. The Deformed Ion-Ion Potential Contours for ^{40}Ar + ^{156}Gd 123

FIGURE		PAGE
VI-8.	Same as Figure VI-7, Except for $^{40}Ar + ^{160}Gd$	124
VI-9.	Same as Figure VI-7, Except for $^{40}Ar + ^{162}Dy$	125
VI-10.	Same as Figure VI-7, Except for $^{40}Ar + ^{164}Dy$	126
VI-11.	Same as Figure VI-7, Except for $^{40}Ar + ^{180}Hf$	127
VI-12.	Comparison of Experimental Contours of the Ion-Ion Potential for $^{40}Ar + ^{160}Gd$ with Those Calculated Using a Deformed Folding Potential	132
VI-13.	Same as Figure VI-12, But for a Deformed Proximity Potential	133
A-1.	Simple Model of Giant Dipole Resonance Excitation	147
A-2.	The Induced Dipole Moment $\langle\vec{d}\rangle$ for an Axially Symmetric Deformed Nucleus in an External Homogeneous Electric Field $\vec{E}$	150
B-1.	Comparison of the $\lambda = 0$ Radial Dependence for the Fermi Double-Folding Expansion and the Multipole-Multipole Expansion	166
B-2.	The Same as Figure B-1 for $\lambda = 2$	167
B-3.	The Same as Figure B-1 for $\lambda = 4$	168
C-1.	Calculations of Backscattered Heavy-Ion Spectra for $^{40}Ar + ^{160}Gd$	176
D-1.	Schematic Diagram of the Model Used to Construct the Safe-Energy Formula	178
D-2.	Least-Squares Fit of Some Heavy-Ion Scattering Data to Eq. D-1	180

CHAPTER I

INTRODUCTION

Nuclear collisions can be categorized as (a) those restricted to the asymptotic region where charge and matter distributions do not overlap and Coulomb interactions dominate, (b) those occurring in an intermediate region where surface distributions overlap somewhat causing a sensitive interplay between Coulomb and nuclear interactions, and (c) those resulting in significant overlap where nuclear interactions dominate. The second region is a rich source of information on the tail of the nuclear interaction potential.

A significant amount of experimental and theoretical work has been discussed concerning inelastic scattering in the region where both Coulomb and nuclear forces make comparable contributions to the scattering process (the Coulomb-nuclear interference or CNI region). Most of this work has involved light ions (e.g., α-particles) on deformed targets, or light heavy ions (e.g., ^{16}O) on more spherical targets. In all of these cases the inelastic excitation is dominated by one- or two-step processes. Guidry et al. (1978a) reported the first CNI experiments using heavy ions on highly deformed target nuclei. In such cases, the large radial and angular momenta of the system, coupled with the deformation of the target nucleus, imply many contributing partial waves, appreciable rotational excitation, and the dominance of multistep processes in the scattering event. Most analyses of the previous CNI data have employed quantum-mechanical coupled-channel

or distorted-wave Born approximation (DWBA) descriptions. The CNI structure may then be interpreted in terms of interferences among amplitudes in a limited number of channels contributing to the excitation [see, e.g., Baker (1975)]. The proliferation of open channels for heavy ions on deformed targets due to multiple-step processes and a large number of contributing partial waves preclude a DWBA treatment and until recently made a quantum-mechanical coupled-channels analysis difficult. The development of highly accurate and efficient large-scale coupled-channel codes (Rhoades-Brown, Macfarlane, Pieper, 1980a, 1980b) has made a rigorous quantum-mechanical treatment of general heavy-ion scattering feasible. However, even though the coupled-channels calculations can be done, the large number of contributing amplitudes does not allow a simple interpretation of the excitation process. The development of the classical-limit S-matrix (CLSM) formalism [see Massmann and Rasmussen (1975), Donangelo et al. (1976), Guidry et al. (1976a, 1978b), and the more extensive references in Chapter III] first made tractable the analysis of inelastic scattering data for such systems. This approach provides simple and accurate semiclassical models for the excitation mechanism.

Heavy-ion inelastic scattering at energies near the Coulomb barrier leads to appreciable excitation of the ground-state rotational band for highly deformed nuclei. Large effects associated with interference between Coulomb and nuclear forces have been predicted (Guidry et al., 1976a) and observed (Guidry et al., 1978a) in such systems. The Coulomb part of this interaction is well understood, both experimentally (Ward et al., 1976; Guidry et al., 1976b) and theoretically (Massmann and Rasmussen, 1975; Guidry et al., 1978b). The

nuclear part is less well known, but is expected to be largely of a surface nature due to the short range of the nucleon-nucleon force and strong absorption in the nuclear interior. Investigations of CNI with the CLSM method suggest that (a) because both Coulomb and nuclear forces contribute to the excitation, CNI should probe both charge and mass parameters; (b) at energies below the barrier a relatively clean separation is possible between the effects due to the real and imaginary parts of the nuclear interaction potential; (c) the short de Broglie wavelength of the heavy-ion system implies a localization in the radial separation of the collision partners; and (d) the large transfer of angular momentum into rotational modes of the target nucleus implies a localization in the angular region of the deformed nuclear surface probed in the interaction. These observations imply that heavy-ion CNI should be an excellent probe of the deformed nuclear surface.

Traditional charged-particle spectroscopy is not feasible at present for these systems because of heavy-ion straggling and the close spacing of the low-lying rotational levels. As suggested previously (Guidry et al., 1976a) and demonstrated experimentally (Guidry et al., 1978a), particle-γ-spectroscopy techniques provide a relatively precise method whereby such processes may be studied.

The work described in this dissertation was divided into three related tasks.

1. A theoretical investigation of the radial and angular localization effects inherent in such heavy-ion collisions was conducted. This investigation verified the existence of radial and

angular localization effects as observable physical phenomena in heavy-ion scattering from highly deformed target nuclei. These effects are true physical phenomena and not traits dependent on particular treatments of the excitation (e.g., semiclassical or quantum-mechanical formalisms).

2. A technique which exploits radial and angular localization effects in such collisions within the framework of the CLSM formalism was developed to extract the ion-ion interaction potential in the nuclear surface region from CNI data. The extracted potentials are believed to be rather insensitive to particular parametrizations of the nuclear interaction potential and provide simple, accurate quantitative models of the inelastic excitation mechanism.

3. Experiments were performed using particle-γ spectroscopy for the systems $^{40}Ar + (^{156}Gd, ^{160}Gd, ^{162}Dy, ^{164}Dy, ^{180}Hf)$ at energies near the Coulomb barrier. The prescription mentioned above was applied to deduce equipotential contours of the surface ion-ion interaction for all five systems.

This dissertation is composed of seven chapters, of which this is the first, and five appendices. In Chapter II, brief overviews of nuclear size and shape measurements and some of the popular parametrizations of nuclear ion-ion interaction potentials are presented. Chapter III contains a discussion of the physical model used in the study, the fundamentals of the CLSM formalism, the salient features of heavy-ion CNI for such systems, and a comparison of the CLSM approach to a more rigorous quantum-mechanical coupled-channels method. The radial and angular localization effects are studied in detail in

Chapter IV. The experimental techniques are described, the data analysis is outlined, and the experimental inelastic excitation probabilities are reported in Chapter V. Chapter VI contains an explanation of the special analysis necessary for the $^{40}Ar + ^{180}Hf$ system, a development of the prescription used to extract the ion-ion interaction potentials, and applications of the method to the five systems, and a discussion of the experimental results. Chapter VII contains summary remarks and suggestions for future efforts. Appendix A provides derivations of the adiabatic giant resonance potentials included in the Hamiltonian of Chapter III. Appendix B is composed of a justification for neglecting corrections in the electric interaction potential used in the CLSM Hamiltonian which are caused by overlap of the charge distributions. Appendix C lists important thick-target kinematical relations and describes the method used to fit the heavy-ion backscatter spectrum. Appendix D summarizes a "safe energy" formalism developed in the course of this work. Finally, Appendix E describes important features of the CLSM computer code KULEXA.

CHAPTER II

NUCLEAR STRUCTURE AND HEAVY-ION INTERACTION POTENTIALS

Nearly seventy years ago Rutherford (1911) first proposed the existence of the atomic nucleus, described simply as (a) possessing sufficient positive charge to counterbalance the surrounding electronic charge, (b) exhibiting a diameter on the order of 10^{-12} cm, and (c) accounting for most of the atomic mass. Today the nucleus is envisioned as an ensemble of neutrons and protons, with free mesons and other subatomic particles playing rather minor roles in low-energy phenomena. Despite many attempts to divine the nuclear choreography in terms of basic interparticle interactions, at this writing no truly coherent quantum-mechanical nuclear field theory is established. Instead, the majority of nuclear structure studies have been guided by semiphenomenological models such as the "collective model" introduced by Bohr (1952) and extended and generalized by Bohr and Mottelson (1953, 1969, 1975), Nilsson (1955), Mottelson and Nilsson (1959), and a host of collaborators. At the heart of this model are the "collective variables" which ascribe such macroscopic features as size, deformation, and moments of inertia to the quantum-mechanical nucleus, and which enter into many popular parametrizations of nuclear interaction potentials.

This chapter focuses on some fundamental aspects of nuclear sizes and shapes. Examples of interaction potentials commonly used in the analysis of heavy-ion scattering data are discussed.

I. SIZES AND SHAPES

Rainwater (1950) proposed that nuclei may possess nonspherical equilibrium shapes. Evidence in support of this concept abounds. For example, as opposed to the atomic case, nuclei exhibit nonzero (and often large) intrinsic electric quadrupole and higher multipole moments. In fact, a plot of observed quadrupole moments versus atomic number (Preston and Bhaduri, 1975, Figure 3-2) shows a broad positive peak between atomic numbers 60 and 78, the rare-earth region, and a similar feature between atomic numbers 90 and 102, the actinide region. These have come to be known as the regions of "highly deformed" nuclei. A second example is the energy spacing of certain correlated low-lying excited states in several nuclei—the ground state rotational band. This spacing closely parallels that characteristic of a quantum-mechanical rigid rotor

$$E_I = \frac{\hbar^2}{2\mathcal{I}} I(I + 1) , \qquad \text{(II-1)}$$

where I is the angular momentum of the state in units of $\hbar$ and $\mathcal{I}$ is the rotor's moment of inertia.

Precise quantitative measurements of nuclear sizes and shapes are normally divided according to (a) those which use strong interaction probes sensitive primarily to the nuclear matter distribution and (b) those which employ electromagnetic interaction probes that predominantly sample the charge distribution. Examples of the former class are elastic and inelastic scattering of nucleons, pions, mesons and other strongly interacting projectiles; nucleon transfer reactions,

hadronic atom spectroscopy, and alpha decay. Examples of the latter class are photonuclear processes, electron scattering, μ-mesic atom x-ray measurements, atomic hyperfine structure, and Coulomb excitation with light and heavy ions. The experimental techniques, supporting theories, and recent results are reviewed amply by Collard, Elton, and Hofstadter (1967), Barrett and Jackson (1977), Mackintosh (1977), Alder and Winther (1966, 1975), and Bohr and Mottelson (1969, 1975).

The above investigations indicate that heavy nuclei are leptodermous (thin-skinned) systems—that is, the measured charge and matter distributions show small diffuseness parameters (defined as the radial distance over which the density drops from 90% to 10% of a nearly constant central value). This fact lends credibility to the concept of a nuclear "surface." Common definitions are (a) the equivalent sharp cutoff radius R, (b) the equivalent rms radius $\sqrt{\langle r^2 \rangle}$, and (c) the half-density radius $R_{1/2}$ [see Myers (1973) for an excellent discussion of the geometry of leptodermous distributions]. Nuclear densities typically are quoted in terms of the Fermi distribution

$$\rho(r) = \frac{\rho_0}{1 + \exp[(r-R_{1/2})/a]} , \qquad \text{(II-2)}$$

where ρ_0 is the central density and a is a measure of the diffuseness. Figure II-1 shows a plot of Eq. II-2 for a rare-earth nucleus for which $a \approx 0.65$ fm. Note that $R \approx \sqrt{\langle r^2 \rangle} \approx R_{1/2}$, which implies that there is only a slight ambiguity in specifying the nuclear radius.

Due to the saturation of the strong interaction, nuclear matter is nearly incompressible. Hence, the nuclear radius, to a good

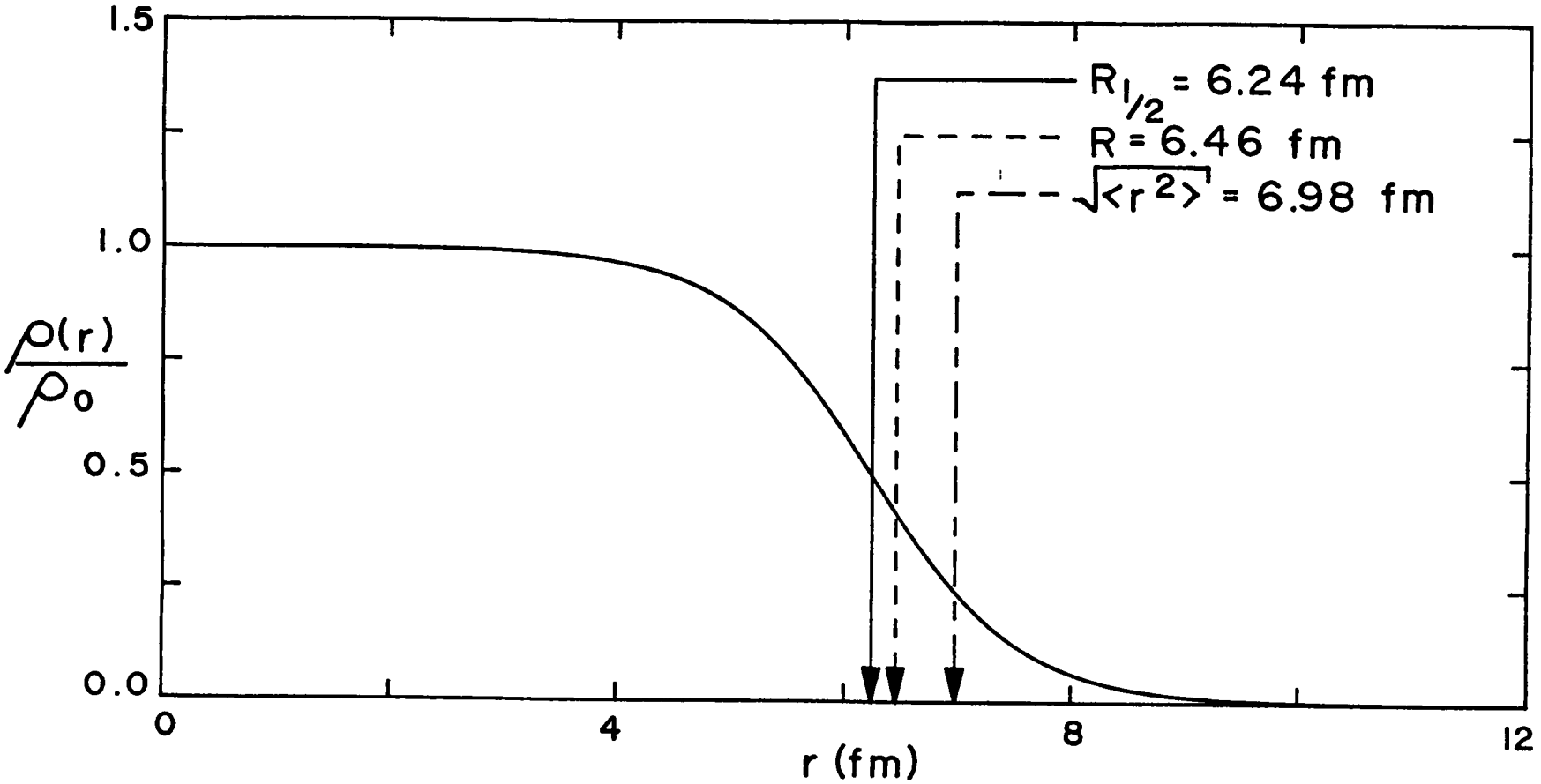


Figure II-1. Plot of a representative nuclear density distribution. The calculation is for a nucleus of atomic mass number A = 160 and diffuseness a = 0.65 fm. The half-density radius $R_{1/2}(= 1.2\ A^{1/3})$, the equivalent sharp cutoff radius R, and the equivalent rms radius $\sqrt{\langle r^2 \rangle}$ are marked by the arrows.

approximation, is proportional to the cube root of the atomic mass number A, so that for a wide range of nuclei it is observed that

$$R_{1/2} = r_0 A^{1/3} . \qquad \text{(II-3)}$$

For typical nuclei $r_0 \approx 1.2$ fm for charge distributions. The value of r_0 corresponding to nuclear interaction radii is not as well established.

The available evidence suggests that nuclei come in a variety of shapes—spherical, prolate, oblate, and even some suggesting a triaxial nature. A convenient parametrization of the nuclear surface in terms of the distortion of a liquid drop of radius R_0 is

$$R(\theta,\phi) = \frac{R_0}{\xi} [1 + \sum_{\lambda=2}^{\infty} \sum_{\mu=-\lambda}^{\lambda} \alpha_{\lambda\mu} Y_{\lambda\mu}(\theta,\phi)] , \qquad \text{(II-4)}$$

where θ and ϕ are the polar and azimuthal angle with respect to an arbitrary body-fixed axis for rigid nuclei (or a space-fixed axis for vibrational nuclei). This expression omits the $\lambda = 0$ high energy monopole resonance terms and the $\lambda = 1$ terms corresponding to a simple translation of the center of mass. The α's are deformation parameters and the $Y_{\lambda\mu}$ are spherical harmonics. A scale factor,

$$\xi \approx 1 + \frac{1}{4\pi} \sum_{\lambda=2}^{\infty} \sum_{\mu=-\lambda}^{\lambda} |\alpha_{\lambda\mu}|^2 , \qquad \text{(II-5)}$$

is required for volume conservation. For an axially symmetric nucleus Eq. II-4 simplifies to

$$R(\theta) = \frac{R_0}{\xi}[1 + \beta_2 Y_{20}(\theta) + \beta_4 Y_{40}(\theta) + \beta_6 Y_{60}(\theta) + \ldots] , \qquad \text{(II-6)}$$

where the β's are the standard deformation parameters quoted in the literature. (Because most deformation parameters are small, to a good approximation $\xi \approx 1$). Figure II-2 gives examples of pure quadrupole (β_2), hexadecapole (β_4), and hexakontattetara (β_6) deformations calculated with Eq. II-6.

Values of β_2 and β_4 have been measured for most deformed nuclei. A few reports suggesting β_6 distortions have appeared, particularly for the actinides, although the uncertainties are rather large. Figures II-3 and II-4 show plots of some nuclear shapes calculated with Eq. II-6 using published deformation parameters with $\xi = 1$ and $R_0 = r_0 A^{1/3}$ (see Eq. II-3).

II. NUCLEAR ION-ION INTERACTION POTENTIALS

The tremendous development of heavy-ion accelerators in recent years (Grunder and Selph, 1977) has provided an alternative to more traditional techniques of exploring nuclear structure: the study of heavy-ion reactions (Hodgson, 1978; Nörenberg and Weidenmüller, 1980; Broglia and Winther, 1981). In general, the scattering of one heavy ion from another is an extremely complicated many-body problem. For example, take the simpler case of a single nucleon scattering from a complex nucleus. One arrives at an infinite set of coupled one-particle equations

$$\frac{-\nabla^2}{2m}\psi_\alpha(\vec{r}) + \sum_{\alpha'} \overline{V}_{\alpha\alpha'}(\vec{r})\psi_{\alpha'}(\vec{r}) = (E - E_\alpha)\psi_\alpha(\vec{r}) \qquad \text{(II-7)}$$

with

$$\overline{V}_{\alpha\alpha'} = \langle \phi_\alpha(\vec{r}_t) | v(\vec{r},\vec{r}_t) | \phi_{\alpha'}(\vec{r}_t) \rangle \ . \qquad \text{(II-8)}$$

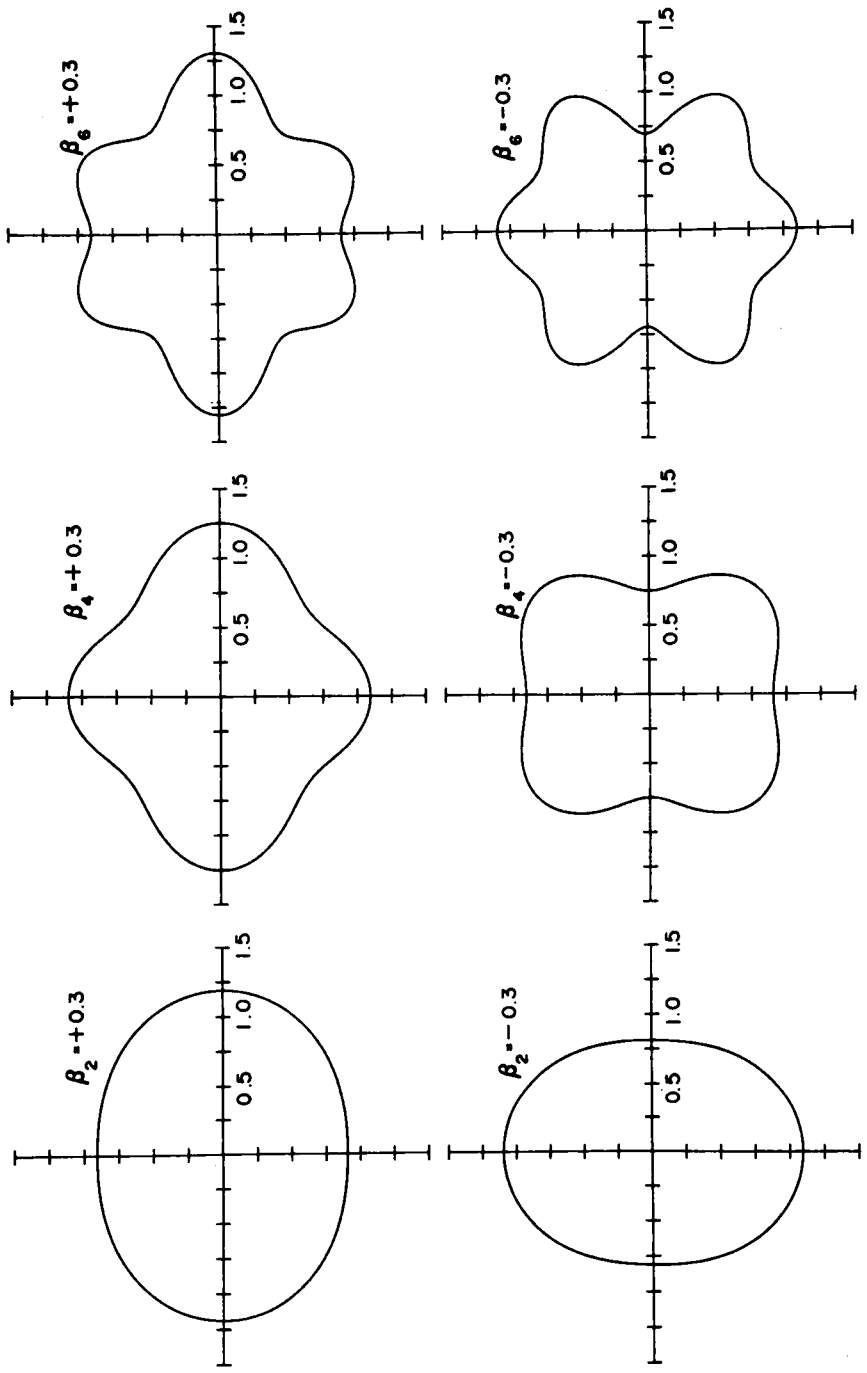


Figure II-2. Examples of pure β_2, β_4, and β_6 deformations.

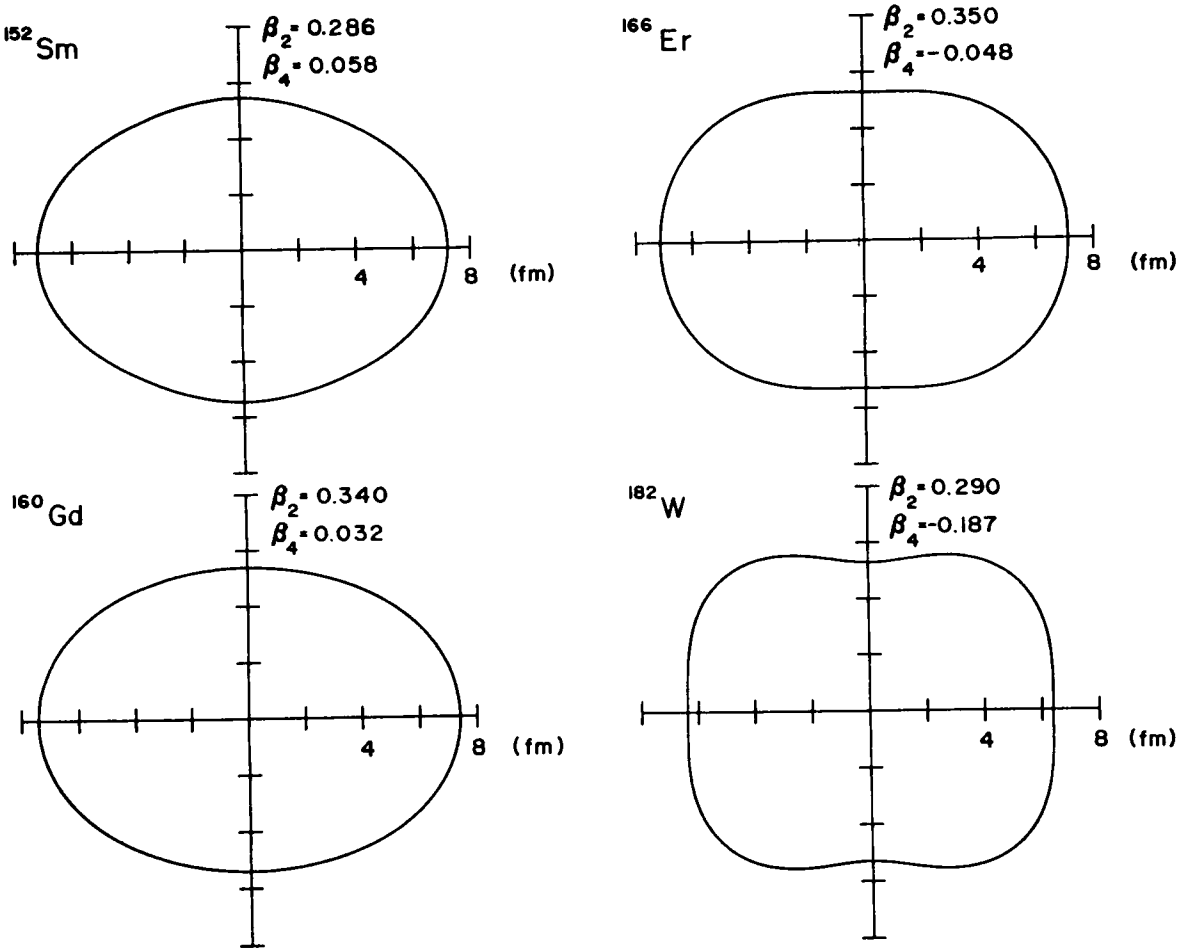


Figure II-3. The shapes of some deformed rare-earth nuclei. The ^{152}Sm, ^{160}Gd, and ^{166}Er deformation parameters are from Erb et al. (1972), and the ^{182}W parameters are from Lee et al. (1975). For all cases the radius parameter r_0 = 1.1 fm.

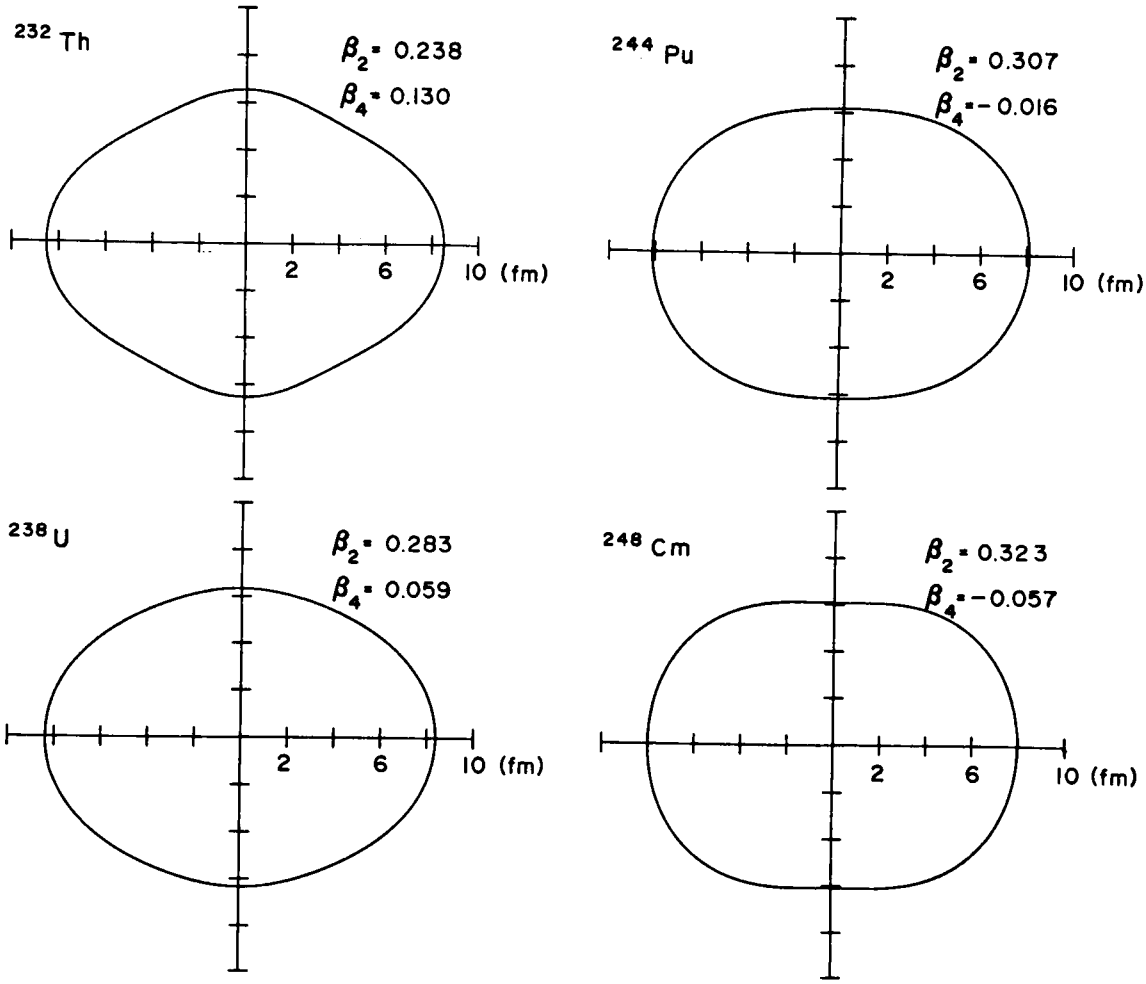


Figure II-4. Shapes of some deformed actinide nuclei. The deformation parameters are from Bemis et al. (1973). In all cases the radius parameter r_0 = 1.1 fm.

Projectile wavefunctions are denoted by $\psi(\vec{r})$ and target eigenfunctions are denoted by $\phi(\vec{r}_t)$. Entrance and exit channels are labeled α' and α, respectively. Summation is over both discrete and continuum states. The potential matrix $\overline{V}_{\alpha\alpha'}$ provides coupling via the interaction $v(\vec{r},\vec{r}_t)$. The projectile energy is E and the exit channel energy eigenvalue is E_α. Obviously the solution of Eq. II-7 is a formidable, if not impossible, task! If the projectile is a heavy ion, the situation is even more complicated.

An approximate solution of Eq. II-7 is possible if the summation is truncated. Continuum states are neglected and only a limited number of discrete states are considered. This is the so-called "coupled-channels method" (Tamura, 1969; Rhoades-Brown, Macfarlane, and Pieper, 1980a, 1980b). However, even with such gross simplifications, a huge amount of computation is required for any nontrivial case. Also, because the calculations involve so many coupled channels, a clear picture of the interaction mechanism is difficult to obtain.

The earliest and most popular treatment of the scattering of two heavy ions replaces Eq. II-7 with an effective one-body potential: the ion-ion interaction potential. A potential form containing certain free parameters is selected (somewhat arbitrarily). These parameters are determined by (a) fitting to experimental elastic and inelastic scattering cross sections or (b) microscopic calculations using effective constituent nucleon-nucleon interactions. The former is the "phenomenological" approach and the latter is the "theoretical" approach. One hopes that the result is a model-insensitive unambiguous potential from which nuclear structure can be inferred. Nörenberg and

Weidenmüller (1980) provide copious references to the literature on heavy-ion potentials.

The Phenomenological Optical Potential

The simplest example of an ion-ion interaction potential is the "optical potential," which was first suggested by Bethe (1940) and later developed as a tool in nuclear reaction physics by Feshbach, Porter, and Weisskopf (1953, 1954). Although originally developed for light-particle scattering, it has been adopted in heavy-ion physics. Excellent reviews of the physical background, formalism, and applications to single-nucleon, light-ion, and heavy-ion scattering are provided by Marmier and Sheldon (1970), Hodgson (1971, 1978), Sinha (1975), and Nörenberg and Weidenmüller (1980).

A simple expression for the optical potential is

$$V_{opt} = V + iW \ , \qquad \text{(II-9)}$$

where the real part V accounts for refractive effects and diffraction, and the imaginary part W takes into account the presence of other reaction channels not treated explicitly in the calculation. A Schrödinger equation which incorporates Eq. II-9 describes the propagation of a matter wave of energy E through an absorptive medium with a complex index of refraction η given by

$$\eta^2 = 1 - \frac{(V + iW)}{E} \ . \qquad \text{(II-10)}$$

The analogy to a similar situation for the scattering of light in optics gives rise to the term "optical potential."

Because theoretical calculations of the optical potential are difficult and not uniformly successful (especially for the imaginary part), phenomenological determinations have received the most emphasis. The standard parametrization is

$$V_{opt} = -V_0 f - iW_0 g \ , \qquad \text{(II-11)}$$

where V_0 and W_0 are positive strength parameters and f and g are modulating functions which contain adjustable parameters. Marmier and Sheldon (1970, Table 14-1) catalogue some of the commonly used form-factors. The usual practice, however, is to choose the Woods-Saxon (Woods and Saxon, 1954) formfactor

$$f(r) \equiv \{1 + \exp[(r - r_0(A_1^{1/3} + A_2^{1/3}))/a]\}^{-1} \qquad \text{(II-12)}$$

for both the real and imaginary parts. The subscripts 1 and 2 refer to projectile and target nucleus, respectively. Equation II-12 is valid for scattering of spherical nuclei. Typically, for inelastic scattering from deformed nuclei, the "deformed Woods-Saxon" formfactor

$$f(r,\theta) \equiv \{1 + \exp[(r - R(\theta))/a]\}^{-1} \ , \qquad \text{(II-13)}$$

where

$$R(\theta) = r_0[A_1^{1/3} + A_2^{1/3}(1 + \beta_2 Y_{20}(\theta) + \beta_4 Y_{20}(\theta))] \ , \qquad \text{(II-14)}$$

is used instead.

Excellent results are obtained with heavy-ion optical potentials. However, they are usually not unique. A number of known ambiguities are associated with the optical potential. The nature of these ambiguities is discussed by Igo (1959), Drisko, Bassel, and Satchler (1963), Bingham (1965), Hodgson (1971), and Nörenberg and Weidenmüller (1980).

Folding Potentials

If the relaxation time for the constituent nucleons is long compared to the collision time for a pair of heavy ions (so that the nucleonic densities are "frozen"), the matrix element

$$U_{aA}(\vec{R}) = \langle \psi_0^a \psi_0^A | V_{aA} | \psi_0^a \psi_0^A \rangle \qquad \text{(II-15)}$$

provides a reasonable estimate of the real nuclear ion-ion interaction potential for elastic scattering. In this expression V_{aA} represents a sum over all two-body interactions v_{12} between all nucleons in a and all nucleons in A, while ψ_0^a and ψ_0^A denote model ground-state wavefunctions for a and A, respectively. The expression is valid for low-energy collisions only and ignores antisymmetrization between nucleons in a and nucleons in A. Note that Eq. II-15 represents an effective interaction which in general is complex, nonlocal, energy- and angular-momentum dependent (Satchler and Love, 1979). Further, it differs from the free nucleon-nucleon interaction because (a) individual nucleons are surrounded by nuclear matter so that intermediate virtual states are blocked by the exclusion principle and (b) internucleon binding perturbs the matrix elements of the effective interaction off the energy shell for free nucleon-nucleon scattering (Hodgson, 1978).

With the above provisos, one can write

$$U_{aA}(\vec{R}) = \int d\vec{r}_1 \int d\vec{r}_2 \rho_1(\vec{r}_1)\rho_2(\vec{r}_2) v(\vec{r}_{12} = \vec{R} + \vec{r}_2 - \vec{r}_1) , \qquad \text{(II-16)}$$

where ρ_i is the density distribution of the nucleons in the ground state of the ith nucleus, $v(\vec{r}_{12})$ is an effective interaction between nucleons,

and the coordinates are defined in Figure II-5. Because Eq. II-16 involves an integration over two densities it is referred to as the double-folding potential (it is analogous to the potential for two charge distributions in electrostatics). To calculate $U_{aA}(\vec{R})$, density distributions must be chosen and a suitable effective interaction must be selected. The matter distributions are typically parametrized in terms of phenomenological Fermi distributions, and the interaction v_{12} is adjusted to get agreement with experimental scattering data. Excellent results have been obtained using such potentials to analyze heavy-ion scattering data, especially for collisions of spherical nuclei. Dover and Vary (1975), Hodgson (1978), Satchler and Love (1979), and Broglia and Winther (1981) review the various approaches in vogue. The application of folding potentials to deformed nuclei is currently under investigation (Satchler, 1981).

Often one of the integrations in Eq. II-16 is performed to obtain a single-folding potential

$$U_{aA}(\vec{R}) = \int d\vec{r}_1 U_{2N}(\vec{R} - \vec{r}_1)\rho_1(\vec{r}_1) \ , \qquad \text{(II-17)}$$

where

$$U_{2N}(\vec{R} - \vec{r}_1) = \int d\vec{r}_2 \rho_2(\vec{r}_2) v(\vec{r}_{12}) \ . \qquad \text{(II-18)}$$

This form represents an effective nucleon-nucleus interaction. The standard practice is to invoke empirical, phenomenological nucleon-nucleus potentials in place of U_{2N}. Invariably these single-folding potentials overestimate the strength of the real ion-ion potential by

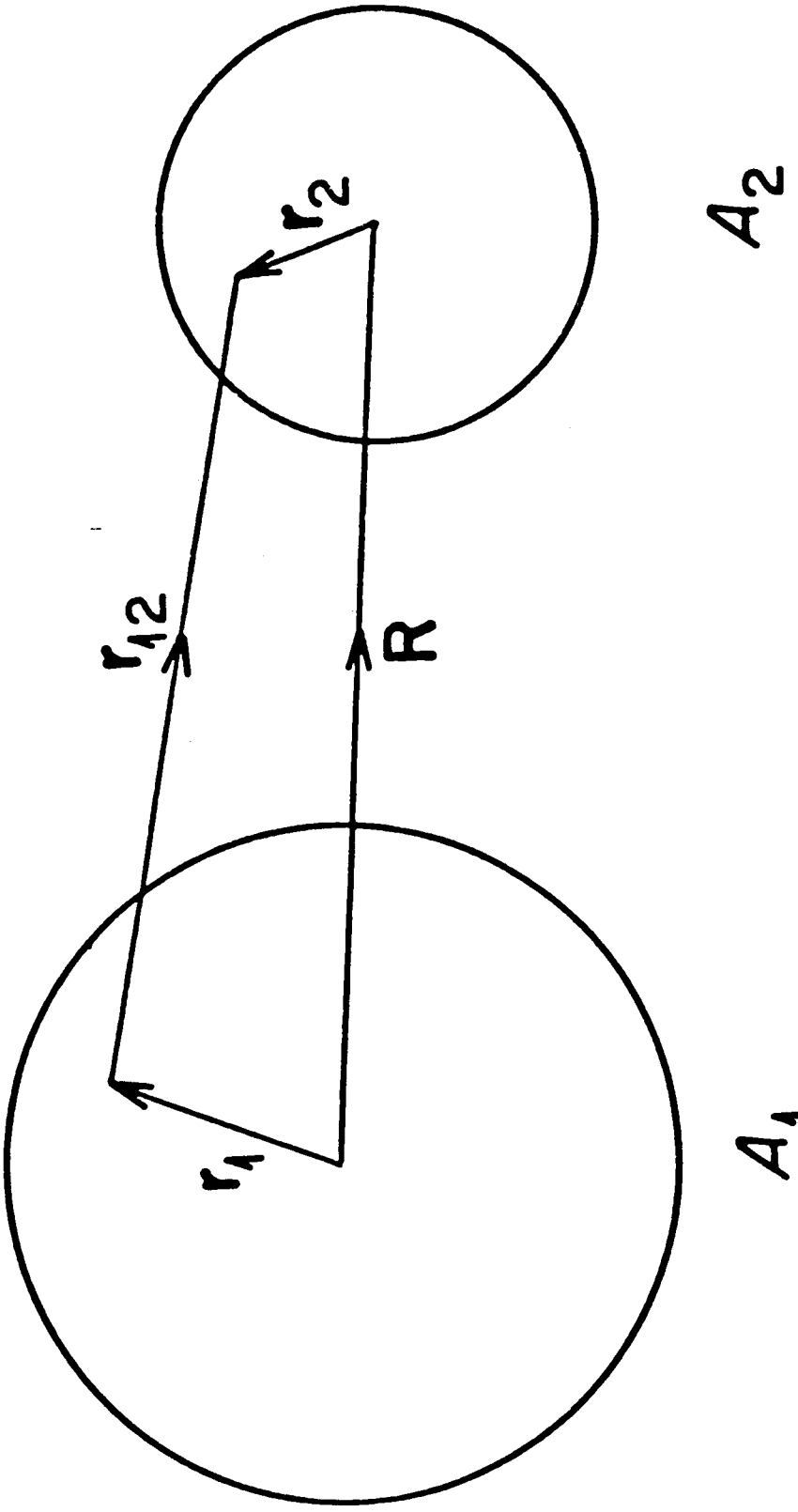


Figure II-5. Coordinates used to define the double-folding potential.

a factor of about two (Satchler, 1975). Satchler and Love (1979) give an explanation for this behavior.

Proximity and Energy-Density Potentials

A very useful approximate ion-ion potential, which exploits the fact that the short-range nuclear force manifests itself as a surface-surface interaction for heavy leptodermous nuclei, is the proximity potential (Blocki et al., 1977; Broglia and Winther, 1981). If the integrations in Eq. II-16 are performed up to an integration over the plane P perpendicular to the vector which connects the centers of the collision partners, the result is

$$V_{prox}(\vec{R}) = \int_P dxdy\ e(x,y;\vec{r}_i)\ , \qquad \text{(II-19)}$$

where $e(x,y;\vec{r}_i)$ denotes the interaction energy per unit area at the point (x,y) over the surface. In general, $e(x,y;\vec{r}_i)$ depends on a range parameter γ for the nuclear force and on the radii r_i and diffusenesses a_i of the nuclear density distributions. For heavy leptodermous systems $r_i >> a_i$ and $r_i >> \gamma$ so that $e(x,y;\vec{r}_i)$ has a very weak dependence on r_i and is therefore approximately equal to the interaction energy per unit area between two flat infinite nuclear surfaces. That is,

$$e(x,y;\vec{r}_i) \approx e_\infty(\xi'(x,y))\ , \qquad \text{(II-20)}$$

where ξ' is the gap function between surfaces, which in general depends on x and y because the surfaces are curved (Blocki et al., 1977). Introducing ξ' into Eq. II-19 as an integration variable and integrating over the other variable leads to

$$V_{prox}(\xi) = 2\pi\bar{R} \int_{\xi}^{\infty} e_{\infty}(\xi')d\xi' \ , \qquad \text{(II-21)}$$

where $\bar{R}$ is the geometric mean of the two nuclear radii. Calculation of the universal function $e_{\infty}(\xi')$ is discussed by Blocki et al. (1977). Randrup and Vaagen (1978) have extended the formalism to include deformed nuclei.

Another approach to solving Eq. II-16 employs $\varepsilon(\rho)$, the nuclear binding energy per unit volume calculated at a density ρ (Brueckner et al., 1968; Scheid and Greiner, 1969; Lombard, 1973; Ngô et al., 1975). Equation II-16 reduces to

$$V_{E\text{-}D}(\vec{R}) = \int d\vec{r}'[\varepsilon(\rho_1 + \rho_2) - \varepsilon(\rho_1) - \varepsilon(\rho_2)] \ , \qquad \text{(II-22)}$$

where the integration is over the full energy density distribution. In general, $\varepsilon(\rho)$ also depends on derivatives of ρ, resulting in surface effects which cause difficulties for close collisions of deformed nuclei. Krappe, Nix, and Sierk (1979) have developed a scheme using a double-folding of a Yukawa-plus-exponential potential which circumvents these problems. Their "unified" nuclear potential appears to do an excellent job of reproducing heavy-ion elastic scattering, fusion, fission, and ground-state masses and deformations.

CHAPTER III

CLASSICAL LIMIT S-MATRIX FORMALISM FOR COULOMB-NUCLEAR INTERFERENCE

This search for ion-ion interaction potentials exploiting the localization effects inherent in heavy-ion collisions was a direct result of the success of the classical limit S-matrix (CLSM) formalism in reproducing heavy-ion multiple Coulomb excitation results (Massmann, 1975; Massmann and Rasmussen, 1975; Donangelo et al., 1976; Guidry et al., 1978b) and the qualitative and quantitative features of Coulomb-nuclear interference (CNI) in heavy-ion scattering (Guidry et al., 1976a; Donangelo, 1977). In this chapter, the basic CLSM theory needed to understand subsequent chapters is summarized, and some of the pertinent aspects of Coulomb-nuclear interference are outlined. Complete discussions of this material are contained in the references cited above.

I. MODEL ASSUMPTIONS AND COORDINATES

In this study, the scattering event is considered to be a collision between a spherical projectile and an axially symmetric deformed even-even target nucleus. The target nucleus is rotationally excited via the Coulomb and nuclear fields of the projectile. Vibrational modes, except for an adiabatic excitation of giant multipole resonances, are neglected. The scattering is restricted to very nearly backward scattering ($\sim 180°$) in the center-of-mass system. This has two important consequences.

1. Restriction to backward scattering insures that trajectories corresponding to monotonic deflection functions make the dominant contribution.
2. The density of partial waves in a heavy-ion collision is such that the deflection function is very nearly continuous so that a specific scattering angle can be assigned to each partial wave.

Therefore, the gross simplification of assuming that only $J_{in} \sim 0$ contributes to the backward scattering is justified.

Figure III-1 shows the coordinates sufficient to describe the system. The distance between centers is r. Because the scattering is confined to a plane by angular momentum conservation and because of the spherical symmetry of the projectile and the fact that only near-zero impact parameters contribute to excitation of the axially symmetric target nucleus, no azimuthal coordinate is necessary. There remains a single rotational degree of freedom, which can be related to χ, the angle between the symmetry axis of the target nucleus and the line joining centers, because of the definition

$$\chi \equiv \beta - \theta \qquad \text{(III-1)}$$

and the conservation of angular momentum relation

$$\mathcal{I}\dot{\beta} + mr^2\dot{\theta} = 0 \ . \qquad \text{(III-2)}$$

The angle between the symmetry axis of the target nucleus and the exit channel trajectory is β, while θ is the scattering angle. $\mathcal{I}$ is the moment of inertia of the rotor and m is the reduced mass of the system.

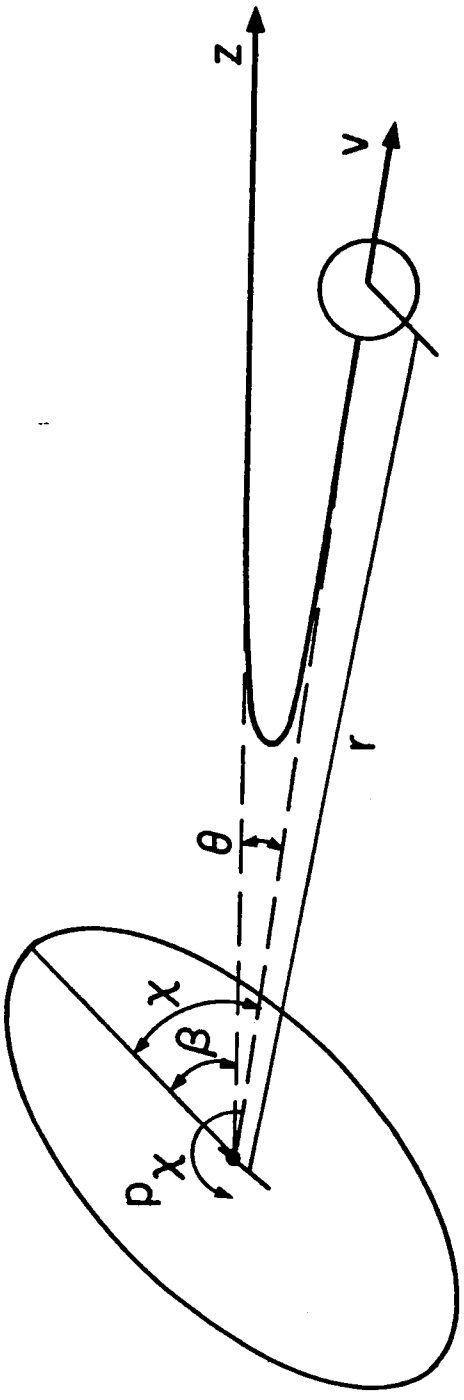


Figure III-1. Coordinate system for inelastic backward scattering from a deformed nucleus.

The classical Hamiltonian for the system described above is

$$H(p_r, p_\chi, r, \chi) = \frac{p_r^2}{2m} + \left(\frac{1}{2\mathcal{I}} + \frac{1}{2mr^2}\right) p_\chi^2$$

$$+ \frac{Z_p Z_t e^2}{r} + \frac{Z_p e^2}{2r^3} Q_0^{(2)} P_2(\cos\chi)$$

$$+ \frac{Z_p e^2}{2r^5} Q_0^{(4)} P_4(\cos\chi) + V_{pol}(r,\chi) - V_0 f_R(r,\chi) - iW_0 f_I(r,\chi) , \qquad \text{(III-3)}$$

where the radial and angular momenta conjugate to the coordinates r and χ of Figure III-1 are p_r and p_χ, respectively. The projectile has charge $Z_p e$ and the target nucleus has charge $Z_T e$. The $P_\lambda(\cos\chi)$ are Legendre polynomials of order λ and the $Q_0^{(\lambda)}$ are intrinsic charge multipole moments of order λ given by:

$$Q_0^{(\lambda)} = \sqrt{\frac{16\pi}{2\lambda + 1}} \int d^3\vec{r}\, \rho(r)\, Y_{\lambda 0}(\hat{r})\, r^\lambda , \qquad \text{(III-4)}$$

where $\rho(r)$ is the target nucleus charge-density function. The term $V_{pol}(r,\chi)$ represents a polarization potential arising from adiabatic giant resonance excitation. Appendix A contains a derivation and discussion of the exact form employed in this work. $V_0 f_R + iW_0 f_I$ represents a complex deformed nuclear potential with modulating functions f_R and f_I for the real and imaginary parts, respectively. Explicit expressions for f_R and f_I will be given in Chapter VI.

In Eq. III-3 only the monopole-monopole, monopole-quadrupole, and monopole-hexadecapole electric interactions are included. Magnetic

interactions are neglected. Corrections to the basic multipole-multipole electric interaction due to overlap of charge distributions are omitted, as justified in Appendix B. It is important to keep these assumptions in mind because the nuclear potential will be determined by using as a reference potential a Coulomb interaction which is supposedly well understood.

II. CLSM FORMALISM

The CLSM method is semiclassical in nature. Probability amplitudes are calculated via integration of the classical equations of motion corresponding to Eq. III-3 and are manipulated according to normal quantum-mechanical rules which allow for interference effects. The CLSM approach differs from the widely known Winther-de Boer technique for multiple Coulomb excitation (Winther and de Boer, 1966; Alder and Winther, 1975), which treats relative motion degrees of freedom (e.g., r and p_r) classically and internal degrees of freedom (e.g., χ and p_χ) quantum mechanically. In the CLSM approach all degrees of freedom are treated on an equal footing. This allows very simple physical interpretations of the excitation mechanism.

The $J = 0$ CLSM amplitude for rotational scattering to a final spin $I = p_\chi/\hbar$ from the 0^+ ground state of an even-even rotor is given by

$$S_{0\to I}^{J=0} = \frac{1}{2}\sqrt{2I+1}\int_0^\pi P_I(\cos\bar{\chi})\sqrt{\sin\chi_0 \sin\bar{\chi}\frac{d\bar{\chi}}{d\chi_0}}\times e^{i\phi'}\,d\chi_0\,, \tag{III-5}$$

where the barred quantities are defined explicitly by Donangelo et al.

(1978) and are related to the corresponding unbarred quantities by canonical transformations, and the phase ϕ' is defined by

$$\phi' = -\frac{1}{\hbar}\int [r(t)\, dp_r(t) + \chi(t)\, dp_\chi(t)]$$

$$+\frac{1}{\hbar}\bar{\chi}p_\chi + \frac{1}{\hbar}\int_{\tilde{r}_T}^{r} \tilde{p}_r\, d\tilde{r} + \sigma_0(\eta_0) + \sigma_I(\eta_I)\,, \qquad \text{(III-6)}$$

where the $\sigma_I(\eta_I)$ are Coulomb phase shifts, the tilde quantities are defined by Donangelo et al. (1978), and $\tilde{r}_T$ is the turning point of the radial motion for an elastic collision. As discussed elsewhere, Eq. III-5 may be integrated numerically [the integral method of Donangelo et al. (1976) and Guidry et al. (1978b)]. Alternatively, the integral can be evaluated using asymptotic expansions and uniform saddle-point integration methods [the saddle-point method of Massmann and Rasmussen (1975), Guidry et al. (1976a), and Guidry et al. (1978b)].

Figure III-2 represents a plot of a typical quantum-number function (the final spin of the rotor I_f versus initial orientation angle χ_0) obtained by integrating the classical equations of motion corresponding to Eq. III-3 for the case of pure Coulomb excitation (no nuclear or polarization potential). Classically allowed transitions are defined as those which satisfy the semiclassical criterion that $I_f + \frac{1}{2}$ falls within the functional range of the quantum-number function (Massmann, 1975; Massmann and Rasmussen, 1975; Guidry et al., 1976a; Donangelo, 1977). In Figure III-2, $I_{max} = 8^+$ is the maximum classically allowed spin. Those spins lying above the top of the quantum-number function are classically forbidden. In general for classically allowed transitions two trajectories

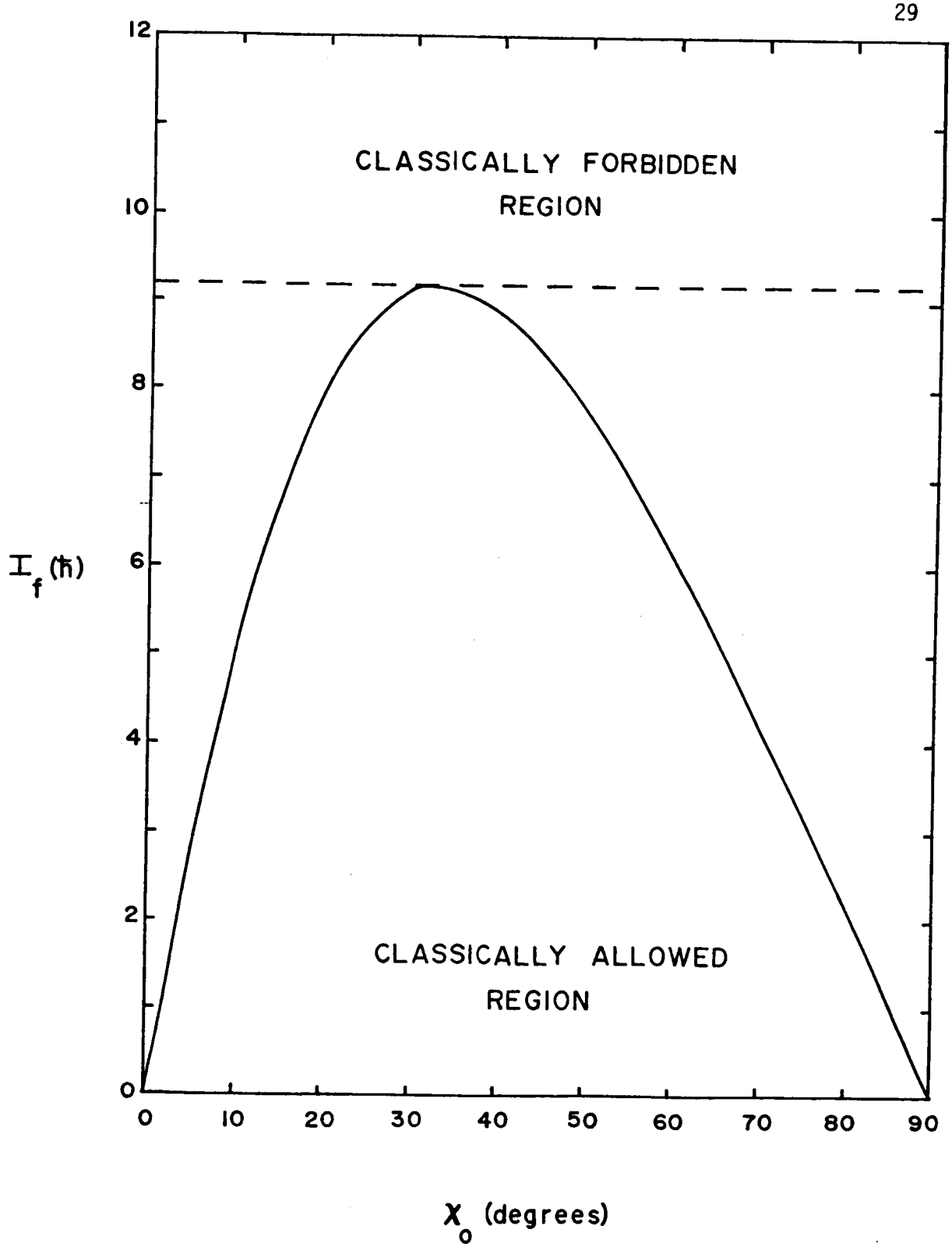


Figure III-2. Plot of a typical quantum-number function. The calculation is for pure Coulomb excitation of ^{160}Gd by 140-MeV ^{40}Ar projectiles. The classically allowed and classically forbidden regions are indicated. Results are similar if a nuclear potential is included.

(points of stationary phase) dominate in the evaluation of Eq. III-5 (Levit, Smilansky, Pelte, 1974; Massmann and Rasmussen, 1975; Guidry et al., 1976a). The J = 0 amplitude in that case becomes

$$S_{0\to I}^{J=0} = -\sqrt{\pi}\, e^{\frac{i}{2}(\Phi_1+\Phi_2)}[(\sqrt{\bar{p}_1} + \sqrt{-\bar{p}_2})\xi^{\frac{1}{4}}\, Ai(-\xi)$$

$$-i\,(\sqrt{\bar{p}_1} - \sqrt{-\bar{p}_2})\, Ai'(-\xi)/\xi^{\frac{1}{4}}] \,, \qquad \text{(III-7)}$$

where the quantities Ai and Ai' represent the complex Airy function and its first derivative, respectively. The classical action Φ is defined by the differential equation

$$\dot{\Phi} = -\frac{1}{\hbar}(r\dot{p}_r + x\dot{p}_x) \,. \qquad \text{(III-8)}$$

The classical probability amplitudes $\bar{p}_k$ are defined by

$$\bar{p}_k = \frac{2 \sin \bar{x}_k}{[\partial I(x_0)/\partial x_0]_{\bar{x}_k}} \qquad (k = 1,2) \qquad \text{(III-9)}$$

with the k indexing the stationary phase trajectories, and the Airy function argument is given by

$$\xi = [\tfrac{3}{4}(\Phi_2 - \Phi_1)]^{2/3} \,. \qquad \text{(III-10)}$$

All the quantities used in these equations are determined by integration of the classical equations of motion generated from the classical

Hamiltonian (Eq. III-3) and starting with an initial orientation angle χ_0.

To simplify calculations: (a) classically forbidden transitions are treated approximately by analytical continuation of the quantum-number function and (b) the imaginary potential is assumed to be purely absorptive, so that no refractive or diffractive effects are included (Guidry et al., 1976a; Guidry et al., 1981a). Because the imaginary potential has significant influence only in the highest-energy data, these approximations introduce little uncertainty into the data analysis.

Because of its conceptual utility, it is useful to introduce an approximation to Eq. III-7 which is valid for well-separated points of stationary phase

$$S_{0\to I}^{J=0} \approx i[\sqrt{|\bar{p}_1|}\, e^{i(\Phi_1 + \frac{\pi}{4})} + \sqrt{|\bar{p}_2|}\, e^{i(\Phi_2 - \frac{\pi}{4})}] \ . \qquad \text{(III-11)}$$

As verified by comparison to quantum-mechanical coupled-channels calculations for heavy-ion rotational scattering which employ full partial-wave summations (Rhoades-Brown et al., 1981), to a very good approximation the probability for exciting a spin I is determined by the single J = 0 term

$$P_{0\to I} \approx |S_{0\to I}^{J=0}|^2 \qquad \text{(III-12)}$$

where the S-matrix element $S_{0\to I}^{J=0}$ is determined from Eqs. III-5, III-7, or III-11. Note that whereas these equations define amplitudes which are to be manipulated according to the principle of quantum superposition,

the quantities necessary to evaluate these amplitudes are determined by integrating classical equations of motion. This is the meaning of the term classical limit. All numerical work discussed here utilizes the more accurate expressions of Eqs. III-5 or III-7, but the discussion is facilitated by writing the probability explicitly in the approximation of Eq. III-11. From Eqs. III-11 and III-12

$$P_{0\to I} \approx \begin{cases} p_1 + p_2 + 2\sqrt{p_1 p_2}\,\sin(\Delta\Phi) & \text{classically allowed states} \quad \text{(III-13a)} \\ p e^{-2\Im m(\Phi)} & \text{classically forbidden states} \quad \text{(III-13b)} \end{cases}$$

where p_1 and p_2 are the classical probabilities for the first and second trajectories, respectively, and p is the classical probability for the single trajectory that contributes to exciting a classically forbidden state (Guidry et al., 1976a; Donangelo et al., 1976; Guidry et al., 1978b). In Eq. III-13b, $\Delta\Phi = \mathrm{Re}(\Phi_2 - \Phi_1)$, the real part of the phase difference. In Eq. III-13b, $\Im m(\Phi)$ is the imaginary part of the phase Φ for that single trajectory. The quantum interference structure for the classically allowed states (those that can be reached by classical mechanics) in Eq. III-13a arises from the coherent contribution of two real saddle points to the probability for a given state and is a manifestation of the quantum principle of superposition. For classically forbidden states (those that cannot be reached by classical mechanics with real trajectories), only a single exponentially damped term contributes to the probability, as dictated by the topology of the integrand in Eq. III-5. The exponential damping is associated with

penetration into classically forbidden regions on complex classical trajectories and may be viewed as a manifestation of the uncertainty principle in classical-limit mechanics.

The basic structure of these two equations is illustrated in Figure III-3 for the case of pure E2 Coulomb excitation in the sudden limit and for an infinite Sommerfeld parameter η($\eta = Z_t Z_p e^2/\hbar v_0$, where v_0 is the initial relative velocity). It is a remarkable fact that for this case the CLSM and exact quantum mechanical results can be obtained analytically and that the corresponding expressions are identical. For low enough values of the quadrupole coupling parameter $\bar{q}_2$ ($\bar{q}_2 = m^2 v_0^3 Q_0^{(2)}/4\hbar Z_t^2 Z_p e^2$) the excitation probability for a given state decreases rapidly and monotonically with decreasing interaction. These are the forbidden states for that region. For increased $\bar{q}_2$ the same state becomes classically allowed and the excitation function begins to oscillate because of the interference between two contributing orientation angles. For example, the 6^+ state is classically forbidden at low values of $\bar{q}_2$ and the probability increases monotonically with $\bar{q}_2$ until $I_{crit} \sim 2\bar{q}_2 \gtrsim 6$, at which point the 6^+ state becomes classically allowed and the probability begins to oscillate. These two types of behavior are precisely described by the CLSM calculations.

III. GENERAL EFFECTS OF THE COULOMB-NUCLEAR INTERFERENCE

To understand the general effect of the competition between Coulomb and nuclear forces in producing multistep excitation it is useful to consider the approximate formulae, Eq. III-13. The classically allowed probabilities are characterized by an interference term. This

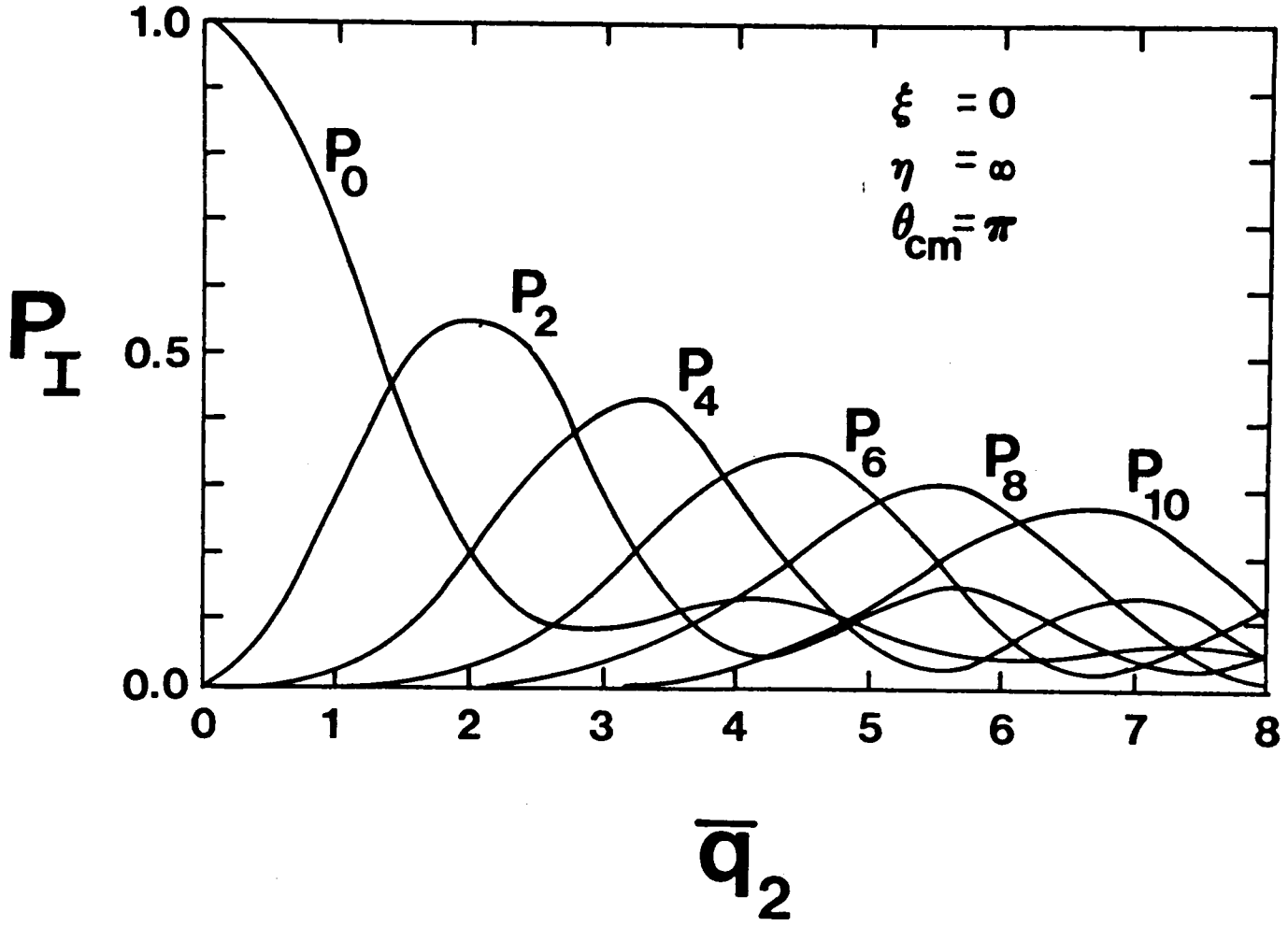


Figure III-3. Coulomb excitation probabilities versus quadrupole coupling strength $\bar{q}_2$. Calculations are for a rotor in the $\eta \to \infty$, sudden impact limit. Quantum-mechanical and CLSM calculations are identical for this case.

interference should not be confused with the Coulomb-nuclear interference—it would remain even in the presence of a pure Coulomb or pure nuclear force (cf. the oscillations in Figure III-3 for pure Coulomb excitation). It results from the quantum principle of superposition and represents an interference between two different initial orientation angles of the classical rotor which lead to the same final angular momentum. This structure is termed the quantum-mechanical interference since it vanishes in the limit $\hbar \to 0$. For the classically allowed states the Coulomb-nuclear interference involves modification of the quantum-mechanical interference structure by the competition (classical interference) between Coulomb and nuclear forces in transferring angular momentum. This competition is represented classically in Figures III-4 and III-5, and the effect of the nuclear force on the phase is shown in Figure III-6.

The classically forbidden states are characterized by an exponential damping due to the increase of the imaginary part of the classical phase (Eq. III-13b). This imaginary component of the classical action is acquired because penetration into classically forbidden regions involves a complex classical trajectory. It arises formally because complex initial orientation angles (which are not quantum-mechanical observables) are required to reach spins above the maximum spin shown in the quantum-number function (Figure III-2, p. 29). Since the competition between Coulomb and real nuclear forces will act to lower the quantum-number function of Figure III-2, CNI for classically forbidden states will involve an increase in their forbiddeness and hence an increasingly damped structure. These considerations are true for a purely real

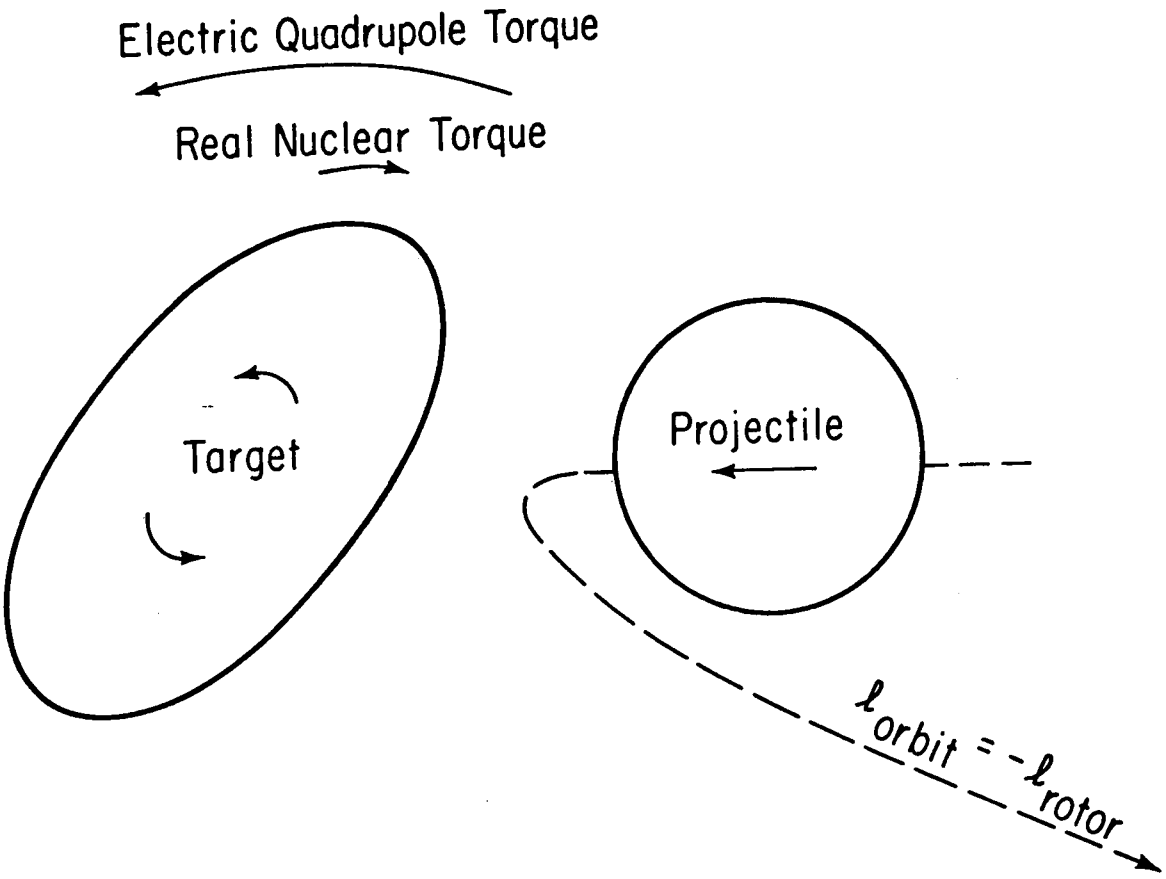


Figure III-4. Schematic illustration of classical CNI. The competition between the repulsive electric quadrupole potential and the attractive real nuclear potential is indicated.

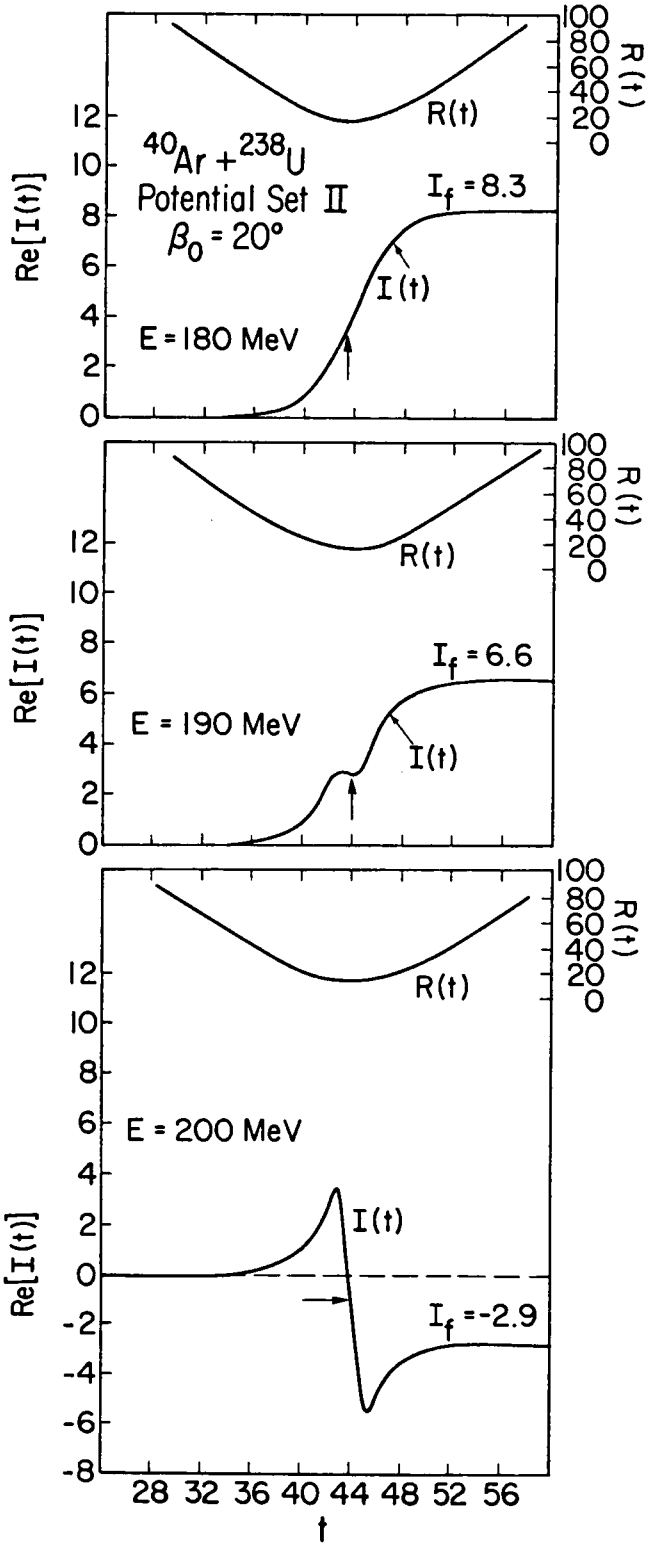


Figure III-5. Illustration of classical angular momentum transfer in CNI. Each calculation is for zero impact parameter and initial rotor orientation angle $\beta_0 = 20°$ and uses parameter set II of Guidry et al. (1976a) for the nuclear potential. The classical spin of the rotor I(t) [in $\hbar$ units] and the radial separation R(t) as a function of dimensionless time units. The arrows indicate the values at the distance of closest approach.

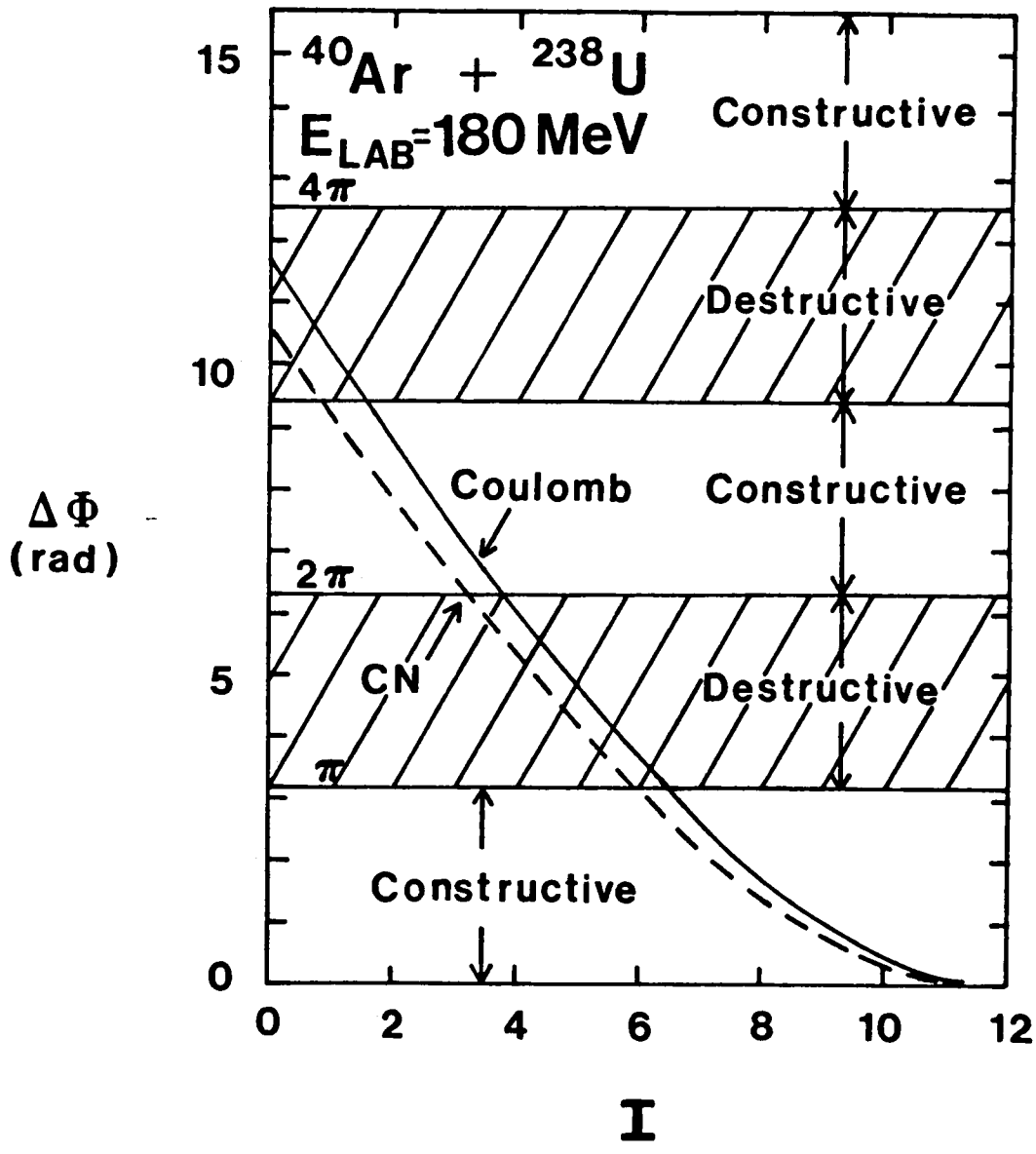


Figure III-6. The real part of the phase difference $\Delta\Phi$ versus final spin I. I is given in units of $\hbar$. Calculations are for ^{40}Ar + ^{238}U at E_{LAB} = 180 MeV. The solid curve resulted from parameter set I of Guidry et al. (1976a) [pure Coulomb excitation]. The dashed curve resulted from parameter set II of Guidry et al. (1976a) [Coulomb-nuclear excitation]. Regions of constructive and destructive interference are indicated.

nuclear potential. In the case of a complex nuclear potential, the imaginary part of the potential will contribute an additional damping in both the forbidden and allowed cases.

As discussed in detail previously (Guidry et al., 1976a), the initial effect of the interference between Coulomb and nuclear forces should appear in the sensitive phases of Eq. III-13, with the p's only slightly affected. If that is the case, it becomes particularly simple to predict the modification of the pure Coulomb excitation brought about by the admixture of a nuclear force: (a) the oscillations in the excitation function for pure Coulomb excitation of classically allowed states which are due to the quantum-mechanical interference will be shifted in phase by the CNI; and (b) the classically forbidden states will be damped (become more forbidden) due to the CNI.

The initial effect of combining an attractive real nuclear force with the Coulomb force is to decrease the real phase difference for the classically allowed states and to increase the imaginary phase for the classically forbidden states. Therefore in the initial interference region it is expected that the effect of the CNI can be predicted from the effect of the nuclear potential on the sine term of Eq. III-13a and the exponential damping factor of Eq. III-13b. This allows a simple rule for the nature of the heavy-ion CNI: The initial Coulomb-nuclear interference will be constructive if the excitation function for pure Coulomb excitation is approaching or has reached a minimum; it will be destructive if the excitation function for pure Coulomb excitation is approaching or has reached a maximum.

It should be noted that this rule is predicated on the nuclear potential being largely real and smoothly varying in the tail region and

applies only to the initial interference where the CNI effect is dominated by the phases. For large imaginary potentials, or for deeper penetration into the potential other effects (e.g., changes in the classical p's of Eq. III-13) become important, and one must rely increasingly on the details of the calculation. Note that the phase rule of Malfliet, Landowne, and Rostokin (1973) for CNI appears to be a close analog of the above rule in the limit of single-step excitation. Whether the above assumptions are fulfilled in real nuclear systems is a matter for experimental verification. It is apparent from the excitation functions in Figures III-7 and III-8 that the rule works remarkably well. In all cases shown there the interference structure is as predicted above.

From the above considerations and Figure III-3 (p. 34) one realizes why only destructive interferences are seen for α-particle excitation of 2^+ and 4^+ states, and for the $^{16}O + ^{162}Dy$ example in Figure III-8. For subbarrier scattering the dominant monopole-quadrupole Coulomb interaction is not sufficient in either case to have caused the excitation function to have passed its first maximum, and the initial CNI is always destructive. This is clear from Figure III-3 (p. 34) and the simple rule stated above, and implies a critical value of the quadrupole coupling strength $\bar{q}_2$ for observing initial constructive interference. In practical terms, for typical well-deformed targets the Z of the projectile must exceed a value lying roughly in the region between Ne and Ar projectiles before the initial interference may be constructive.

The success of the above qualitative predictions suggests that the tail of the deformed potential is smoothly varying and largely real.

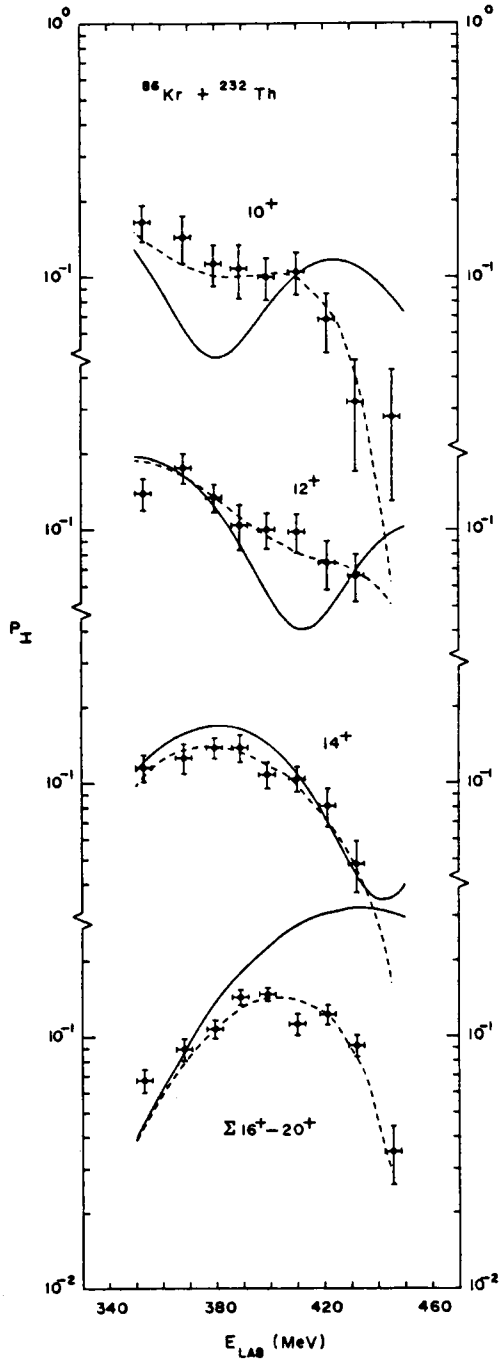


Figure III-7. Excitation functions for the $^{86}Kr + ^{232}Th$ system which demonstrate the simple rule for heavy-ion CNI. The solid curves are calculations assuming pure Coulomb excitation, while the dashed curves are fits determined in a manner similar to those reported in Chapter VI.

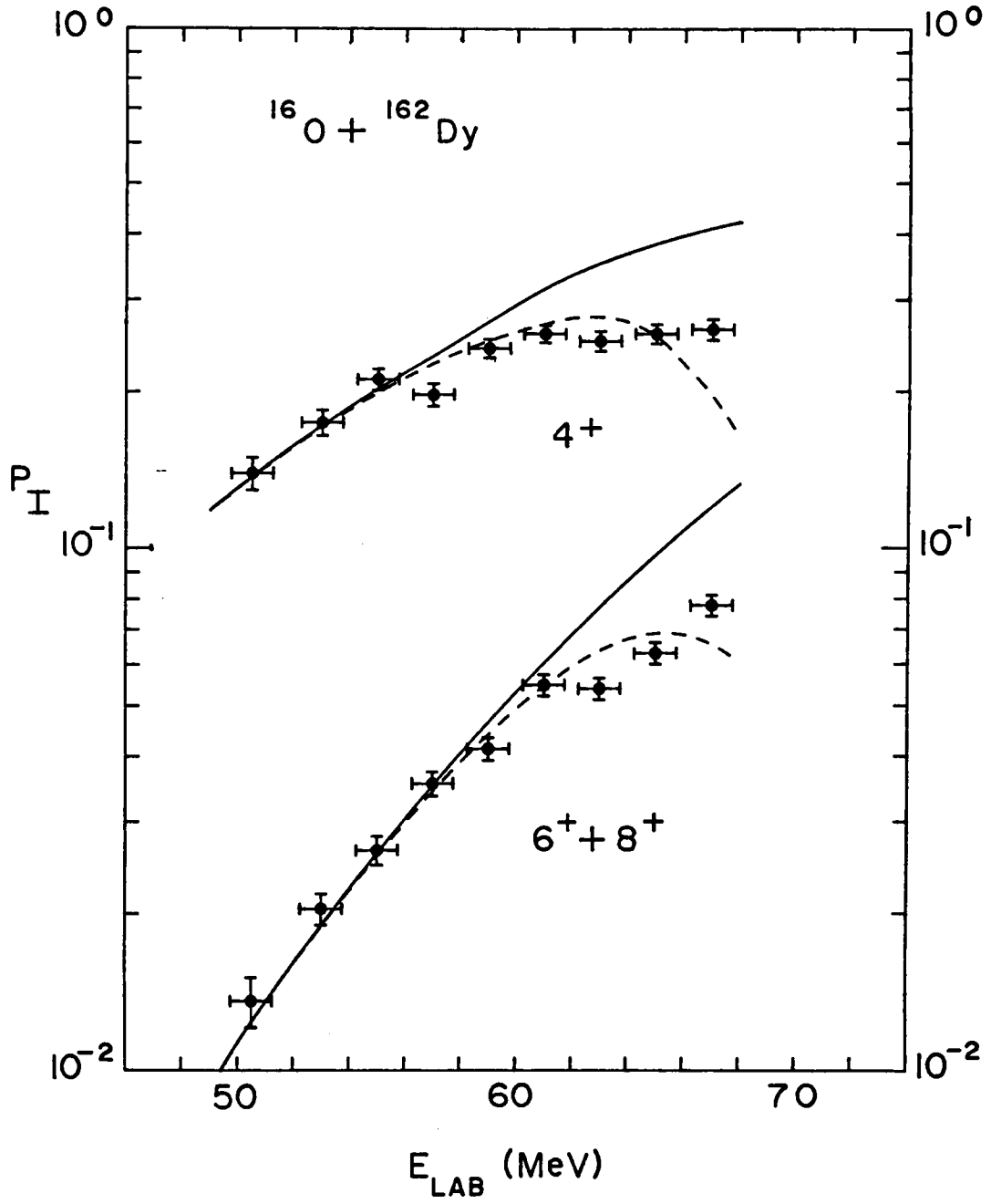


Figure III-8. Same as Figure III-7, except for the $^{16}O + ^{162}Dy$ system.

It is also clear that the model presented here for the CNI is at least qualitatively correct. Hence it is natural to propose that experiments of this nature can provide an extremely sensitive probe of the deformed nuclear surface, as suggested by Malfliet, Landowne, and Rostokin (1973) and Guidry et al. (1978a). This sensitivity is due to the strong influence of the phases in Eq. III-13. Furthermore, this sensitivity will be augmented by the localization of the heavy-ion interaction radially and in angle on the nuclear surface (discussed in Chapter IV).

The above ideas concerning the effect of competition between nuclear and Coulomb forces on a basic quantum interference structure and on wave mechanical penetration into classically forbidden regions can be generalized. For example, one may consider E2-E4 interference within a similar model and exploit the modification induced by the E4 potential on the basic quantum-mechanical interference structure of the dominant E2 excitation to determine the E4 moment. Or one can apply a similar analysis to the effect of the giant resonance adiabatic polarization potentials on the quantum-mechanical interference structure associated with the dominant part of the potential. This approach amounts to using a (well-understood) dominant part of the potential to establish a reference excitation pattern. The sensitivity of this reference pattern to even small perturbations (due to the phases involved) is then exploited to measure other parts of the potential.

IV. COMPARISON OF CLSM CALCULATIONS TO EXACT QUANTUM-MECHANICAL COUPLED-CHANNELS CALCULATIONS

When the CLSM formalism was first developed to treat heavy-ion inelastic excitation its accuracy could only be inferred from extrapolations based on comparisons to exact quantum-mechanical coupled-channels calculations [using the code AROSA (Roesel, Saladin, and Alder, 1974)] and semiclassical Winther-de Boer (Winther and de Boer, 1966) calculations for pure Coulomb excitation in lighter systems (Guidry et al., 1978b). Excellent agreement, both in magnitude and in phase, among the S-matrix elements calculated via the three methods was obtained for such systems as $^{1}H + {}^{168}Er$, $^{2}H + {}^{168}Er$, and $^{4}He + {}^{168}Er$. The CLSM approach should be more accurate for heavier systems [e.g., ^{40}Ar + (rare-earth)] than for lighter systems (because the semiclassical approximations become more valid). Therefore, the accuracy of the CLSM approach was assumed when it was extended to heavy-ion inelastic scattering in the CNI region. Only recently could the validity of this assumption be tested rigorously.

Rhoades-Brown et al. (1981) have made a model-model comparison of the CLSM formalism and the fully quantum-mechanical coupled-channels formalism of Rhoades-Brown et al. (1980a, 1980b) which is applicable to very heavy systems. They treat the case of multiple quadrupole excitation of the ground-state rotational band of ^{160}Gd up to the 12^{+} state by backward scattered 120-185 MeV ^{40}Ar projectiles. This energy range spans regions of pure Coulomb excitation, strong CNI, and strong absorptive damping. [Note that the maximum classically allowed spin occurs at approximately the 8^{+} state.]

The model Hamiltonian employed in both calculations is given by Eq. III-3 with $Q_0^{(2)} = 6.168$ eb, $Q_0^{(4)} \equiv 0$, $V_{pol}(r,\chi) \equiv 0$, $V_0 = 15$ MeV, $W_0 = 10$ MeV, and $f_R(r,\chi) = f_I(r,\chi)$, where

$$f_R(r,\chi) = f(r) + \sqrt{\frac{5}{4\pi}} \frac{\partial f(r)}{\partial r} P_2 (\cos \chi) \delta_2^N . \qquad \text{(III-14)}$$

In Eq. III-14, $f(r)$ is the Woods-Saxon formfactor defined in Eq. II-12 (for the calculations discussed here $r_0 = 1.2$ fm and $a = 0.5$ fm). The quantity δ_2^N is defined by

$$\delta_2^N = r_0 A_T^{1/3} \beta_2^N \text{ fm} , \qquad \text{(III-15)}$$

where r_0 is defined in Eq. II-3, A_T is the atomic mass number of the target nucleus, and β_2^N is the nuclear quadrupole deformation parameter. For these calculations $\beta_2^N = 0.2$. The moment of inertia $\mathcal{I}$ in Eq. III-3 was determined by setting the energy of the first excited 2^+ state equal to 80 keV. The energies of the other states were then obtained using the rotational model (Eq. II-1).

Two separate coupled-channels calculations were performed to obtain quantum-mechanical inelastic excitation probabilities for comparison to the J = 0 CLSM probabilities defined by Eq. III-12. The first involved truncation of the partial wave sum to J = 0 only, and the second involved a full quantal calculation including all J values up to a maximum of J = 2400. For the J = 0 quantal calculations the probability of inelastic excitation for backward projectile scattering P_I (180°) is defined through the square modulus of the appropriate

S-matrix element (i.e., Eq. III-12). The probability $P_I(\theta)$ for the full quantal calculations was defined in terms of the semiclassical relation

$$\sigma_{0^+,I^+}(\theta) = P_I(\theta) \sqrt{\sigma_{0^+}^{OPT}(\theta)\sigma_{I^+}^{OPT}(\theta)} , \qquad \text{(III-16)}$$

where $\sigma_{0^+,I^+}(\theta)$ is the inelastic differential cross section and $\sigma_{I^+}^{OPT}(\theta)$ and $\sigma_{0^+}^{OPT}(\theta)$ are the optical model differential cross sections for $W_0 = 0$ and the appropriate channel energy, all evaluated for $\theta = 180°$. Figure III-9 contains comparisons of calculations of the excitation probabilities $P_I(180°)$ as a function of laboratory energy using the $J = 0$ classical and quantum methods, as well as the full quantum technique. For $E_{LAB} < 160$ MeV, the Coulomb potential completely dominates. For $E_{LAB} \geq 185$ MeV nuclear absorption strongly attenuates the excitation probabilities. In both quantum calculations the model space was truncated at the 16^+ state, assuring convergence for transitions to the 12^+ state. No equivalent truncation problem exists in the CLSM formalism.

In Figure III-9 excellent agreement is found between the CLSM and $J = 0$ quantum-mechanical calculations across the whole energy range, up to the 12^+ state, i.e., well inside the classically forbidden region. The close agreement between the two quantal calculations for reactions exciting spins up to the 8^+ state indicates the monotonic and classical nature of the deflection function, as discussed by Glendenning (1975). For higher spin states, classically forbidden at back angles, one observes an increasing systematic difference across the whole energy range between the $J = 0$ and full quantum-mechanical results.

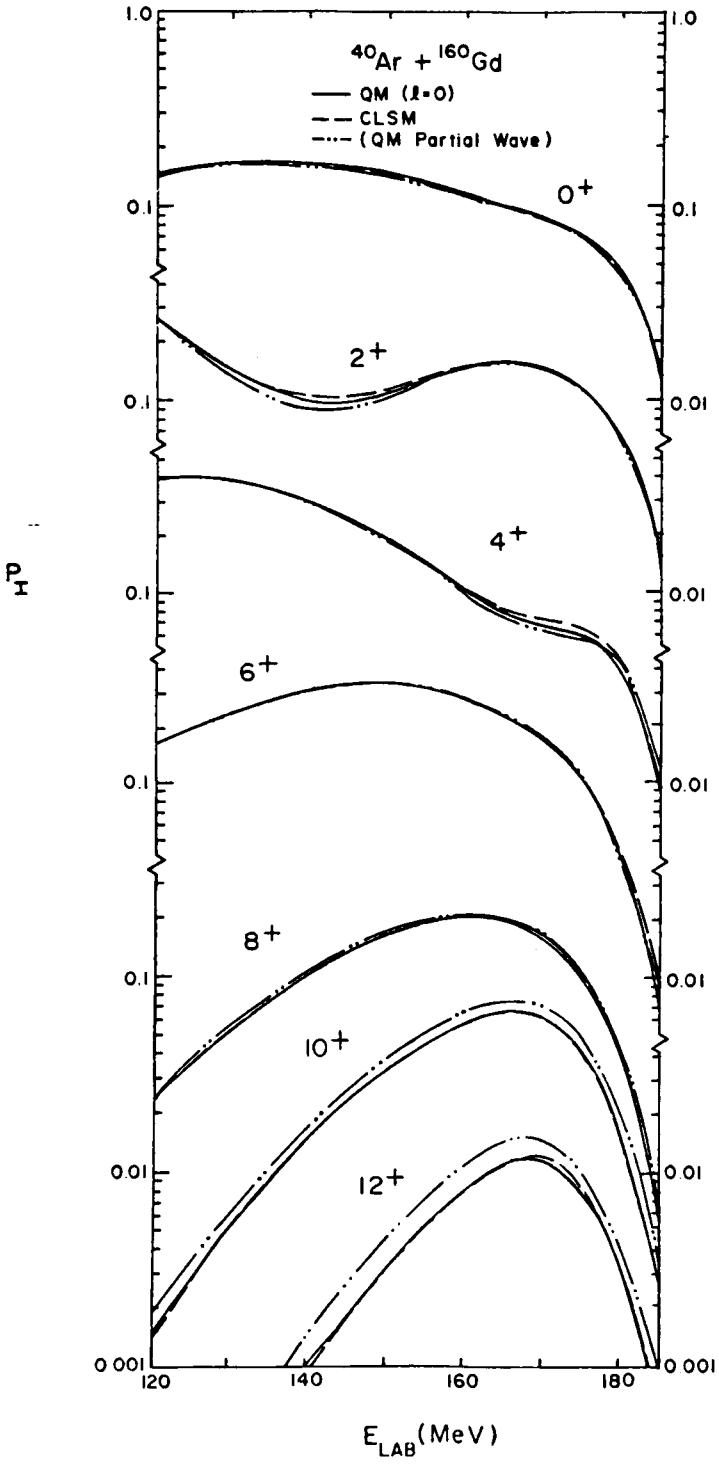


Figure III-9. Excitation probabilities calculated with the potential described by Eq. III-14. The solid curve represents the quantal excitation probabilities calculated with J = 0 only. The dashed curve is the J = 0 CLSM results. The dot-dashed curve is the result of the full quantal calculation summed over many partial waves.

These results have several important implications:

1. They confirm the accuracy of the classical-limit formalism for the J = 0 S-matrix elements in a domain where one expects the radial and collective degrees of freedom may be described with classical dynamical equations. This is true even when the complex nuclear potential, a concept alien to classical physics, dominates the reaction mechanism. The excellent agreement between the quantal and classical-limit calculations for J = 0 in the classically forbidden region implies the accuracy of the analytical continuation method used.

2. For the classically-allowed transitions, the close agreement between all three calculations for the excitation probabilities shows that just a single J = 0 classical-limit or quantal calculation is sufficient to analyze such back-angle experimental data. In fact, for J = 0, the angular momentum selection rules reduce the quantal calculation to the solution of only one set of nine coupled equations for this problem. Hence, the quantal technique is a practical alternative to classical-limit calculations.

3. For low-spin states, the small difference between the quantal J = 0 calculation and the full quantal calculation summed over many partial waves implies a monotonic and classical nature for the deflection function (Glendenning, 1975). This lends further evidence for the concept of radial and surface angular localization in very heavy-ion collisions (discussed in Chapter IV).

4. The differences between the J = 0 quantal calculations and the full quantal calculations for $P_{10^+}(180°)$ and $P_{12^+}(180°)$ show that quantum interference effects are becoming important in the partial wave

sums of Eq. III-16. Thus, although an excited rotational state with very large angular momentum tends to behave classically, the reaction mechanism to reach that state can be classically forbidden, in which case many quantum paths may contribute to the excitation probability.

It should be noted that the nuclear potential used in these calculations does not give rise to a pocket inside the Coulomb barrier. This is a property of many heavy-ion optical potentials found in the literature. For potentials with pockets, it may be necessary to add quantum-mechanical tunneling explicitly to the classical prescription.

The above comparison clearly demonstrates the complementary roles of semiclassical and fully quantum-mechanical formalisms used to treat heavy-ion inelastic scattering. The quantal calculations are rigorous to a high accuracy, although the excitation mechanism is lost in the shuffle of thousands of partial waves and coupled channels. The excitation mechanism is transparent in the semiclassical approaches, but the truly quantal effects could be glossed over. Neither approach should be preferred exclusively over the other, but rather both should serve as complementary tools for extracting nuclear structure information.

CHAPTER IV

LOCALIZATION EFFECTS IN HEAVY-ION COLLISIONS

In general, from the uncertainty relation

$$\Delta q \cdot \Delta p \gtrsim \hbar \tag{IV-1}$$

localization in a coordinate q (e.g., a generalized angle) is associated with a large uncertainty in its canonically conjugate momentum p (in our example, a generalized action). In the backward scattering of heavy ions from deformed rotors discussed here the relevant coordinate-momentum pairs (q, p) are those involving the relative radial motion in the center-of-mass system (r, p_r) and those involving the angular motion of the target nucleus (χ, p_χ). Because p_r and p_χ attain large values in such collisions, the corresponding uncertainties Δp_r and Δp_χ are expected to be large also. Hence, wavepacket descriptions are possible in which both Δr and $\Delta\chi$ are small while still being consistent with the uncertainty relation. Therefore, it is permissible to claim that expectation values of dynamical functions of r and χ which would rigorously involve integration over wavefunction amplitudes can be replaced with their localized classical counterparts (classical limit approximations).

I. RADIAL LOCALIZATION

In most heavy-ion collisions the de Broglie wavelength associated with the asymptotic radial motion of the center of mass of the colliding nuclei

$$\lambda\!\!\!^{-}_0 = \hbar/p_r^{\,0} \tag{IV-2}$$

is very small compared to some characteristic distance D. (As an illustration, for the scattering of ^{40}Ar projectiles from deformed rare-earth nuclei at energies near the Coulomb barrier, $\lambda\!\!\!^{-}_0 \approx 0.1$ fm.) For collisions below the Coulomb barrier one may take

$$D \gtrsim 2\eta\lambda\!\!\!^{-}_0 \ , \tag{IV-3}$$

where the η is the Sommerfeld parameter defined in Chapter III. For collisions around the Coulomb barrier

$$D \gtrsim R_1 + R_2 \ , \tag{IV-4}$$

the sum of the nuclear radii. Typically, for heavy-ion collisions $D/\lambda\!\!\!^{-}_0 \gtrsim 10^{-2}$ (Hodgson, 1978, Table 1.1.1). Thus, it is possible to form wavepackets of dimension small compared to D which still contain enough waves to insure a reasonably well-defined momentum. Further, if the wavepacket is sufficiently narrow, it will not break up in the scattering field. For a Gaussian wavepacket of width σ the above two conditions are satisfied if (Broglia and Winther, 1972a)

$$\lambda\!\!\!^{-}_0 << \sigma << D \ . \tag{IV-5}$$

Thus, the scattering problem can be solved rather accurately for the case of heavy ions using semiclassical equations to describe the process (Ford and Wheeler, 1959a, 1959b; Strutinski, 1964; Broglia and Winther, 1972a, 1972b, 1981; Harney, Braun-Munzinger, and Gelbke, 1974; Glendenning, 1975; Hodgson, 1978).

In the true experimental situation the wavepackets produced by accelerators may be somewhat larger than necessary to satisfy Eq. IV-5. However, Rook (1974) has shown that a semiclassical description is valid

even for large wavepackets. Physically this arises because each portion of the initial large wavepacket moves along its own classical orbit and after the reaction there is no interference between parts of the wavefunction which originate from different portions of the initial wavepacket. Portions corresponding to different orbits do not interfere because they end at different positions while portions corresponding to different positions on the same orbit reach the detector at different times. Thus a large wavepacket can be treated as a superposition of small wavepackets, all of which satisfy Eq. IV-5.

Some concern might be expressed over the argument that close to the classical turning point the radial velocity becomes small so that $\chi \to \infty$ causing the wavepacket to disperse in this region. Such reasoning is fallacious as can be seen from the motion of a free particle described in spherical coordinates where the centrifugal potential also gives rise to a turning point in the radial motion (Broglia and Winther, 1972b). Further, for particles moving in a Coulomb potential, there is a focusing effect which tends to shrink the wavepacket in the radial direction near the turning point (Broglia and Winther, 1972b). (There is also a wavepacket in momentum space, for which the expectation value of the momentum $\langle p \rangle$ can go to zero resulting in a singularity in χ. However, the passage of $\langle p \rangle$ through zero creates no singularity in the motion of the wavepacket. Consider, for example, a Gaussian wavepacket with $\langle p \rangle = 0$: its width increases regularly with time and at approximately the same rate as if it were moving in a slowly varying potential.) Thus, so long as the scattering is confined to the CNI region where only the smoothly-varying tail of the nuclear potential is felt the inequality

in Eq. IV-5 will not be violated and the wavepacket description will be valid even at the turning point. [Goldberg, Schey, and Schwartz (1967) provide elementary heuristic examples of one-dimensional Gaussian wavepackets impinging on square wells and barriers which show that the packets are not totally destroyed at the turning point.]

Because there will be strong absorption for appreciable overlap of the nuclei, the ion-ion interaction will be dominated by contributions from the nuclear surfaces. [Moffa, Dover, and Vary (1976) report a method of determining the radial extent of this surface region for heavy-ion elastic, inelastic, and transfer reactions.] This leads to a picture of the ion-ion interaction in terms of classical-like particles (center-of-mass motion defined by narrow wavepackets) interacting at their mutually well-defined surfaces. In this surface region of the potential the interaction increases rapidly with decreasing separation and the excitation is expected to be dominated by the potential near the turning point. Then to a good approximation different incident energies (different turning points) probe different radial regions of the nuclear surface, as shown schematically in Figure IV-1.

II. ANGULAR LOCALIZATION

Wavepacket analyses similar to those for the radial motion are possible for the conjugate pair (χ, p_χ). The angular wavepackets would be defined in terms of $\mathcal{D}$-functions rather than radial wavefunctions. If one makes the definition

$$I = p_\chi/\hbar \ , \qquad \text{(IV-6)}$$

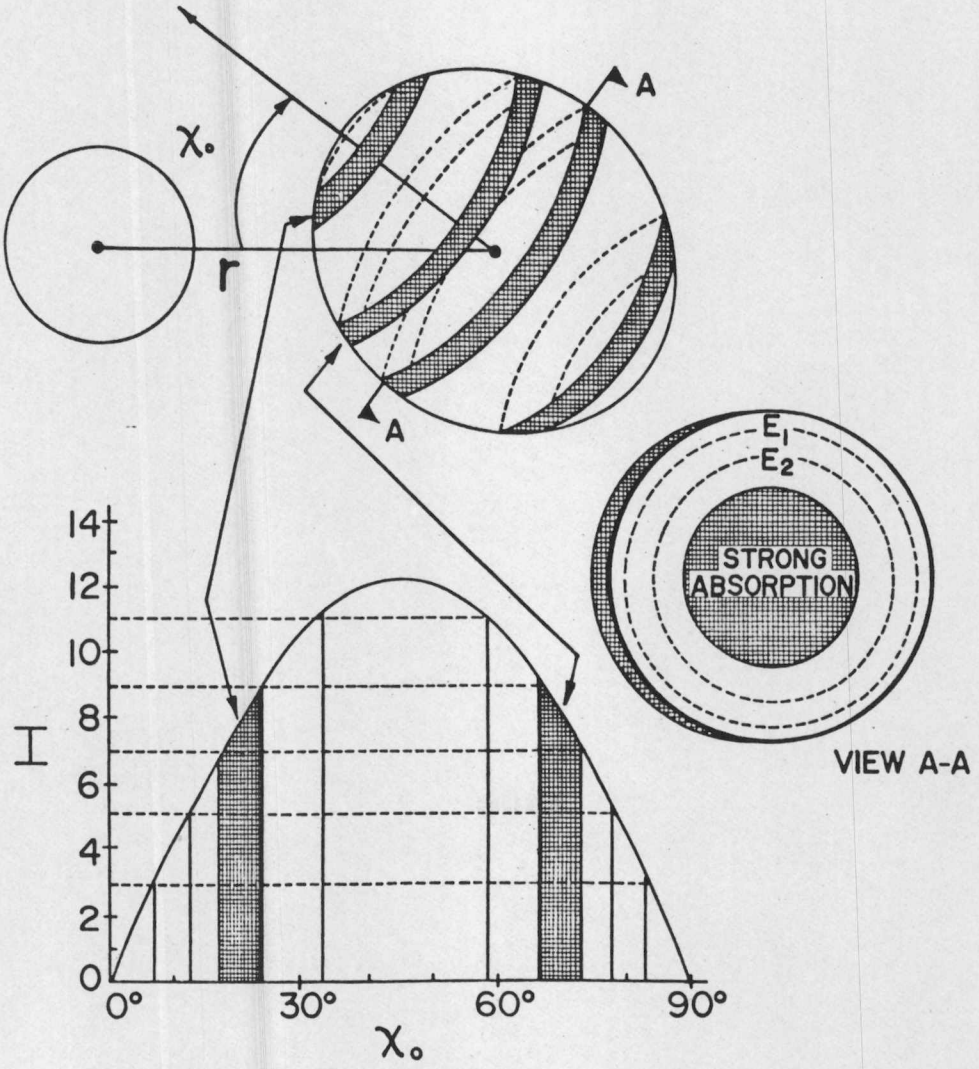


Figure IV-1. Schematic illustration of radial and angular localization in heavy-ion collisions. Different beam energies probe different radii of the ion-ion potential (view A-A). Different spin states probe different angular regions of the ion-ion potential, as determined by the roots of the quantum-number function.

an angular analogue of the de Broglie wavelength (Eq. IV-2) is given by

$$\delta_0 = \frac{\hbar}{p_\chi} = \frac{1}{I} , \qquad \text{(IV-7)}$$

where I is the value of the spin in the interaction region (which is approximately one-half of the value of the final spin). If $\delta_0 << 1$ it is possible to form wavepackets spanning relatively small angular regions which contain enough terms to insure a reasonably well-determined angular momentum. In the scattering of ^{40}Ar from deformed rare-earth nuclei at energies near the Coulomb barrier $I \gtrsim 5$. Hence, it is possible to localize over angular regions of roughly 10-20°. For the scattering of ^{86}Kr from actinide nuclei at energies near the Coulomb barrier, $I \geq 10$ so that angular localization of the order 5-10° may be expected.

The concept of angular localization can be made more clear by studying the angular motion in the sudden-collision limit (not too far from the actual experimental situation) for which $\chi = \chi_0$, where χ_0 is the initial orientation angle of the target. The uncertainty relation becomes

$$\Delta I \cdot \Delta\chi_0 \geq 1 . \qquad \text{(IV-8)}$$

Figure IV-2 shows a plot of the excitation probability P_I versus final spin I_f for pure Coulomb excitation of ^{160}Gd by 140-MeV ^{40}Ar (arguments are similar if a nuclear potential is included). The uncertainty of the spin of the target nucleus in the interaction region, ΔI, is defined by

$$(\Delta I)^2 = \langle I^2 \rangle - \langle I \rangle^2 , \qquad \text{(IV-9)}$$

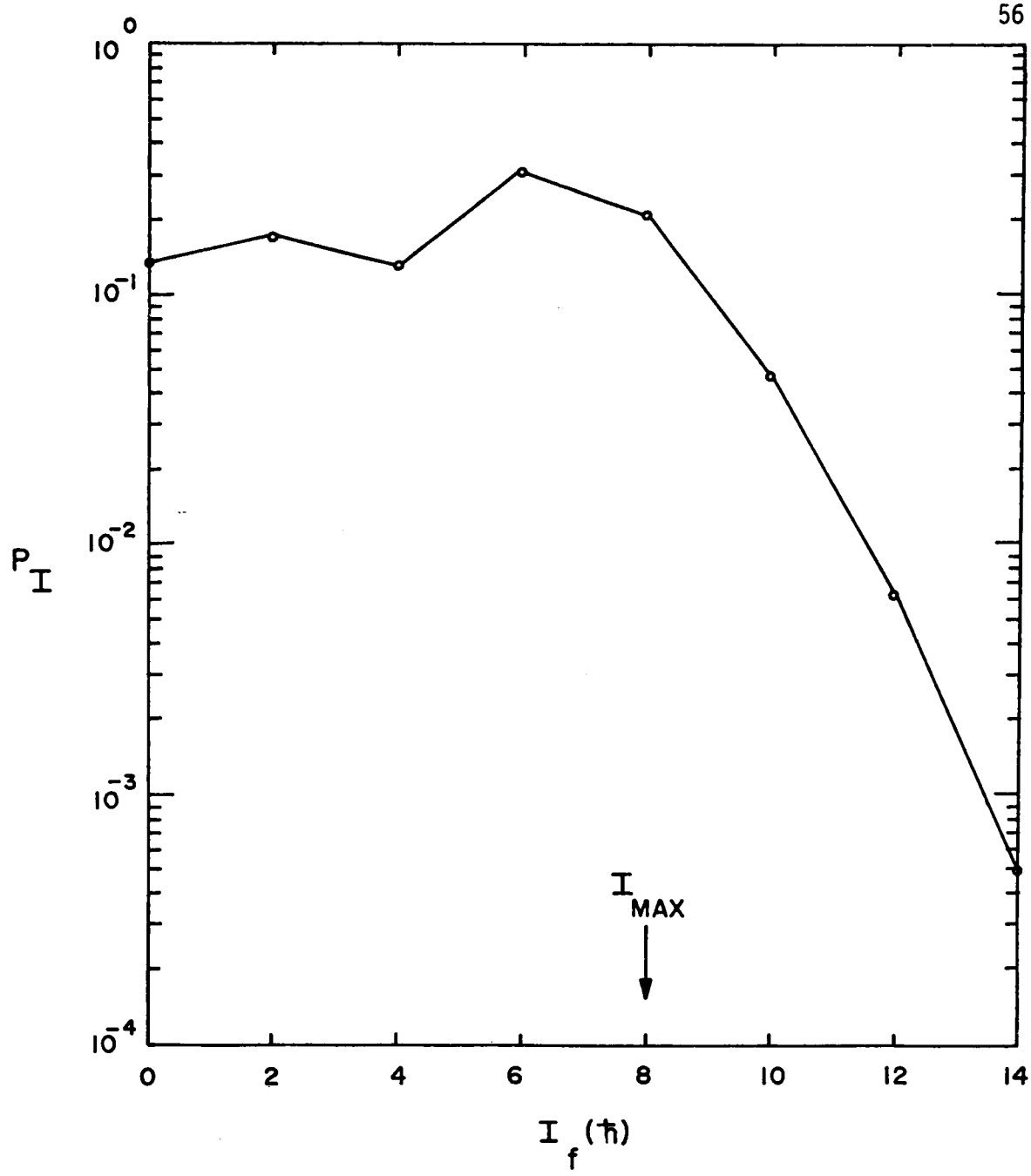


Figure IV-2. Typical plot of excitation probability P_I versus final spin I_f. The calculation is for pure Coulomb excitation of ^{160}Gd by 140-MeV ^{40}Ar projectiles. I_{max}, the maximum classically allowed spin, is indicated. Note the rapid fall of the values of P_I for $I_f > I_{max}$. Similar results are obtained if a nuclear potential is included.

where the brackets denote expectation values. The quantum-number function is odd-symmetric on the domain 0 to π, and therefore

$$\langle I \rangle \equiv 0 \ , \tag{IV-10}$$

so that only the $\langle I^2 \rangle$ term contributes in Eq. IV-9. Because the probability amplitudes defined by Eq. III-9 already contain a factor of two to account for contributions from that part of the quantum-number function in the domain $\pi/2$ to π, only positive values of I need to be considered in evaluating $\langle I^2 \rangle$. That is,

$$(\Delta I)^2 = \sum_{I=0}^{\infty} P_I \ I^2 \ . \tag{IV-11}$$

A crude estimate of ΔI can be obtained by approximating the function in Figure IV-2 as follows:

$$P_I = \begin{cases} P & I_f \leq I_{max} \\ 0 & I_f > I_{max} \end{cases} \ , \tag{IV-12}$$

where I_{max} is the maximum classically allowed final spin and where P is a constant given roughly by

$$P \approx \frac{1}{(\frac{1}{2} I_{max} + 1)} \ . \tag{IV-13}$$

The approximation (Eq. IV-12) becomes more valid as the system becomes heavier. Substitution of Eq. IV-12 into Eq. IV-11 yields

$$(\Delta I)^2 \approx P \sum_{I=0}^{\frac{1}{2} I_{max}} I^2$$

$$\approx P \frac{(\frac{1}{2} I_{max})(\frac{1}{2} I_{max} + 1)(I_{max} + 1)}{6}$$

$$\approx \frac{1}{12} I_{max} (I_{max} + 1) . \qquad \text{(IV-14)}$$

Hence, for $I_{max} >> 1$, one obtains

$$\Delta I \approx \frac{1}{\sqrt{12}} I_{max} \approx \frac{I_{max}}{4} . \qquad \text{(IV-15)}$$

Thus to a good approximation ΔI depends linearly on I_{max}; i.e.,

$$\Delta I \propto I_{max} . \qquad \text{(IV-16)}$$

Substitution of Eq. IV-10 into Eq. IV-8 yields

$$\Delta\chi_0 \propto \frac{1}{I_{max}} . \qquad \text{(IV-17)}$$

Therefore, the transfer of multiple rotational quanta implies a localization in initial orientation of the deformed rotor, and hence a localization in the part of the target nuclear surface probed by the projectile, as shown schematically in Figure IV-1. If the approximation that the uncertainty in final spin is of the order of the spacing between members of the ground-state rotational band ($2\hbar$) is made, a corresponding uncertainty may be projected onto the χ_0 axis. From Figure IV-1 and Eq. IV-17 it is again clear that the higher the quantum-number function (greater average angular momentum transfer), the greater will be the localization in the initial orientation angle χ_0. Therefore, large

angular momentum transfer implies a localization in the region of the deformed nuclear surface presented to the incoming projectile. This implies that excitation of a particular spin state of a deformed nucleus corresponds, in the classical limit, to probing certain localized regions of its surface. This angular localization in the surface region will be greatest for very heavy-ion projectiles (e.g., ^{40}Ar) and considerably smaller for less massive projectiles (e.g., ^{4}He).

Donangelo et al. (1981) have demonstrated that common approximations to the deformed ion-ion potential manifest themselves in strongly state-dependent effects. This response to the shape of the potential is interpreted as evidence for angular localization during heavy-ion collisions. They consider a comparison of CLSM calculations using two parametrizations of the nuclear potential which possess slightly different shapes. The first of these is the first-order Woods-Saxon expansion potential (Bohr and Mottleson, 1975) previously defined in Section IV of Chapter III in Eqs. III-14 and III-15. The second is the deformed Woods-Saxon potential defined by Eq. II-13. The same parameters used by Rhoades-Brown et al. (1981) [see Section IV of Chapter III] were employed in these calculations, and the same values for the constituent parameters were used in both potentials.

Figure IV-3 shows the excitation probabilities for backward scattering as a function of the incoming projectile laboratory energy, calculated for the two potentials under consideration. At low energies both calculations agree for all spins, since for energies $E_{LAB} \lesssim 160$ MeV the colliding nuclei do not get close enough to be inside the range of the nuclear force. The effects due to the particular approximation of

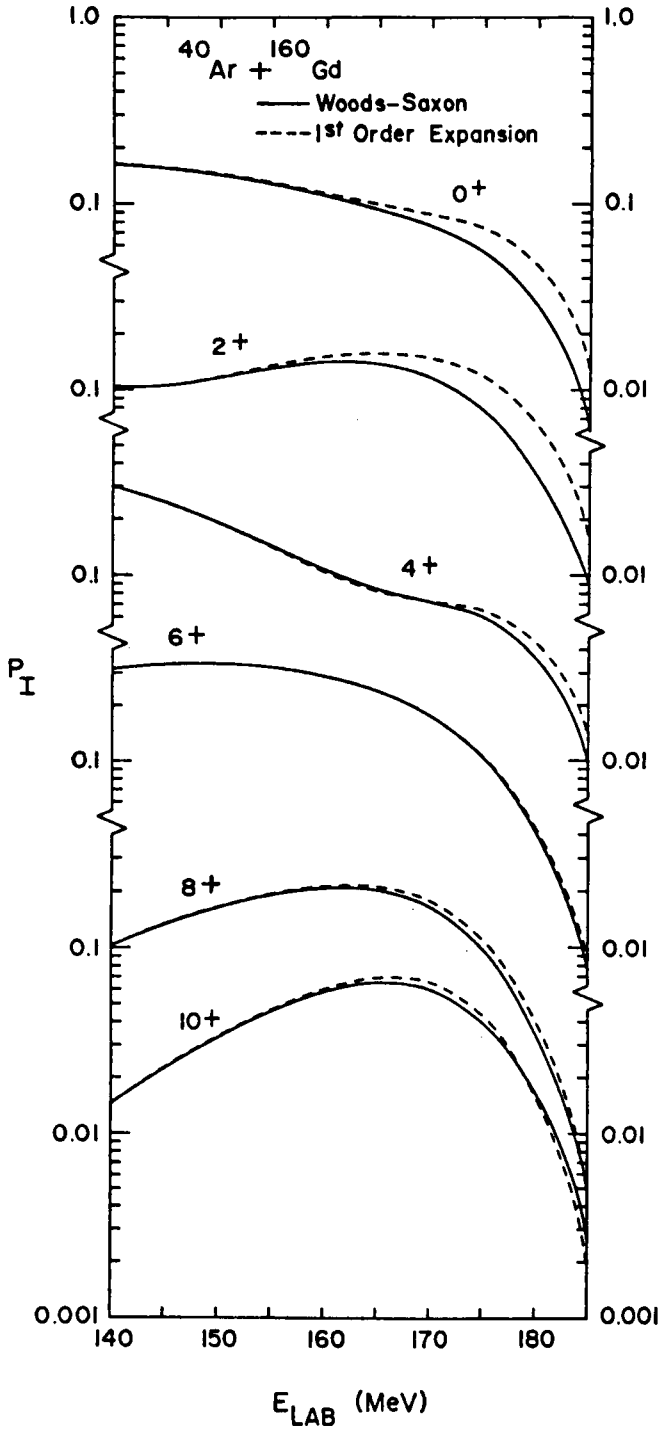


Figure IV-3. Comparison of the J = 0 CLSM excitation probabilities calculated for the deformed Woods-Saxon potential and the first-order expansion potential.

the potential are felt most in the Coulomb-nuclear interference (CNI) region, $160 \lesssim E_{LAB} \lesssim 190$ MeV. At higher energies the excitation probabilities are almost completely damped out due to competition of rotational excitation with other channels (nuclear absorption).

In the CNI region the excitation probabilities for both potentials show differences which are seen to depend on the spin of the states considered. For spins 0^+ and 2^+ there are marked differences, which become much smaller for spin 4^+. The probability curves obtained with both potentials are essentially the same for spins 6^+ and above. These results can be understood by considering the actual shape of the two potentials involved. In Figure IV-4 the 0.1 MeV and 1.0 MeV equipotentials for the deformed Woods-Saxon and the first-order expansion potentials are plotted for the $^{40}Ar + {}^{160}Gd$ case described above. The differences between the two potentials are most pronounced in the polar ($\theta \sim 0°$, horizontal axis on the figure) and the equatorial ($\theta \sim 90°$, vertical axis) angular regions. The difference in the excitation probabilities as a function of the state spin may then be understood in terms of the angular localization concept discussed previously. Different final spins probe different angular regions on the nuclear surface. The mean orientations associated with excitation of a given angular momentum state are indicated in Figure IV-4. These orientations are readily deduced by solving Hamilton's classical equations for the system as described in Section I of Chapter III. Low spins are associated with angles near 0° and 90°, where the potentials differ the most. For high spins, corresponding to intermediate

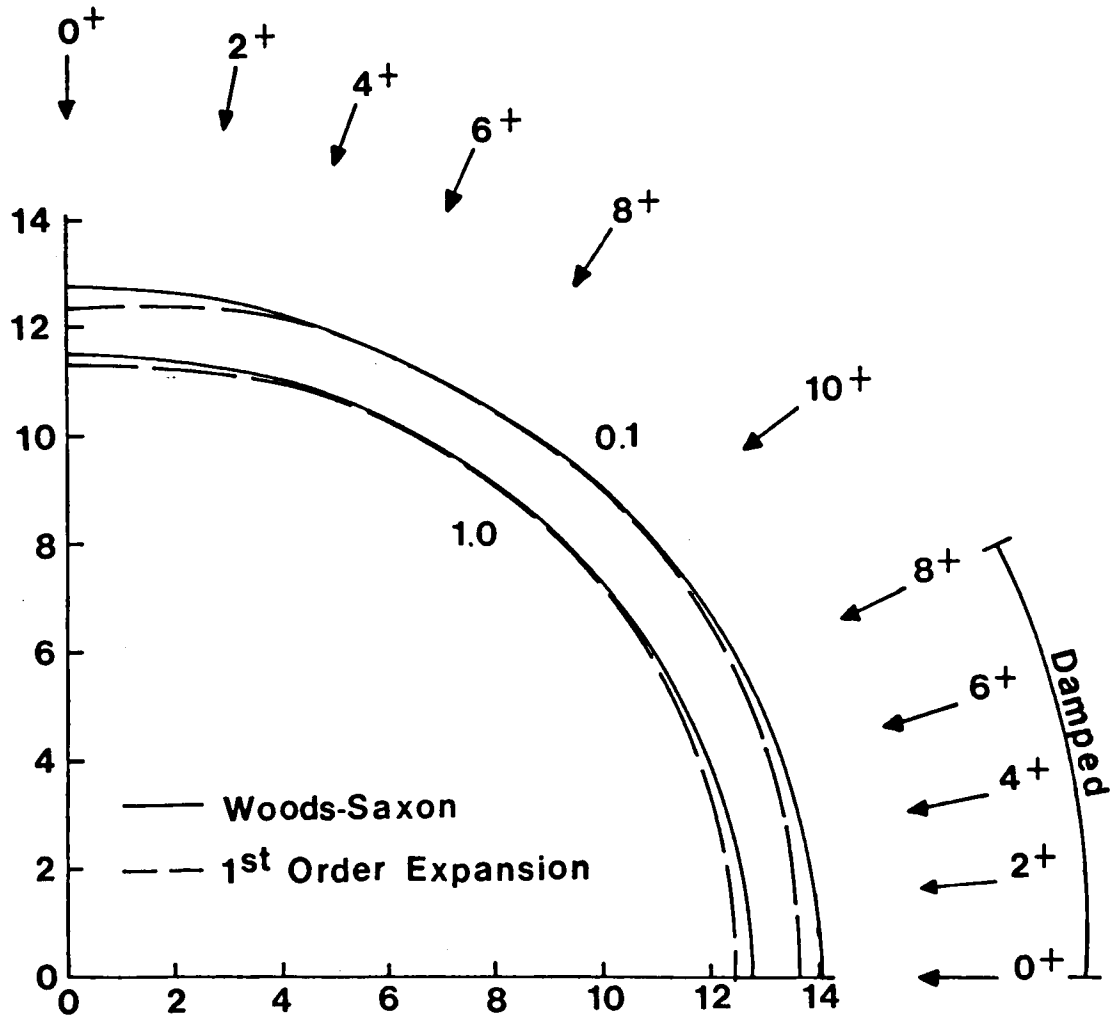


Figure IV-4. Polar plot of the nuclear potential shapes considered in the calculations presented in Figure IV-3. The rotational symmetry axis coincides with the horizontal coordinate axis. The horizontal and vertical axis are in units of fermis. The regions of the ion-ion potential relevant for excitation of particular rotational states are indicated by arrows.

orientations, the potentials almost coincide. Hence, the differences between the calculations shown in Figure IV-4 are just another manifestation of angular localization. Note that of the two orientations associated with spins 0^+-8^+, the one closer to the equatorial ($\theta \gtrsim 90°$) plane dominates due to the damping of the contribution nearer the polar orientation because of closer approach of the nuclear surfaces in this plane and hence a stronger absorptive effect in the collision. For spins 10^+ and above, only one angular region is expected to contribute in this example.

The above results show that approximations to the shape of ion-ion potentials lead to effects which are strongly state dependent. These effects will be more pronounced for larger deformation parameters and for more sensitive processes such as transfer reactions. The concept of orientation-angle localization of rotors in heavy-ion collisions provides a simple and accurate explanation for these state-dependent phenomena. This extreme sensitivity to the angular localization will be exploited in the technique discussed in Chapter VI.

CHAPTER V

EXPERIMENTAL TECHNIQUES AND DATA REDUCTION

The experimental approach discussed here is based on the general principle of using intermediate-resolution (MeV) particle detection to define projectile energies and high resolution (keV) γ-ray spectroscopy to determine the intensity with which various levels are populated. This approach bypasses the severe resolution problems encountered in traditional charged-particle spectroscopy with heavy ions due to the closely-spaced levels of a rotational nucleus.

I. THE PARTICLE-γ COINCIDENCE METHOD

The schematic experimental setup is shown in Figure V-1. Beam particles scattered from the thick target were detected by an annular silicon detector of surface area $\sim$ 200 mm^2 and depletion depth sufficient to completely stop the heavy ions. In the standard geometry the annular detector subtended an angular range of $\sim$160-176° with an average scattering angle $\theta \sim 166°$ in the lab system. The particle detector was typically covered with a 1.6 mg/cm^2 Au foil to shield against electrons and x-rays.

The scattering chamber is shown schematically in Figure V-2. It was attached via a vacuum-tight screw fitting to a lead-lined brass snout, which in turn was attached to the beam line (see Figure V-3). The thick targets were tack-welded to nickel spinnings which fitted onto an O-ring pressure seal. The beam was collimated onto the target by a 4-mm diameter tantalum tube which entered through the center hole of the

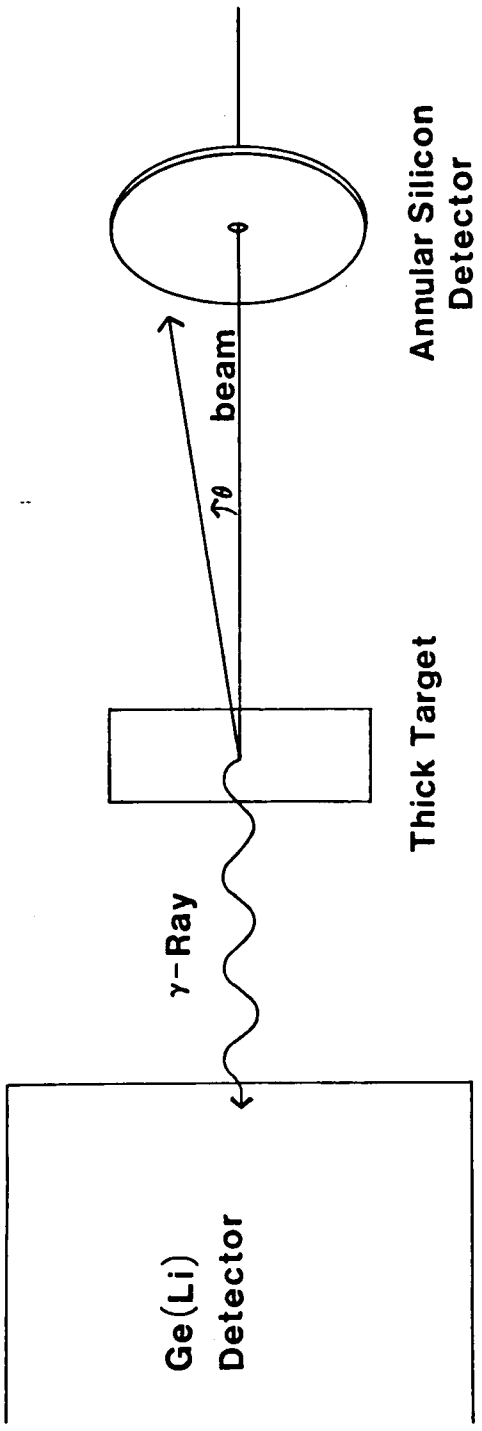


Figure V-1. Schematic diagram of the experimental arrangement.

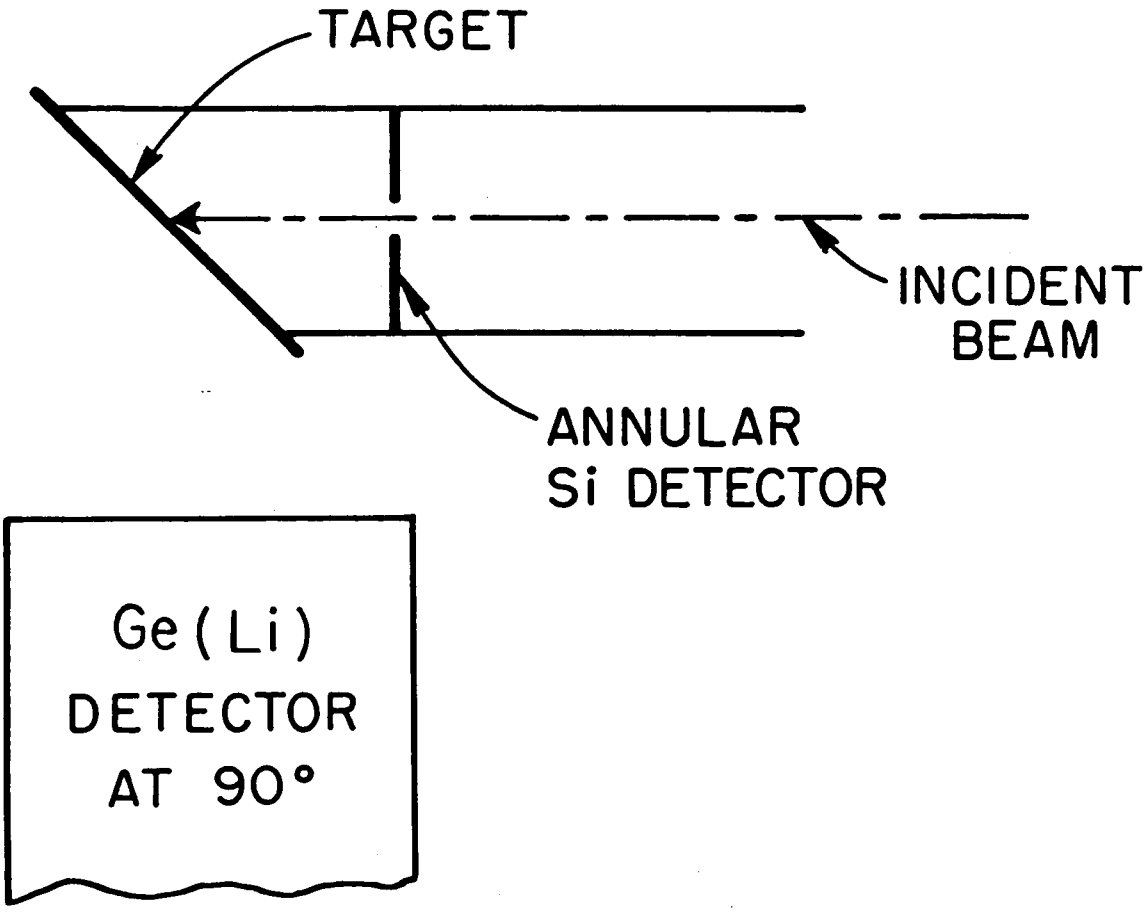


Figure V-2. Schematic diagram of the scattering chamber. The target was inclined at an angle of 45° with respect to the beam direction. For reference, a Ge(Li) detector is shown in a 90° configuration.



Figure V-3. The scattering chamber, snout, and beam-line plumbing for a typical experimental configuration. The Ge(Li) detector is shown in a 90° configuration.

annular silicon detector. The tantalum collimator was electrically insulated from the aluminum scattering chamber. Copper washers were used for electrical contact to the silicon detector. Typically, the chamber was operated at a pressure of $\sim$ 1-2 x 10^{-6} torr.

Three separate experiments were performed using ^{40}Ar ions. Two used beams produced by the Oak Ridge Isochronous Cyclotron (ORIC) while the other used beams produced by the Lawrence Berkeley Lab 88" Cyclotron. In these experiments data were acquired for ^{156}Gd, ^{160}Gd, ^{162}Dy, ^{164}Dy, and ^{180}Hf targets. Table V-1 lists the targets used and associated beam energies for the three experiments, hereafter referred to as ORIC I, ORIC II, and LBL I.

TABLE V-1

TARGET AND BEAM-ENERGY COMBINATIONS USED IN THE EXPERIMENTS

Experiment	Targets	Beam Energies (MeV)
ORIC I	^{156}Gd	160.7
	^{160}Gd	122.0, 160.7
	^{162}Dy	160.7
	^{164}Dy	160.7
ORIC II	^{156}Gd	145.9, 157.2, 158.7
	^{162}Dy	145.9
	^{164}Dy	145.9
LBL I	^{160}Gd	174.3
	^{162}Dy	174.3
	^{180}Hf	174.3

In each experiment the particle detector was operated in coincidence with three coaxial Ge(Li) γ-ray detectors of 14-18% detection efficiency relative to a 7.6 cm by 7.6 cm NaI crystal and resolution

2.0-2.3 keV FWHM for the 1333 keV ^{60}Co line. A block diagram of a typical electronic arrangement is displayed in Figure V-4. Table V-2 summarizes the Ge(Li) detector geometries used in the experiments. All distances in Table V-2 were measured in the reaction plane from the target center to the center of the detector face and all angles are measured relative to the beam direction. In most cases absorbers were placed over the ends of the Ge(Li) detectors to decrease the count rate for low-energy γ-rays. (A typical absorber consisted of a 4 mil Pb, 6 mil Sn, 3 mil Cu sandwich.) In addition, lead anti-Compton shields were placed between the Ge(Li) detectors because of their close spacing.

Data were taken in particle singles and in particle-γ coincidence modes. In the ORIC I experiment particle singles data were stored in a Canberra 4096 multichannel analyzer and coincidence data were stored on magnetic tape via a PDP 11/05 minicomputer using the Tennecomp PACE system (Kahler, 1978) operated in coincidence mode only. [The PACE system uses a single high-speed ADC (analog-to-digital converter) to digitize electronically stretched and multiplexed input signals.] In the ORIC II experiment the PACE system was operated simultaneously in the singles and coincidence mode. Particle singles were stored in-core on the PDP 11/20 and coincidence data were written onto magnetic tape. In the LBL I experiment particle singles were stored in an external 4096 multichannel analyzer and coincidence data were written onto magtape via the installation Modcomp computer. (In the LBL I experimental arrangement a single multiplexed ADC system was used for the coincidence data and a slightly different electronic gating technique was employed.) In all cases the coincidence data consisted of seven digitized parameters: three Ge(Li)

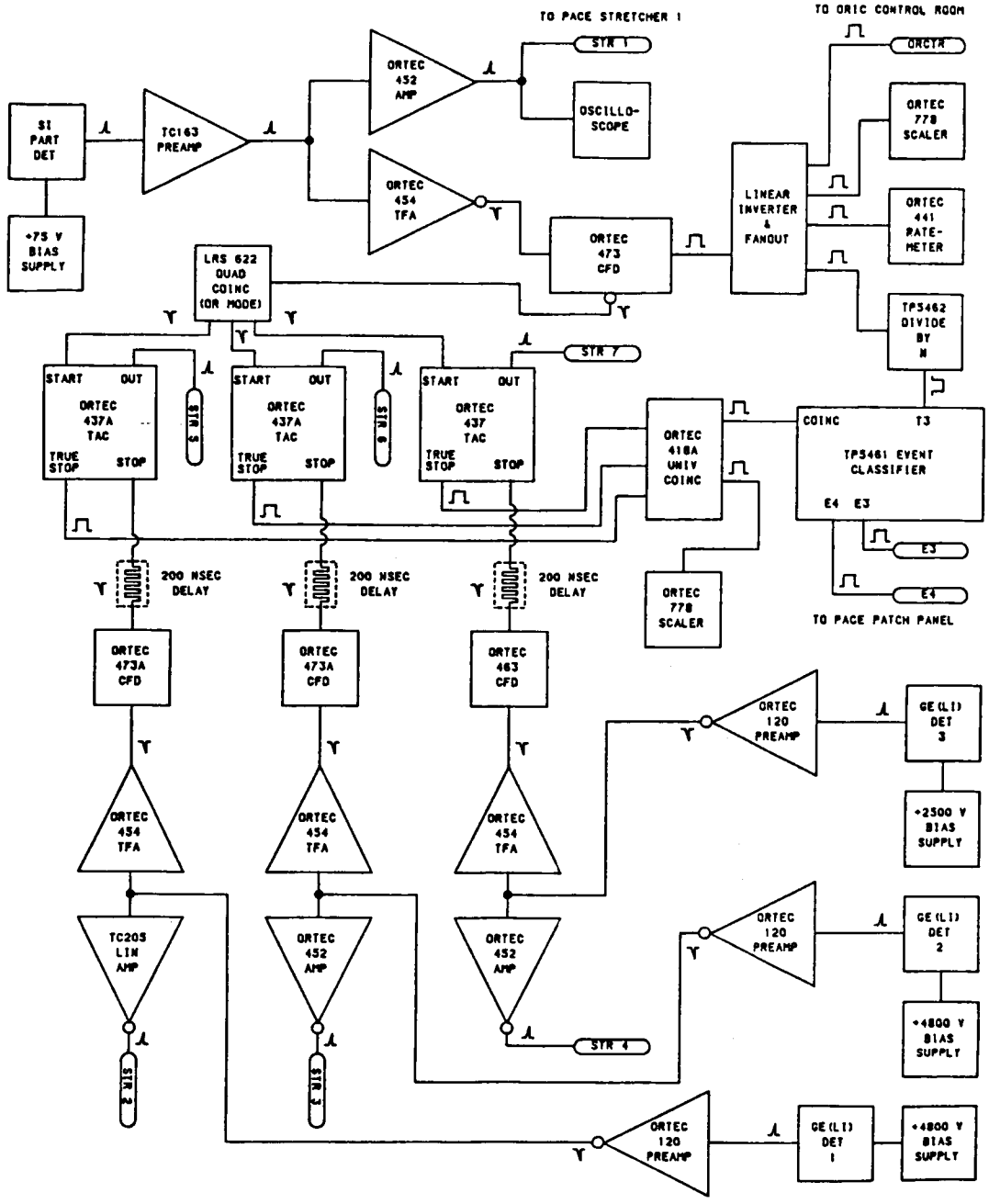


Figure V-4. Block diagram of typical particle-γ coincidence electronics. This particular arrangement was used in the ORIC II experiment.

TABLE V-2

Ge(Li) DETECTOR GEOMETRIES USED IN THE EXPERIMENTS

Experiment	Ge(Li) Detector Number	Detector Angle (Degrees)	Target-to-Detector Distance (cm)
ORIC I	1	0	6.0
	2	90	4.5
	3	-90	4.0
ORIC II	1	0	5.0
	2	90	3.5
	3	-90	3.5
LBL I	1	73	4.5
	2	-90	4.0
	3	0	4.0

detector energy signals, three particle-Ge(Li) TAC (time-to-amplitude converter) signals, and a backscattered-particle energy signal.

In the collision of a ^{40}Ar projectile with a rare-earth target nucleus at energies near the Coulomb barrier the recoil velocity of the target nucleus is small when compared to the speed of light ($v_{recoil}/c << 1$). Therefore the γ-ray spectra corresponding to decay of the excited recoiling target nucleus show little Doppler broadening. In such cases considerable time can be saved if a "thick" target is used. (A "thick" target is one which is thick enough to stop the incident beam.) Figure V-5 shows a schematic diagram of a typical particle spectrum for backward scattering of a heavy-ion beam from a thick target. By using elastic kinematics and tabulated stopping powers (Northcliffe and Schilling, 1970; Hubert et al., 1978, 1980) it is possible to divide the thick-target particle spectrum into bins which correspond to different excitation depths and hence different effective incident energies in the target (see Figure V-5). Therefore the excitation function can be determined by a single measurement over a range of energies. In particular, the energy deposited in the particle detector is related to the effective incident energy on a nucleus in the target by the formulae of Appendix C. Figure V-6 shows a typical example of the smooth and monotonic relationship between the energy deposited in the detector and the energy incident on a nucleus in the thick target.

The particle detector was calibrated by scattering the beam from thick targets composed of nuclei for which the "safe" energy was greater than the experimental beam energy (e.g., Ta, Au, Pb, and Th). The "safe" energy is that energy below which only Coulomb effects are observed and above which nuclear interference becomes apparent. (Appendix D contains a

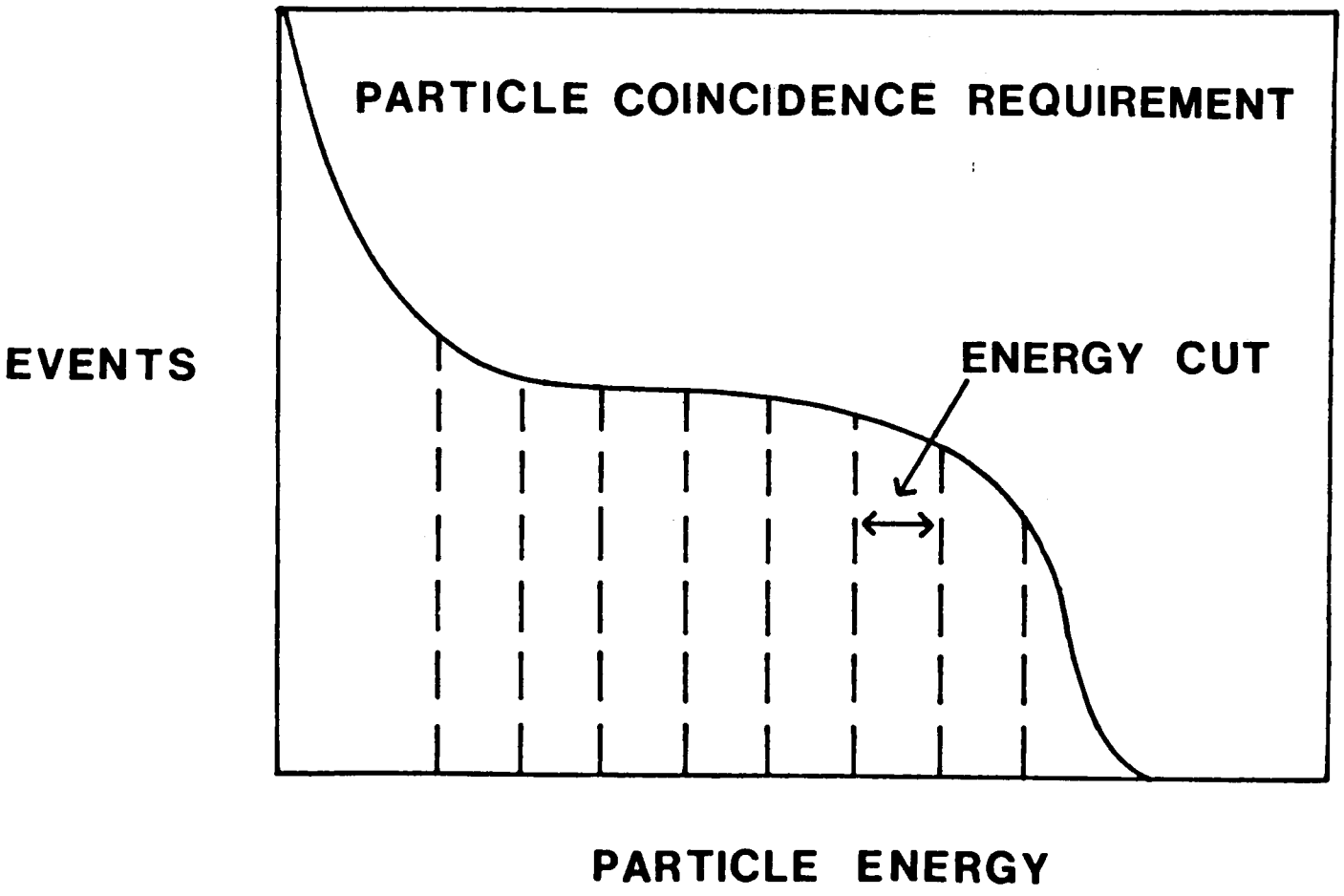


Figure V-5. Schematic diagram of a thick-target backscattered-particle spectrum. Particle energy coincidence requirements permit sectioning of the spectrum into bins corresponding to different incident energies in the target material.

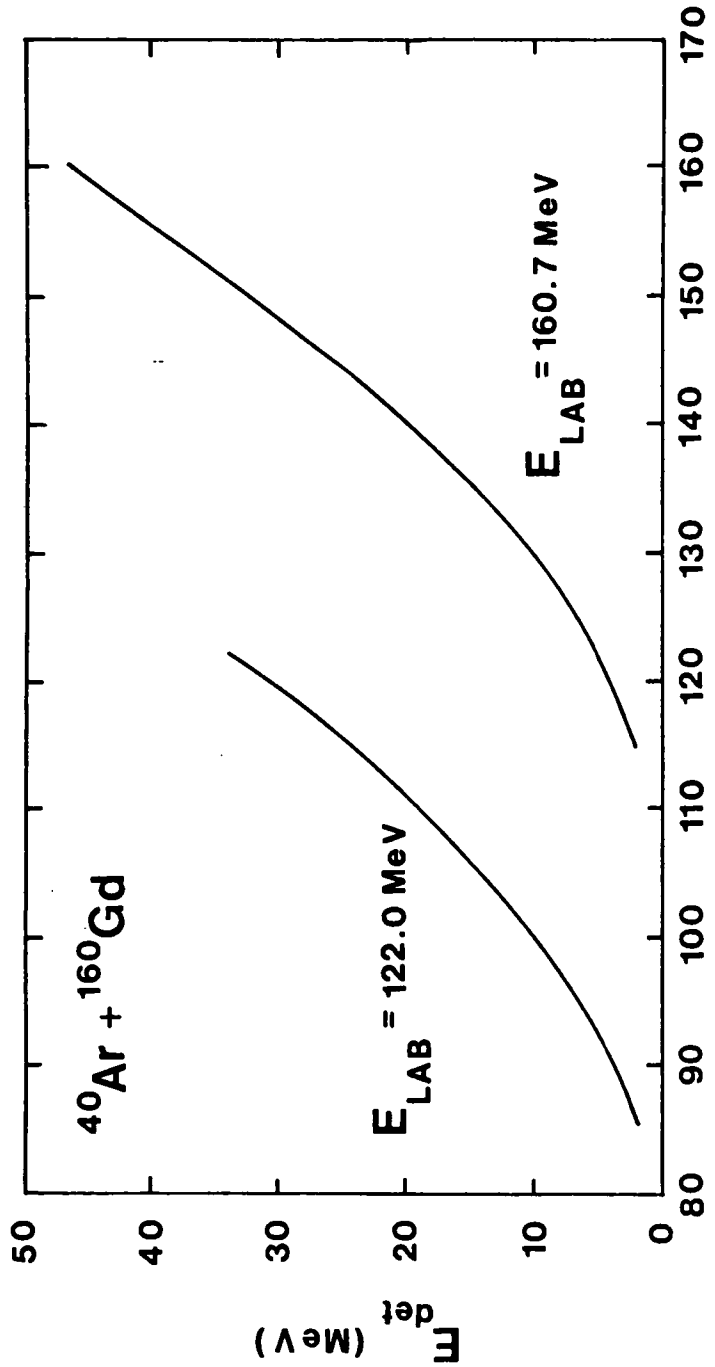


Figure V-6. Examples of E_{det} versus E_{inc} curves. The calculations were made using the relations in Appendix C for $^{40}Ar + ^{160}Gd$ at the two beam energies indicated. The annular particle detector was covered with a t = 1.66 mg/cm^2 Au foil.

discussion of a simple method developed to estimate the safe energies for experiments involving the scattering of deformed nuclei.) The energies for the calibration points were calculated using the relations in Appendix C for scattering from the front edge of the target. To account for edge effects the channel number used in the calibration was chosen to be that for which the high-energy (high-channel) edge of the particle spectrum (see Figure V-5) had fallen to half of its initial value in the drop-off region. Figure V-7 shows a typical calibration curve which illustrates the linearity of the particle detector.

The intrinsic resolution of this particle detection system was estimated by Guidry et al. (1981a) by scattering an ^{86}Kr beam from a 200 $\mu g/cm^2$ Au target. They found that the width of the resulting peak in the particle detector was comparable to that estimated from simple kinematical calculations based on the finite acceptance angle of the detector. This translated into an uncertainty in defining the incident beam energy for the excitation function of about 1%. The uncertainty in the case of ^{40}Ar beams scattering from rare-earth targets was assumed to be of a similar magnitude.

The transition energies for the ground-state rotational bands of the rare-earth nuclei studied are well known (see Table V-3). Because rather pure targets (see Table V-4) were used, the observed γ-ray spectra had very low backgrounds. Therefore, very reliable determinations of the peak areas in the particle-γ coincidence spectra were possible.

The precision of this method has been checked by comparing spectra taken at two different beam energies incident on the face of the thick target. In that case the energy cut representing scattering from the face of

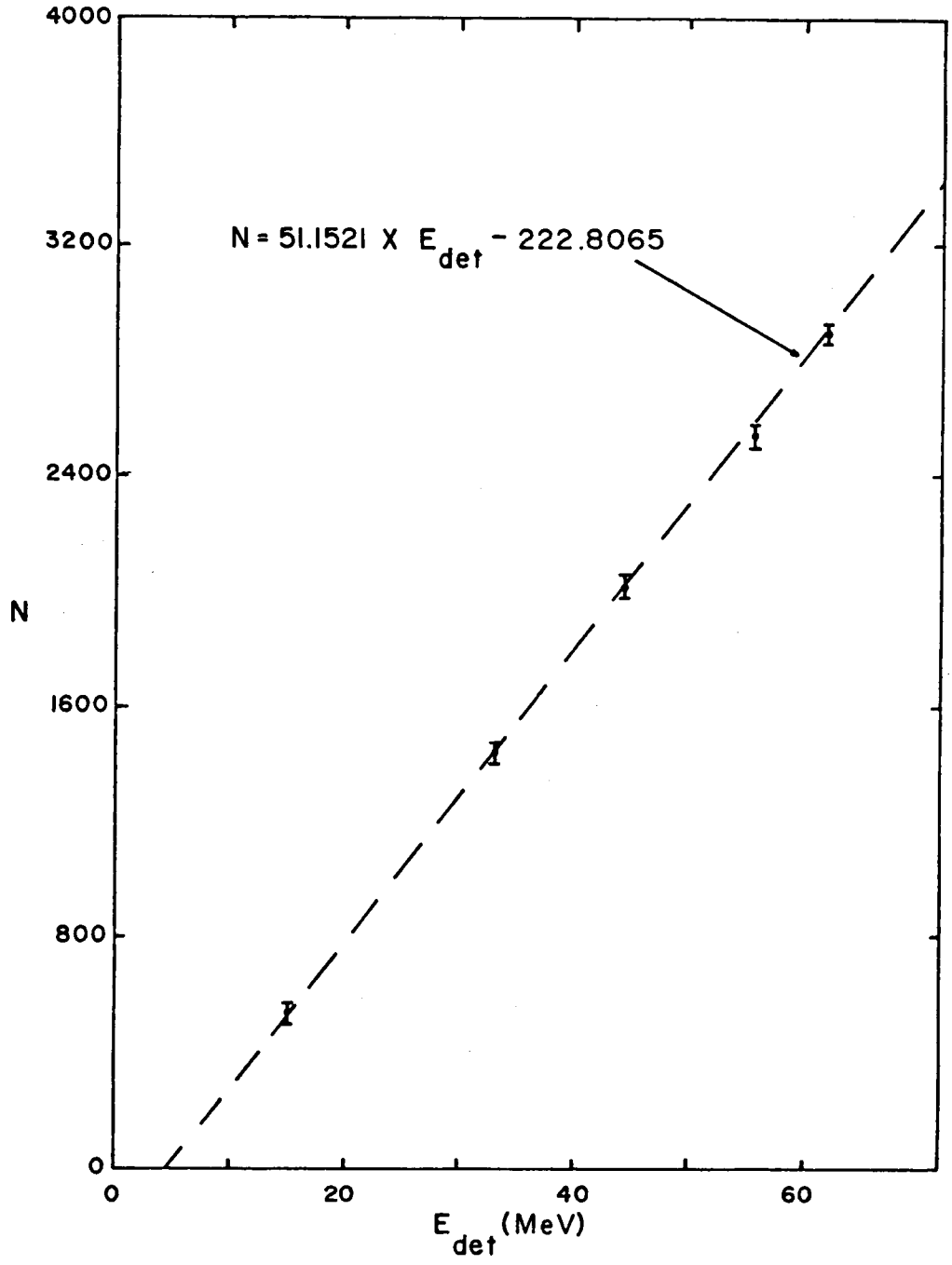


Figure V-7. Example of a particle detector calibration curve. The channel number N is plotted as a function of the energy deposited in the particle detector E_{det}. A least-squares fit to the calibration points yields the linear relation for N indicated in the upper part of the figure. This particular calibration was obtained for particle singles spectra in the ORIC I experiment.

TABLE V-3

THE TRANSITION ENERGIES OF THE GROUND-STATE ROTATIONAL BAND FOR EACH RARE-EARTH NUCLEUS STUDIED

Transition	^{156}Gd	^{160}Gd	^{162}Dy	^{164}Dy	^{180}Hf
$0^+ \rightarrow 2^+$	88.97	75.26	80.66	73.39	93.31
$4^+ \rightarrow 2^+$	199.22	172.62	185.00	168.84	215.24
$6^+ \rightarrow 4^+$	296.50	264.77	282.86	259.09	332.27
$8^+ \rightarrow 6^+$	380.6	351.11	372.75	342.35	443.17
$10^+ \rightarrow 8^+$	451.1	431.17	453.85	417.6	--

Note: The values are quoted in keV. The ^{156}Gd, ^{162}Dy, ^{164}Dy, and ^{180}Hf values are from Sayer, Smith, and Milner (1975). The ^{160}Gd values are from Lee (1978).

TABLE V-4

THE ISOTOPIC ABUNDANCES a FOR THE TARGETS USED IN THE EXPERIMENTS

Target	a (%)	Δa (%)
^{156}Gd	93.58	0.10
^{160}Gd	97.86	0.10
^{162}Dy	96.0	1.00
^{164}Dy	83.2	1.00
^{180}Hf	96.0	1.00

the target at lower energy should correspond in effective incident energy to a cut in the interior of the target at higher energy. When these comparisons were performed the overlapping data for the two cases agreed within experimental uncertainty, suggesting the essential correctness of the method of associating an energy in the particle detector with an effective incident energy in the thick target (see Appendix C). A second confirmation is provided by the fact that the low energy Coulomb excitation parts of the excitation functions determined by these methods agree well with calculated values. This places an upper limit of $\sim$1% on the energy uncertainty.

The method described here is relatively insensitive to uncertainties in the stopping powers employed. In a typical case a 20% uncertainty in stopping powers would result in only $\sim$1-2% uncertainty in relating the energy in the heavy-ion detector to the effective incident energy in the thick target.

Higher precision could be obtained by using thin targets and varying the beam energy to generate a traditional excitation function. There is a second advantage of using a thinner target in situations where the experiment is count-rate limited. Since the Rutherford cross section scales as $1/E_{cm}^2$ the thick-target particle spectrum is dominated by low-energy (Coulomb excitation) events. By using a thinner target it is possible to maximize the number of events recorded which correspond to high E_{cm} (CNI region). However, all data reported here were obtained with the thick-target method described above.

II. THE EXPERIMENTAL EXCITATION PROBABILITIES

The experimental excitation probabilities for each state were determined from the relation

$$P = \frac{1}{aN_B}\left[\frac{(1+\alpha_T)N}{\varepsilon\, W(\theta)} - T\right], \qquad (V\text{-}1)$$

where a is the isotopic abundance, N_B is the number of heavy-ions in the particle spectrum cut expected for Rutherford scattering, α_T is the total internal conversion coefficient, ε is the γ-ray detection efficiency, T is the total number of times the state in question is fed from above, $W(\theta)$ is the γ-ray angular distribution, and N is the total number of γ-rays in the peak, corrected for dead-time losses, summing, and random events.

The total number of heavy ions N_B incident with appropriate impact parameter in given energy cut was determined from the singles heavy-ion spectrum for those energies in the initial interference region where the scattering remains essentially Rutherford. For higher energies this became unreliable due to the influence of the complex nuclear potential on the Rutherford scattering. For a thick target a monitor detector at forward angles is not practical. Furthermore, the thick target in this experimental arrangement would act as a very poor Faraday cup. Therefore, the number of heavy ions N_B was determined by normalizing the low-energy Coulomb excitation part of the thick-target heavy-ion spectrum to the Rutherford cross section, as described in Appendix C. Dead-time corrections to N_B were estimated by including a live-time pulser in the particle-singles electronics. The statistical

uncertainty in N_B is proportional to $\sqrt{N_B}$. In most cases N_B was quite large so that the uncertainty in N_B was assumed to be negligible.

The total conversion coefficient α_T is defined by

$$\alpha_T = \alpha_K + \alpha_L + \alpha_M + \alpha_N + \alpha_O + \ldots . \qquad \text{(V-2)}$$

The values for α_K, α_L, and α_M were determined by interpolation from the compilation of Hager and Seltzer (1973). The values of the sum $(\alpha_N + \alpha_O + \ldots)$ were interpolated from the compilation of Dragoun, Plajner, and Schmutzler (1973). The uncertainties in the interpolated α_T values were estimated to be $\sim$3%. The $2^+ \rightarrow 0^+$ transitions for the rare-earth nuclei studied here had large α_T values (i.e., they are highly converted).

The γ-ray detection efficiencies were determined with calibrated γ-ray sources (typically NBS mixed standards). The usual practice was to afix the calibration source to one of the rare-earth targets used in the experiment such that the activity was centered over the burned spot on the target. The calibrations were timed so that absolute efficiencies could be determined from the relation

$$\varepsilon = \frac{N_a}{B_a T_c \left(\frac{dN}{dt}\right)_0 \exp\left(-0.693 \frac{t}{t_{1/2}}\right)} . \qquad \text{(V-3)}$$

In Eq. V-3, N_a is the background-subtracted peak area for a particular calibration transition, T_c is the time interval for the calibration, t is the time elapsed since the source was calibrated, $t_{1/2}$ is the half-life of the transition, and B_a is the relative intensity for the

transition which depends on the definition of $(\frac{dN}{dt})_0$. If $(\frac{dN}{dt})_0$ is a rate for a reference γ-transition, then B_a is the ratio of the absolute intensity of the transition to the absolute intensity of the reference transition. If $(\frac{dN}{dt})_0$ is a total γ-disintegration rate, B_a is the ratio of the absolute intensity of the peak to the sum of the absolute intensities of all transitions in the reference source. Efficiency calibration curves were obtained for each Ge(Li) detector. Figure V-8 shows an example of a typical efficiency curve. Note that the curve falls precipitously below a γ-ray energy of $\sim$100 keV. This feature is due to the low intrinsic efficiency of the detector crystal at those energies and to the attenuating effect of the absorbers. The $2^+ \rightarrow 0^+$ transition energies listed in Table V-3 all lie within this region. Hence, the efficiency calibration curves were not well determined for the $2^+ \rightarrow 0^+$ transitions and the associated uncertainties in ε for those transitions were quite large. The uncertainties in the efficiencies for the other transitions were estimated to be $\sim$3%.

The experimental angular distribution function $W(\theta)$ was defined as (Camp and Van Lehn, 1969)

$$W(\theta) = 1 + Q_2 A_2 P_2(\cos\theta) + Q_4 A_4 P_4(\cos\theta) , \qquad (V\text{-}4)$$

where θ is the angle between the beam direction and the Ge(Li) detector axis, the Q_i are smearing corrections due to the finite solid-angle subtended by the Ge(Li) detector, the A_i are theoretical angular distribution coefficients, and the $P_\lambda(\cos\theta)$ are Legendre polynomials. Since these experiments involve particles scattered to backward angles in the center-of-mass system, the γ-ray angular distributions should not be appreciably perturbed from those for pure Coulomb excitation. This is clear from

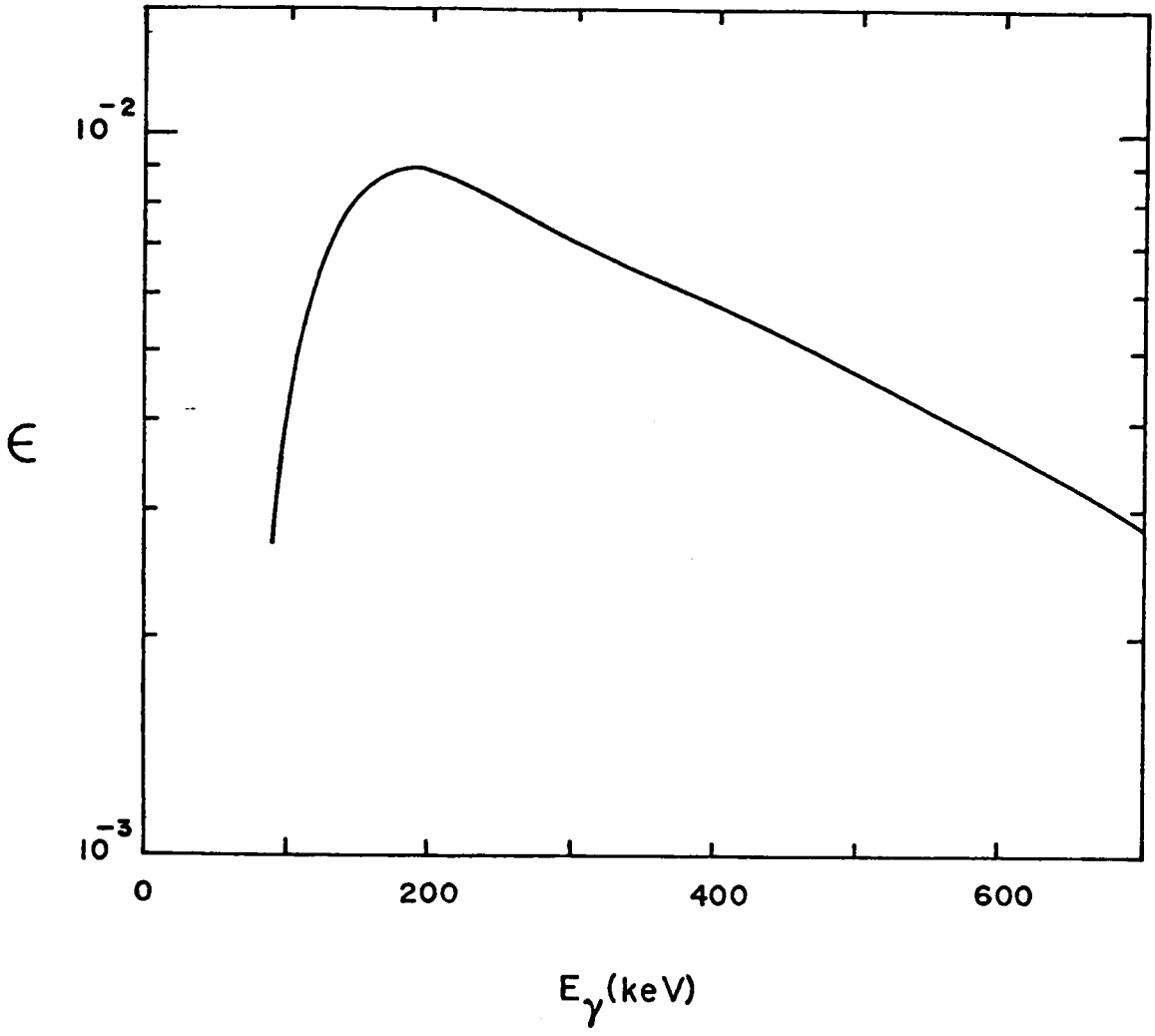


Figure V-8. Example of a Ge(Li) detector efficiency calibration curve. The absolute efficiency ε (see Eq. V-3) is plotted as a function of the detected gamma-ray energy E_γ. Note the precipitous fall of the efficiency curve for $E_\gamma \lesssim 100$ keV. This particular curve was obtained for Ge(Li) detector 1 in the ORIC I experiment.

classical considerations, since for low impact parameters the addition of a standard nuclear force to the Coulomb force can change the amount of angular momentum transferred, but not the fact that it must be transferred approximately perpendicular to the beam axis (only states with $m \sim 0$ can be populated). This conclusion is supported by coupled-channels calculations and was checked experimentally by measuring the 0°-90° anisotropy, which was found to agree with the prediction of Coulomb excitation theory within an experimental uncertainty of ~5% (Guidry et al., 1981a). Accordingly, a version of the Winther- de Boer code (Winther and de Boer, 1966) modified by Sayer (1968) for thick target Coulomb excitation (SWHETY) was used to calculate the spherical tensors from which A_2 and A_4 could be determined. [The accuracy of the Winther-de Boer code for Coulomb excitation angular distributions has been demonstrated by Eichler et al. (1973), Ward et al. (1976), and Guidry et al. (1976b, 1978b).] In general, the spherical tensors depend weakly on the energy of the projectile. However, because only an estimate of A_2 and A_4 was sought, the spherical tensors were assigned constant values determined by a single calculation for a projectile energy intermediate in the range of incident energies sampled by the thick target. The smearing corrections Q_2 and Q_4 were calculated according to the method of Krane (1973) with a computer code SOLCOR (Vassy and Smith, 1973) using the known Ge(Li) detector crystal geometries and the measured target-to-detector distances (Table V-2, p. 71). The values of $W(\theta)$ calculated with Eq. V-4 were assumed to have uncertainties of roughly 3-5%. (In experiments not performed at backward center-of-mass angles the above prescription would not be applicable and $W(\theta)$ should be measured separately).

To determine the peak areas N needed to calculate the experimental excitation probabilities with Eq. V-1, the coincidence data first had to be sorted. The ORIC I and ORIC II data were sorted on PDP 11/20 minicomputers using the intrinsic sorting software of the Tennecomp Operating System (TPOS). The LBL I data were sorted on the ORIC SEL 840-A computer with an assembly language routine written by D. C. Hensley. Gates set on the particle parameter (see Figure V-5, p. 73) were determined using the relations in Appendix C. These gates typically were chosen so that the range of incident energies sampled by the thick target was divided into two-MeV bins (the intrinsic resolution of the detection system was of this order). Additional gates were set on the TAC parameters to permit discrimination of prompt and random events. The TAC limits were determined by first building TAC spectra with gates set on the peaks of the ground-state transitions in the Ge(Li) spectra. These initial sorts revealed that in most cases the timing for the $2^+ \rightarrow 0^+$ transition was very poor, while for the other transitions the timing was excellent. Therefore, the TAC limits were determined from the sorts on the $4^+ \rightarrow 2^+$ transitions. Prompt and random spectra were constructed for each Ge(Li) detector and for all particle energy bins. The random spectra were then subtracted from the prompt spectra.

The areas of the peaks in the random-corrected spectra were determined by Gaussian peak-fitting routines. The ORIC I peak areas were obtained with the routines SKEWUP, MULTIT, and MULTUM written by J. A. Vrba in the Tennecomp Interpretive Language (used by TPOS) for the PDP 11/20. These routines were used to fit skewed-Gaussian peaks automatically to the several hundred Ge(Li) spectra resulting from the sorting operations. The ORIC II and LBL I peak areas were fit with the

normal Gaussian peak-fitting option of the analysis program LIZA written by M. L. Halbert for the ORIC SEL 840-A computer. In both programs linear backgrounds were automatically subtracted before determination of the peak areas, and both programs supplied an estimate of the statistical uncertainty of the resulting fits. In most cases this uncertainty was less than 5%.

Because no sum peaks were noticed in the sorted spectra, summing corrections to the peak areas were ignored. In an experiment where summing is a problem the prescription outlined by Heath (1964) is sufficient for estimating such corrections. Because no dead-time pulser was included in the coincidence electronics in any of the three experiments, dead-time corrections to the peak areas could not be made. The ramifications of this oversight will be discussed in the next section of this chapter.

The feeding from higher-lying states T was determined in a straightforward way by beginning the analysis at the top of the observed ground-state band. Any side feeding into the ground band was neglected. The probability for the highest state clearly seen was analyzed first with the assumption that feeding into it was negligible (T = 0). Hence, the probability determined was actually a sum of probabilities over that state and all states above it in the ground band. However, for the high-spin (classically forbidden) transitions the excitation probability drops so rapidly with angular momentum that typically more than 90% of the probability came from direct excitation of the state, with less than 10% representing probability from states above. The analysis then proceeded down the band, with the feeding T determined

(assuming no side feeding) for each successive state by the previous analysis of states above it.

The uncertainty in the experimental probability ΔP was estimated by applying the propagation of independent-errors theory to Eq. V-1:

$$\frac{\Delta P}{P} = \left\{ \left(\frac{\Delta a}{a}\right)^2 + \left(\frac{\Delta N_B}{N_B}\right)^2 + \left(\frac{1}{1-\delta}\right)^2 \left[\left(\frac{\Delta \alpha_T}{1+\alpha_T}\right)^2 + \left(\frac{\Delta N}{N}\right)^2 + \left(\frac{\Delta \varepsilon}{\varepsilon}\right)^2 + \left(\frac{\Delta W(\theta)}{W(\theta)}\right)^2 \right] + \left(\frac{\delta}{1-\delta}\right)^2 \left(\frac{\Delta T}{T}\right)^2 \right\}^{1/2}, \qquad \text{(V-5)}$$

where

$$\delta \equiv \frac{T}{\left[\frac{(1+\alpha_T)N}{\varepsilon\, W(\theta)}\right]} \qquad \text{(V-6)}$$

and represents the ratio of the feeding correction to the net intensity (both feeding and direct excitation) in the peak. At the top of the band $\delta \gtrsim 0$, whereas toward the bottom of the band $\delta \to 1$. Thus, the probabilities for the lowest transitions in the band had the largest uncertainties. The worst situation occurred for the $2^+ \to 0^+$ transition.

The particle-γ coincidence method obviously did not yield the ground state (0^+) probabilities directly (no γ-decay). Furthermore, because of (a) the large conversion coefficients, (b) low and poorly determined detection efficiencies, (c) poor timing, and (d) large uncertainties due to feeding corrections no attempt was made to determine the excitation probabilities for 2^+ states. The 2^+ can be obtained from a careful γ-ray experiment or a conversion electron-particle coincidence experiment. If all excited ground band states have been determined, the 0^+ probability (true elastic scattering) could be estimated by imposing

unitarity on the excitation probabilities in the initial interference region where the scattering is still essentially Rutherford and the imaginary potential small. (This procedure is less useful for higher energies where the imaginary potential is no longer negligible and significant deviations from a Rutherford trajectory occur.) For the data reported here the highest clearly resolved state, in most cases, was the 8^+. Hence, the excitation functions discussed in the next section are for the 4^+, 6^+, and sum of the 8^+ and 10^+ states only.

III. THE EXPERIMENTAL EXCITATION FUNCTIONS

As indicated in the previous sections of this chapter, three Ge(Li) detectors were used to acquire data in each experimental run (Table V-2, p. 71), primarily to improve statistics. The data for each detector was analyzed separately to generate an excitation function. Ideally, since each represented an independent determination, the calculated excitation functions should have been identical except for experimental uncertainties (i.e., overlapping error bars). In most cases the agreement was very good (e.g., Figure V-9) but in several cases there appeared to be some systematic splitting of the three excitation functions (e.g., Figure V-10). This splitting is not fully understood but was most likely caused by (a) not including dead-time corrections for the coincidence Ge(Li) spectra and/or (b) systematic errors in obtaining the Ge(Li) efficiency calibrations. A single characteristic excitation function for each run was determined by (a) taking a weighted average of the probabilities from each detector for each energy bin and (b) then taking a weighted average of adjacent

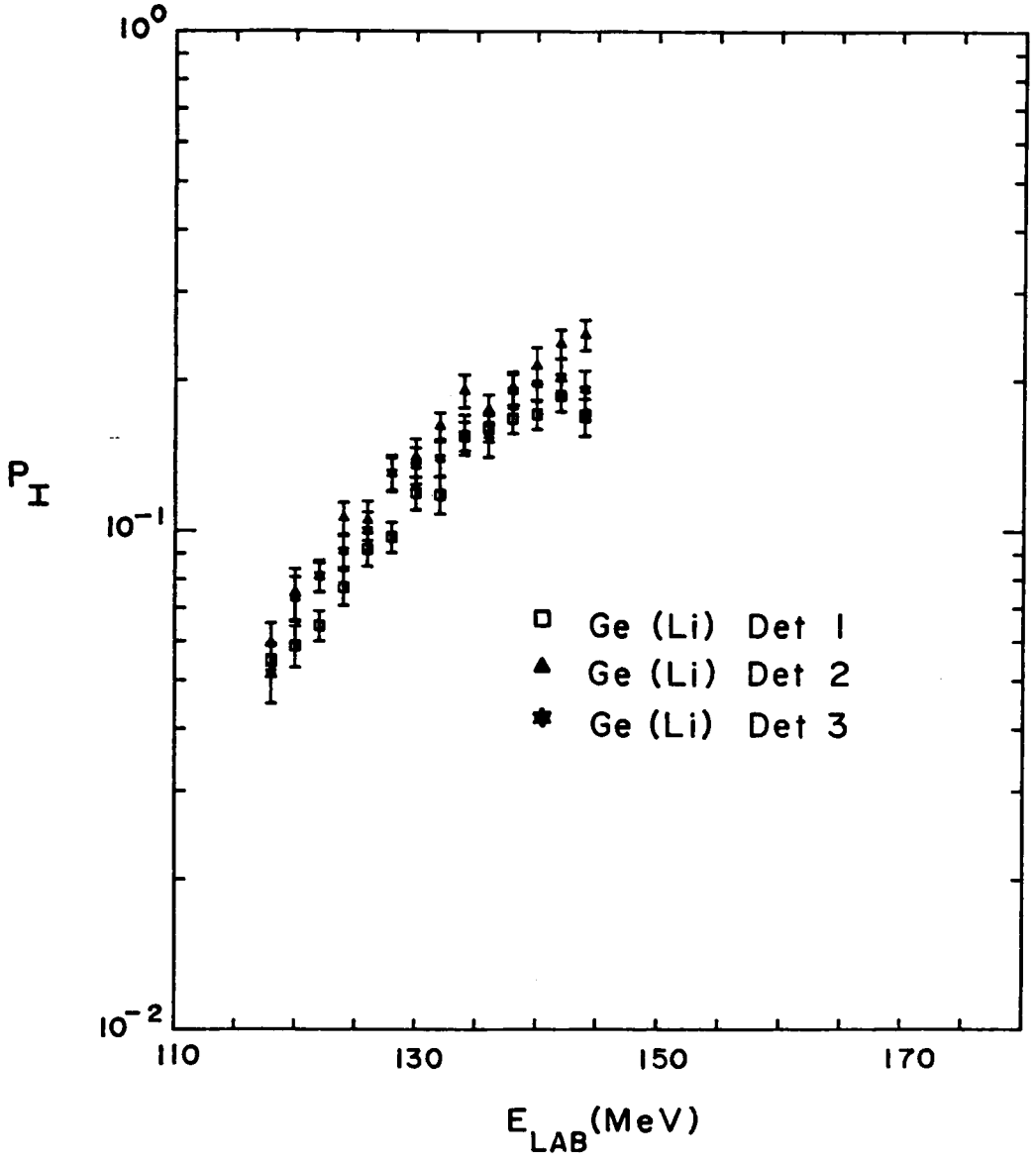


Figure V-9. Example of good agreement between the experimental excitation functions for the three Ge(Li) detectors. This case represents the data for the $8^+ + 10^+$ states obtained in the 145.9-MeV $^{40}Ar + ^{164}Dy$ ORIC II run, prior to averaging and renormalization.

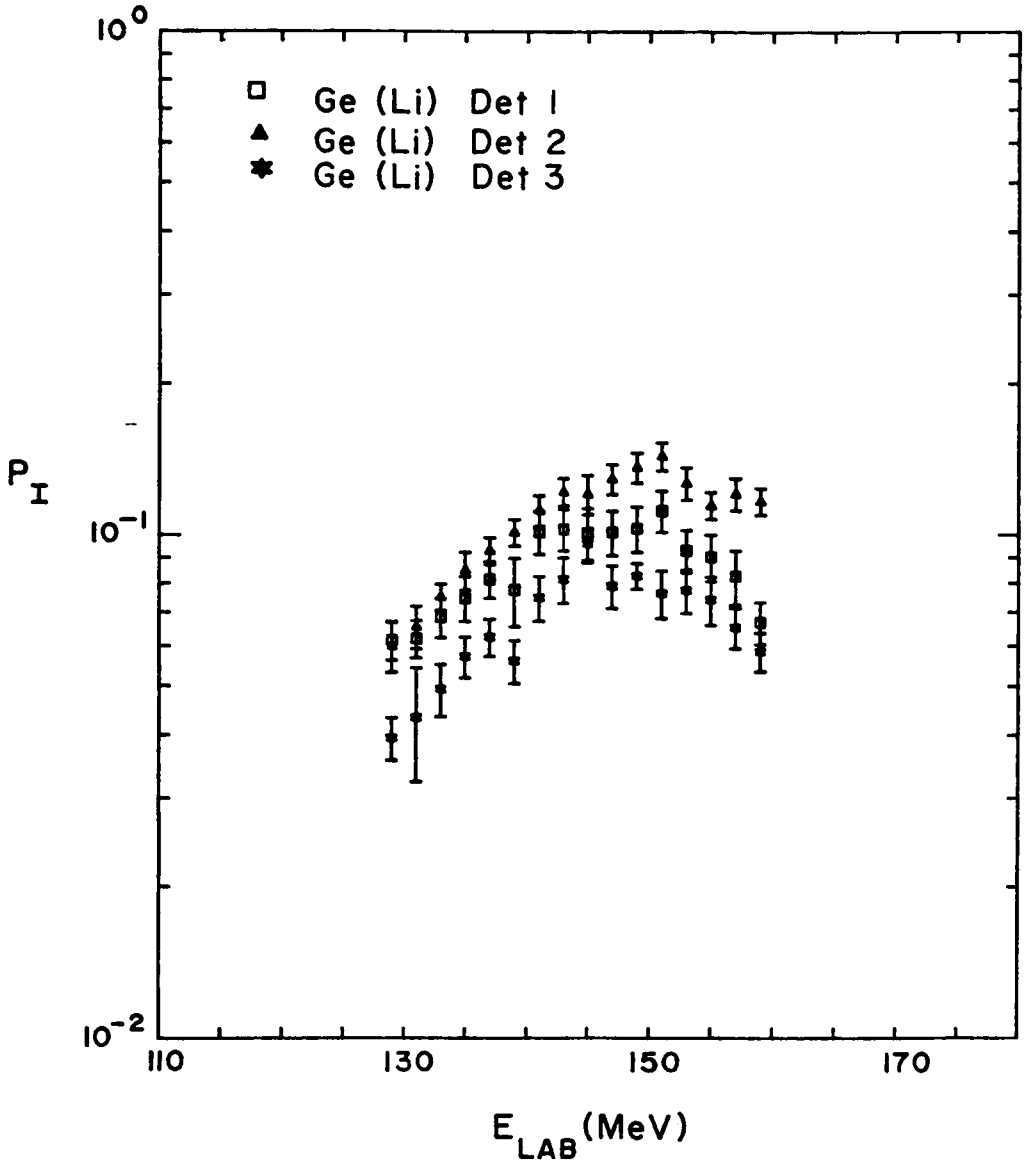


Figure V-10. Example showing the worst case of splitting of the experimental excitation functions for the three Ge(Li) detectors. This case represents the data obtained for the $8^+ + 10^+$ states in the 160.7-MeV $^{40}Ar + ^{162}Dy$ ORIC I run. The average of the three excitation functions is roughly equivalent to that for Ge(Li) detector 1.

bins to produce data points at four-MeV intervals. In those cases where there were only slight differences among the excitation functions from the detectors all three were averaged together. In some cases one detector's excitation function data were omitted from the average if the error bars were appreciably larger than for the data for the other detectors or if there was a large systematic difference from the other experimental excitation functions. In the cases where one detector's data were omitted from the average the resulting excitation functions were not significantly different from those due to averaging the data from all three detectors.

In addition to the above problem, an overall normalization problem was discovered for the excitation functions calculated for the ORIC I and LBL I experiments and for the 145.9-MeV ^{156}Gd run in the ORIC II experiment. The normalization problem in the ORIC II experiment was due to the loss of part of the particle singles data because of a computer failure. The reason for the problems in the ORIC I and LBL I data is unknown, although the most likely cause was not accounting for differences in dead-time losses between the particle singles and the coincidence Ge(Li) spectra. In both experiments the singles and coincidence data had to be stored in separate ADC-analyzer systems. In the experiment with no normalization problems a single multiplexed ADC system was used for both singles and coincidence signals. For the low energy (Coulomb excitation) data, the experimental excitation functions had to be multiplied by factors greater than one to obtain agreement with excitation curves calculated with published electric quadrupole and hexadecapole moments. Similar adjustments were necessary

for the higher energy (CNI) data to obtain agreement between different runs in the regions where the data overlapped. The factors by which the data were renormalized are listed in Table V-5.

In the final analysis (see Chapter VI), the data will be used to measure the deviation of the total real potential from that responsible for Coulomb excitation. Therefore, to insure the best possible fits to the reference Coulomb excitation curve, for some of the cases in Table V-5 separate normalization factors were determined for the experimental excitation functions corresponding to different states within the same run. These normalizations may be attributed to (a) systematic errors in the assumed angular distribution functions, the calculated conversion coefficients, and the measured Ge(Li) detector efficiencies; (b) gating and timing problems in the coincidence electronics which may have had nonuniform effects on the counting statistics for the different states; and/or (c) systematic errors in the determination of the reference Coulomb excitation curves due to inaccurate modeling of the structure of the target nucleus. Except for the 160.7 MeV ^{40}Ar + ^{162}Dy ORIC I run and the 145.9 MeV ^{40}Ar + ^{156}Gd ORIC II run, the differences in the normalization factors were $\lesssim$ 10% (comparable to the net uncertainty in the excitation probabilities from other factors). In the former case, for each state, the shape of the excitation function in the Coulomb excitation region agreed very well with the shape of the corresponding excitation function determined in the 145.9 MeV ^{40}Ar + ^{162}Dy ORIC II run, for which no normalization factor was necessary. In the latter case, where the differences in the factors were the greatest, the statistics were poor and the error bars large so that the average

TABLE V-5

RENORMALIZATION FACTORS FOR THE EXCITATION FUNCTIONS DETERMINED FOR EACH EXPERIMENTAL RUN

Experiment	Target	Beam Energy (MeV)	Factor for 4^+ State	Factor for 6^+ State	Factor for $8^+ + 10^+$ State
ORIC I	^{156}Gd	160.7	3.45	3.35	3.40
	^{160}Gd	122.0	2.50	2.50	2.50
	^{160}Gd	160.7	2.50	2.50	2.50
	^{162}Dy	160.7	1.60	1.80	1.40
	^{164}Dy	160.7	2.70	3.00	2.90
ORIC II	^{156}Gd	145.9	1.60	1.85	2.10
	^{156}Gd	157.2	1.00	1.00	1.00
	^{156}Gd	158.7	1.00	1.00	1.00
	^{162}Dy	145.9	1.00	1.00	1.00
	^{164}Dy	145.9	1.00	1.00	1.00
LBL I	^{160}Gd	174.3	1.09	1.02	1.11
	^{162}Dy	174.3	1.40	1.45	1.35
	^{180}Hf	174.3	1.12	1.12	1.12

Note: The discussion in Section I of Chapter VI explains how the renormalization factors for the ^{180}Hf data were determined.

excitation function was dominated by the other $^{40}Ar + ^{156}Gd$ runs which had superior statistics. In fact, the data from this run could have been ignored with little effect on the final experimental excitation function for $^{40}Ar + ^{156}Gd$.

The averaged and renormalized excitation functions for all runs corresponding to a specific system (see Table V-1, p. 68) were then consolidated into a single excitation function by weighted averaging of probabilities in overlap regions. Tables V-6 through V-10 contain the final experimental excitation functions for the ^{156}Gd, ^{160}Gd, ^{162}Dy, ^{164}Dy, and ^{180}Hf cases, respectively. The energy uncertainties were estimated from straggling widths calculated with the formulae in Appendix C. The uncertainties in the probabilities are statistical in nature and perhaps do not account properly for systematic errors introduced by renormalization of individual data sets, although they are certainly representative of what can be expected in thick-target experiments. These excitation functions appear to be adequate to exemplify the method of extracting surface ion-ion potentials discussed in Chapter VI.

TABLE V-6

EXPERIMENTAL EXCITATION PROBABILITIES FOR THE $^{40}Ar + ^{156}Gd$ SYSTEM

E	ΔE	P_{4^+}	ΔP_{4^+}	P_{6^+}	ΔP_{6^+}	$P_{\Sigma 8^+-10^+}$	$\Delta P_{\Sigma 8^+-10^+}$
119	2.0	0.373	0.017	0.190	0.010	0.037	0.004
123	1.75	0.373	0.021	0.219	0.014	0.053	0.006
127	1.50	0.389	0.021	0.237	0.012	0.053	0.005
130.75	1.25	0.331	0.012	0.271	0.007	0.084	0.003
134.75	1.0	0.311	0.012	0.290	0.007	0.109	0.003
138.75	1.0	0.295	0.012	0.298	0.008	0.124	0.003
142.75	1.0	0.266	0.013	0.311	0.009	0.134	0.004
146.67	1.0	0.256	0.015	0.283	0.009	0.139	0.004
150.67	1.0	0.226	0.012	0.250	0.008	0.118	0.004
154.67	1.0	0.188	0.011	0.187	0.007	0.097	0.003
158	1.0	0.148	0.021	0.112	0.011	0.072	0.005

Note: The effective incident energy E and corresponding uncertainty ΔE are quoted in MeV. The probability for excitation of a particular spin state is denoted by P_I with corresponding uncertainty ΔP_I.

TABLE V-7

EXPERIMENTAL EXCITATION PROBABILITIES FOR THE $^{40}Ar + ^{160}Gd$ SYSTEM

E	ΔE	P_4^+	ΔP_4^+	P_6^+	ΔP_6^+	$P_{\Sigma 8^+ - 10^+}$	$\Delta P_{\Sigma 8^+ - 10^+}$
101	2.0	0.324	0.013	0.090	0.004	0.007	0.002
105	1.75	0.358	0.016	0.112	0.006	0.016	0.001
109	1.5	0.367	0.017	0.156	0.007	0.024	0.002
113	1.25	0.398	0.020	0.179	0.007	0.034	0.003
117	1.0	0.386	0.022	0.223	0.010	0.041	0.003
120	1.0	0.337	0.033	0.233	0.016	0.056	0.006
130	2.0	0.300	0.026	0.291	0.014	0.110	0.007
134	1.75	0.251	0.028	0.344	0.018	0.141	0.010
138	1.5	0.246	0.030	0.381	0.017	0.177	0.010
142.5	1.5	0.200	0.020	0.319	0.012	0.207	0.006
146.5	1.0	0.168	0.020	0.303	0.011	0.210	0.007
150.5	1.0	0.193	0.018	0.255	0.011	0.196	0.006
154.5	1.0	0.160	0.015	0.220	0.009	0.144	0.004
158.5	1.0	0.124	0.011	0.159	0.007	0.107	0.004
163	1.0	0.078	0.010	0.078	0.006	0.071	0.004
167	1.0	0.037	0.005	0.031	0.004	0.032	0.002
170	1.0	0.021	0.004	0.014	0.003	0.021	0.004

Note: Parameters are defined in Table V-6.

TABLE V-8

EXPERIMENTAL EXCITATION PROBABILITIES FOR THE $^{40}Ar + ^{162}Dy$ SYSTEM

E	ΔE	P_4^+	ΔP_4^+	P_6^+	ΔP_6^+	$P_{\Sigma 8^+ - 10^+}$	$\Delta P_{\Sigma 8^+ - 10^+}$
119	2.0	0.363	0.015	0.212	0.007	0.040	0.002
123	1.75	0.351	0.016	0.251	0.008	0.062	0.003
127	1.50	0.345	0.016	0.267	0.009	0.073	0.003
130.5	1.50	0.311	0.014	0.314	0.008	0.087	0.003
134.5	1.25	0.281	0.014	0.298	0.009	0.110	0.003
138.5	1.25	0.237	0.014	0.330	0.010	0.133	0.003
142.67	1.25	0.220	0.012	0.299	0.008	0.151	0.003
146.5	1.25	0.180	0.016	0.287	0.012	0.164	0.005
150.5	1.25	0.188	0.015	0.248	0.011	0.174	0.005
154.5	1.25	0.179	0.015	0.238	0.010	0.152	0.004
158.5	1.25	0.168	0.013	0.174	0.009	0.135	0.004
163	1.0	0.124	0.014	0.148	0.010	0.097	0.005
167	1.0	0.106	0.011	0.084	0.007	0.058	0.004
171	1.0	0.049	0.006	0.035	0.005	0.031	0.003

Note: Parameters are defined in Table V-6.

TABLE V-9

EXPERIMENTAL EXCITATION PROBABILITIES FOR THE $^{40}Ar + ^{164}Dy$ SYSTEM

E	ΔE	P_4^+	ΔP_4^+	P_6^+	ΔP_6^+	$P_{\Sigma 8^+ - 10^+}$	$\Delta P_{\Sigma 8^+ - 10^+}$
119	2.0	0.361	0.017	0.246	0.007	0.059	0.003
123	1.75	0.338	0.017	0.279	0.008	0.079	0.002
127	1.50	0.320	0.019	0.307	0.009	0.105	0.003
130.5	1.25	0.272	0.014	0.303	0.008	0.125	0.003
134.5	1.25	0.252	0.014	0.325	0.009	0.152	0.004
138.5	1.25	0.218	0.014	0.329	0.010	0.185	0.004
142.5	1.25	0.210	0.015	0.324	0.010	0.205	0.005
146	1.0	0.210	0.022	0.299	0.018	0.236	0.009
150	1.0	0.201	0.021	0.266	0.016	0.223	0.008
154	1.0	0.168	0.018	0.218	0.015	0.187	0.008
158	1.0	0.133	0.016	0.145	0.011	0.120	0.005

Note: Parameters are defined in Table V-6.

TABLE V-10

EXPERIMENTAL EXCITATION PROBABILITIES FOR THE $^{40}Ar + ^{180}HF$ SYSTEM

E	ΔE	P_4^+	ΔP_4^+	P_6^+	ΔP_6^+	$P_{\Sigma 8^+ - 10^+}$	$\Delta P_{\Sigma 8^+ - 10^+}$
137	2.25	0.448	0.018	0.179	0.007	0.0228	0.0022
141	2.0	0.413	0.019	0.202	0.008	0.0311	0.0029
145	1.75	0.407	0.021	0.217	0.008	0.0402	0.0026
149	1.50	0.388	0.021	0.239	0.010	0.0591	0.0037
153	1.25	0.358	0.022	0.269	0.010	0.0685	0.0038
157	1.25	0.337	0.022	0.280	0.012	0.0859	0.0046
161	1.25	0.326	0.024	0.270	0.012	0.106	0.0049
165	1.0	0.292	0.022	0.276	0.011	0.0953	0.0054
169	1.0	0.220	0.018	0.221	0.010	0.0773	0.0045
172	1.0	0.180	0.019	0.146	0.010	0.0594	0.0056

Note: Parameters are defined in Table V-6.

CHAPTER VI

THE ION-ION INTERACTION POTENTIAL IN THE NUCLEAR SURFACE REGION

As noted in Chapter I, CNI is an excellent probe of both nuclear charge and mass parameters in the surface region. Also, as indicated in Chapter III, the CLSM method provides a sensitive, accurate formalism for treating heavy-ion CNI reactions involving deformed target nuclei. Furthermore, the localization effects discussed in Chapter IV can be exploited to deduce less ambiguously the ion-ion interaction potential at the nuclear surface. This chapter describes the technique developed to extract the ion-ion interaction potential. The method is demonstrated with applications to the data reported in Chapter V.

I. NUCLEAR CHARGE PARAMETERS

As justified in Appendix B, the monopole-multipole electric interaction specified in the model Hamiltonian (Eq. III-3) is quite adequate for heavy-ion CNI reactions studied in this work. Information on the intrinsic nuclear charge distribution is contained in the multipole moments $Q_0^{(\lambda)}$ defined in Eq. III-4. To obtain values for the $Q_0^{(\lambda)}$, one could perform a Coulomb excitation experiment for a heavy-ion projectile on a deformed target nucleus at safe energies (see Appendix D). From the population signature (the relative excitation probabilities for the excited rotational states) for the inelastic excitation, the $Q_0^{(\lambda)}$ (typically for λ = 2,4) can be deduced by using the

CLSM formalism with no nuclear potential included in the model Hamiltonian.

The $Q_0^{(\lambda)}$ can be expressed in terms of the commonly reported reduced transition matrix elements $\langle 0^+ \| \mathcal{M}(E\lambda) \| \lambda^+ \rangle$, in the rotational approximation, through the relation

$$\langle 0^+ \| \mathcal{M}(E\lambda) \| \lambda^+ \rangle = \sqrt{\frac{2\lambda + 1}{16\pi}}\, Q_0^{(\lambda)} \quad . \tag{VI-1}$$

Table VI-1 lists the values of $\langle 0^+ \| \mathcal{M}(E2) \| 2^+ \rangle$ and $\langle 0^+ \| \mathcal{M}(E4) \| 4^+ \rangle$ reported by Ronningen et al. (1977) for the nuclei studied in this work. Also included in Table VI-1 are the corresponding values of $Q_0^{(2)}$ and $Q_0^{(4)}$ calculated with Eq. VI-1.

The data for the $^{40}Ar + ^{160}Gd$ system obtained in the ORIC I experiment were the first to be analyzed. During the course of resolving the normalization problems described in Chapter V a fit to the data for $E_{LAB} < 140$ MeV (pure Coulomb excitation region) was made to extract the $Q_0^{(2)}$ and $Q_0^{(4)}$ parameters. The resulting values were found to agree very well with those calculated from the matrix elements reported by Ronningen et al. (1977), as can be seen in Table VI-1 where they have been listed for comparison. Although the values due to Ronningen et al. (1977) could have been used with negligible influence on the final results, the $Q_0^{(2)}$ and $Q_0^{(4)}$ values obtained from the ORIC I data were employed in subsequent analyses of the more complete set of data for the $^{40}Ar + ^{160}Gd$ system.

When the data for the $^{40}Ar + (^{156}Gd, ^{162}Dy, ^{164}Dy)$ systems were analyzed, it was observed that the values of $Q_0^{(2)}$ and $Q_0^{(4)}$ calculated from the matrix elements of Ronningen et al. (1977) did an excellent

TABLE VI-1

EXPERIMENTAL VALUES OF $\langle 0^+ \| \mathcal{M}(E\lambda) \| \lambda^+ \rangle$ AND $Q_0^{(\lambda)}(\lambda = 2,4)$ FOR THE NUCLEI STUDIED

Nucleus	$\langle 0^+ \| \mathcal{M}(E2) \| 2^+ \rangle$ (eb)	$\langle 0^+ \| \mathcal{M}(E4) \| 4^+ \rangle$ (eb^2)	$Q_0^{(2)}$ (eb)	$Q_0^{(4)}$ (eb^2)	Source
^{156}Gd	2.138	0.42	6.779*	0.993*	Ronningen et al. (1977)
^{160}Gd	2.279	0.33	7.226	0.780	Ronningen et al. (1977)
^{160}Gd	2.275	0.35	7.214*	0.825*	This work
^{162}Dy	2.32	0.27	7.356*	0.638*	Ronningen et al. (1977)
^{164}Dy	2.367	0.25	7.505*	0.591*	Ronningen et al. (1977)
^{180}Hf	2.176	0.21	6.899	0.496	Ronningen et al. (1977)
^{180}Hf	2.176	-0.65	6.899	-1.536	Ronningen et al. (1977)
^{180}Hf	1.945	-0.11	6.167*	-0.252*	This work

*The $Q_0^{(2)}$ and $Q_0^{(4)}$ values marked with an asterisk are the ones used in the fitting procedure described in Section IV of this chapter.

Note: For the entries from Ronningen et al. (1977) the $Q_0^{(\lambda)}$ were calculated from the $\langle 0^+ \| \mathcal{M}(E\lambda) \| \lambda^+ \rangle$ using Eq. VI-1, whereas for those marked "This work" the $\langle 0^+ \| \mathcal{M}(E\lambda) \| \lambda^+ \rangle$ were calculated from the $Q_0^{(\lambda)}$.

job of reproducing the population signatures in the pure Coulomb excitation region. Therefore, based on the close agreement for the ^{160}Gd moments, no fits were considered necessary to obtain the $Q_0^{(2)}$ and $Q_0^{(4)}$ values for these systems. Instead, the values due to Ronningen et al. (1977) listed in Table VI-1 were used in the analyses described in Section IV.

Coulomb excitation measurements of the electric moments of ^{180}Hf are rather sparse. In fact, aside from the heavy-ion measurement discussed in this work, the only values currently available are those of Ronningen et al. (1977) from Coulomb excitation by α-particles. Because ^{180}Hf lies in a region where the $\langle 0^+ || \mathcal{M}(E4) || 4^+ \rangle$ values are predicted to change sign (Flocard, Quentin, and Vautherin, 1973; Nerlo-Pomorska, 1976), Ronningen et al. (1977) were unable to unambiguously determine the sign of the $\langle 0^+ || \mathcal{M}(E4) || 4^+ \rangle$ moment. Table VI-1 lists both their positive and negative candidates for the $\langle 0^+ || \mathcal{M}(E4) || 4^+ \rangle$ matrix element for ^{180}Hf, as well as their experimental measurement of $\langle 0^+ || \mathcal{M}(E2) || 2^+ \rangle$. CLSM calculations of the population signature for ^{180}Hf in the Coulomb excitation region were made using $Q_0^{(2)}$ and $Q_0^{(4)}$ moments corresponding to these matrix elements (Table VI-1). Neither choice gave acceptable agreement with the experimental population signature.

Let the probability ratios R_{31} and R_{32} be defined by

$$R_{31} = \frac{P_{\Sigma 8^+} - 10^+}{P_{4^+}} \qquad \text{(VI-2)}$$

and

$$R_{32} = \frac{P_{\Sigma 8^+} - 10^+}{P_{6^+}} . \qquad \text{(VI-3)}$$

In Eqs. VI-2 and VI-3, the P_I are excitation probabilities for the state I. R_{31} and R_{32} represent experimental population signature ratios for the ^{180}Hf data. Because of the way that they are defined, they are insensitive to an overall renormalization of the probabilities. A FORTRAN computer code was written to perform a nonlinear least-squares fit to the experimental R_{31} and R_{32} values with $Q_0^{(2)}$ and $Q_0^{(4)}$ as adjustable parameters. The multipole moments obtained from this fit are listed in Table VI-1 for comparison to the values of Ronningen et al. (1977). Note that there are significant differences for both the $Q_0^{(2)}$ and $Q_0^{(4)}$ moments. Figure VI-1 presents a comparison of R_{31} and R_{32} as functions of energy calculated with the moments of Ronningen et al. (1977) to the least-squares results for the experimental probability ratios. Clearly, the $Q_0^{(2)}$ and $Q_0^{(4)}$ moments measured by Ronningen et al. (1977) using α-particle projectiles are incompatible with the moments extracted from the ^{40}Ar heavy-ion Coulomb excitation.

The reasons for the discrepancy between these two measurements of the electric moments of ^{180}Hf are unknown. The analysis of the data for the ^{40}Ar + ^{180}Hf system exactly paralleled the procedure outlined in Chapter V used for the other systems, which gave excellent agreement with previous measurements of the electric moments. Moreover, the overall normalization problem noted in Chapter V can be ignored, because relative probabilities are sufficient to determine $Q_0^{(2)}$ and $Q_0^{(4)}$ in the Coulomb excitation region. A possible explanation of the ambiguity could

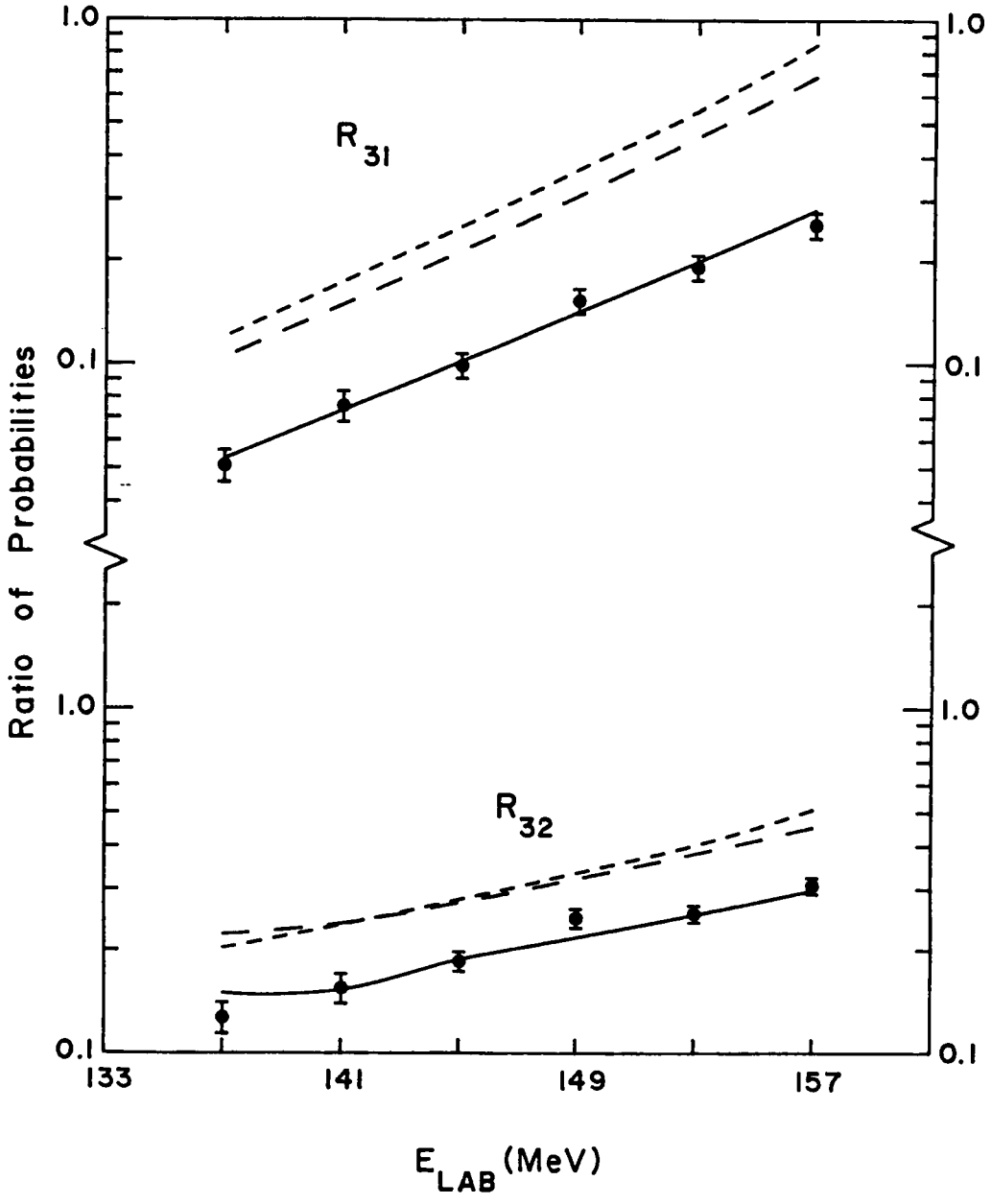


Figure VI-1. Least-squares fit to the experimental population signature of ^{180}Hf in the Coulomb excitation region. $Q_0^{(2)}$ and $Q_0^{(4)}$ were varied to achieve the fits (solid curves) to R_{31} and R_{32} (defined in Eqs. VI-2 and VI-3). The short (long) dashed curves are calculations using the positive (negative) $Q_0^{(4)}$ moment from Ronningen et al. (1977) [see Table VI-1].

be some systematic error in the analysis by Ronningen et al. (1977). The same possibility exists for the analysis described here. However, there is some evidence which suggests that ^{180}Hf may exhibit a triaxial structure (Lee, 1981). Thus, the assumption of axial symmetry may be at fault in both approaches. Also, if the intrinsic structure of ^{180}Hf changes as it is excited up the ground-state rotational band, the two approaches may measure different average $Q_0^{(2)}$ and $Q_0^{(4)}$ moments because each approach samples a different number of spin states. In any case, to be consistent, in the analysis reported in Section IV the $Q_0^{(2)}$ and $Q_0^{(4)}$ values determined by the ^{40}Ar + ^{180}Hf experiment were used.

II. PARAMETRIZATION OF THE NUCLEAR POTENTIAL

The radial and angular localization effects discussed in Chapter IV imply that the problem of determining a global ion-ion potential in the coordinates (r,χ) may be reduced to the simpler and more transparent problem of constructing the potential piece by piece in separate localized regions of the nuclear surface. They also imply that the contours of the ion-ion potential may be extracted from experimental data without having to use particular forms for the potentials (e.g., folding, Woods-Saxon, proximity, etc.) in the scattering calculation itself. Once the potential contours have been constructed, the various proposed theoretical forms may be compared directly to the experimental potential. This independence from particular parametrizations of the potential in the scattering calculation is quite similar in spirit to "model-independent" analyses of electron scattering data and muonic atoms (Barrett and Jackson, 1977).

From the above discussion, it is evident that the form of the real nuclear potential used in the calculation is not critical, since it will only be required to describe a localized region of the nuclear surface sampled by a particular spin state. It only need have enough parameters to do this accurately. The parameters themselves need not be directly connected to physically significant quantities, since they are only tools used to construct a portion of the potential. Particular physical significance will be attached only to the global potential constructed in this manner. In the most general case the potential could be expanded around the point(s) (r,χ) making the dominant contribution to a particular state for a particular energy; the expansion coefficients varied to yield the best fit to the data; and the potential in that region determined from the values of the expansion coefficients.

For the cases discussed in this dissertation a simpler approach was taken. A Woods-Saxon potential (Eq. II-12) is known to give a reasonably good description for spherical nuclei. Therefore, a deformed Woods-Saxon potential (Eq. II-13) should provide an adequate approximation to the deformed nuclear potential over a limited surface region. Therefore, the explicit expressions for the functions f_R and f_I used in the model Hamiltonian (Eq. III-3) were

$$f_R(r,\chi) = \left[1 + \exp\left(\frac{r-R_R(\chi)}{a_R}\right)\right]^{-1} \qquad \text{(VI-4)}$$

and

$$f_I(r,\chi) = \left[1 + \exp\left(\frac{r-R_I(\chi)}{a_I}\right)\right]^{-1}, \qquad \text{(VI-5)}$$

where

$$R_i(\chi) = R_0^i[A_P^{1/3} + A_T^{1/3}(1 + \bar{\beta}_2 Y_{20}(\chi) + \bar{\beta}_4 Y_{40}(\chi) - \frac{\bar{\beta}_2^2 + \bar{\beta}_4^2}{4\pi})] \quad . \qquad \text{(VI-6)}$$

In Eqs. VI-4 and VI-5, a_R and a_I denote real and imaginary diffuseness parameters, respectively. In Eq. VI-6, R_0^R and R_0^I are real and imaginary optical radius parameters, respectively, A_P and A_T are the projectile and target atomic mass numbers, $Y_{\lambda 0}(\chi)$ is a spherical harmonic, and $\bar{\beta}_2$ and $\bar{\beta}_4$ are parameters used to deform the potential. The term involving the squares of the deformation parameters was included to insure volume conservation, although its effect is relatively small for typical values of the deformation parameters used in the calculations. Note that the parameters $\bar{\beta}_2$ and $\bar{\beta}_4$ are <u>not</u> the standard nuclear deformation parameters β_2 and β_4 normally quoted in the literature. They are only parameters which aid in describing the shape of the ion-ion potential over a limited angular and radial region. Although a more general form could be used, this parametrization seems adequate for fitting the data reported in Chapter V.

III. EQUATIONS OF MOTION

All of the terms in the model Hamiltonian (Eq. III-3) have been defined explicitly. Therefore, by straightforward application of Hamilton's equations, one can determine the classical equations of motion for this problem. Because the effect of the imaginary potential is treated separately and approximately (as discussed later in this section), only the equations pertaining to the real part of the Hamiltonian are listed here. These are:

$$\dot{r} = \frac{p_r}{m} \; ; \tag{VI-7}$$

$$\dot{p}_r = \frac{p_\chi^2}{mr^3} + \frac{Z_P Z_T e^2}{r^2} + \frac{3}{2}\frac{Z_P Q_0^{(2)} e^2}{r^4} P_2(\cos\chi)$$

$$+ \frac{5}{2}\frac{Z_P Q_0^{(4)} e^2}{r^6} P_4(\cos\chi) - \frac{4k_1}{r^5}\{1 + k_2(1 +$$

$$2\beta_2 Y_{20}(\chi))\} - \frac{6k_4}{r^7} - \frac{V_0}{a_R} f_R(r,\chi)[1 - f_R(r,\chi)] \; ; \tag{VI-8}$$

$$\dot{\chi} = \left(\frac{1}{\mathcal{I}} + \frac{1}{mr^2}\right)p_\chi \; ; \tag{VI-9}$$

$$\dot{p}_\chi = \frac{3Z_P Q_0^{(2)} e^2}{4r^3}\sin(2\chi) + \frac{5Z_P Q_0^{(4)} e^2}{32r^5}[7\sin(4\chi)$$

$$+ 2\sin(2\chi)] - 3\sqrt{\frac{5}{4\pi}}\frac{k_1 k_2 \beta_2}{r^4}\sin(2\chi)$$

$$- \frac{V_0}{a_R} f_R(r,\chi)[1 - f_R(r,\chi)]\{r_0^R A_T^{1/3}[\frac{3\sqrt{5}}{2}\beta_2\sin(2\chi)$$

$$+ \frac{15}{16}\beta_4(7\sin(4\chi) + 2\sin(2\chi))]\} \; . \tag{VI-10}$$

All quantities appearing in Eqs. VI-7 through VI-10 are as defined in Chapter III, Section II of this chapter, and Appendix A. The dot appearing above the dynamical quantities signifies differentiation with respect to the time t. The above set of coupled equations is augmented by the equation for the classical action (Eq. III-8).

The effect of the imaginary potential is treated approximately in the version of the CLSM method selected to treat this problem. In general, an imaginary potential gives rise to absorption, diffraction, and reflection effects. However, to first order in $\frac{W}{V}$, the imaginary potential only gives rise to an absorption factor (Broglia et al., 1974)

$$A = \exp[-\frac{1}{\hbar}\int W\, dt] \ , \qquad \text{(VI-11)}$$

where the integral is evaluated along a trajectory governed by the real potential. In that case, a relatively clean separation between the effects of the real potential (refractive and diffractive) and the imaginary potential (absorption) is possible. Because the effect of the imaginary potential was found to be relatively small, except for the highest energies, for the data discussed here, the approximation represented by Eq. VI-11 was adopted. Therefore, Eq. VI-11 represents an auxiliary equation similar to Eq. III-8 which was included in the integration of the equations of motion.

To determine the quantities needed to calculate the CLSM probabilities (see Chapter III), the aforementioned equations must be integrated numerically subject to the initial conditions

$$r = \text{large (beyond region of inelastic excitation)} \ ; \qquad \text{(VI-12)}$$

$$p_r = -\sqrt{2m(E_{CM} - \frac{Z_p Z_T e^2}{r})} \ ; \qquad \text{(VI-13)}$$

$$\chi = \chi_0 \ \text{(arbitrary in range 0 to } \pi/2) \ ; \qquad \text{(VI-14)}$$

$$p_\chi = 0 \; ; \tag{VI-15}$$

$$\Phi = 0 \; . \tag{VI-16}$$

In Eq. VI-13, E_{CM} is the center-of-mass energy for the system in the asymptotic region. Typically, the initial radius for the integration was chosen to be

$$r = 60 \; a \; , \tag{VI-17}$$

where a is half of the distance of closest approach in a head-on collision for a monopole-monopole Coulomb potential and is defined by

$$a = \frac{Z_P Z_T e^2}{m v_0^2} = \frac{Z_P Z_T e^2}{2 \; E_{CM}} \; . \tag{VI-18}$$

In Eq. VI-18, m is the reduced mass of the system and v_0 is the initial relative velocity in the asymptotic region. The actual integration of the four coupled equations of motion and the two auxiliary equations was accomplished with a FORTRAN version of a Zonneveld-Adams-Moulton routine for coupled first-order differential equations. To use this routine the input equations first had to be reduced to dimensionless form. For completeness, those dimensionless equations are included in Appendix E. Also included in Appendix E is a brief discussion of a few important technical points concerning the operation of the CLSM code KULEXA, as modified for the purpose of this dissertation.

IV. FITS TO THE EXPERIMENTAL EXCITATION FUNCTIONS

The nuclear potential defined by the last two terms of Eq. III-3 and Eqs. VI-4 through VI-6 has several adjustable parameters: V_0, W_0, R_0^R, R_0^I, a_R, a_I, $\bar{\beta}_2$, and $\bar{\beta}_4$. In principle, all could be varied. Furthermore, the assumption of equivalent deformations for the real and imaginary potentials, implicit in the definition of $R_R(x)$ and $R_I(x)$ [Eq. VI-6], could be relaxed to generate two additional parameters. However, a total of ten adjustable parameters would seem unwarranted for the data included in Tables V-6 through V-10 (pp. 94-97).

Because CNI experiments are insensitive to the nuclear interior, the real and imaginary well depths, V_0 and W_0, were fixed in the fitting procedure. Also, because the effect of the imaginary potential is small and treated only approximately (see Eq. VI-11), $\bar{\beta}_2$ and $\bar{\beta}_4$ were chosen to to be the same for both the real and imaginary potentials. Hence, a total of six parameters remained.

In an early analysis of the $^{40}Ar + ^{160}Gd$ data from the ORIC I experiment (Neese et al., 1979) both $\bar{\beta}_2$ and $\bar{\beta}_4$ were allowed to vary. In some initial analyses of the complete set of data for $^{40}Ar + ^{160}Gd$, $\bar{\beta}_2$ was varied and $\bar{\beta}_4$ was fixed. Investigations of the results of the fitting procedure and of the Chi-squared surfaces and covariance matrices indicated that the quality of the data in Tables V-6 through V-10 was insufficient to permit simultaneous determination of R_0^R, a_R, R_0^I, a_I, $\bar{\beta}_2$, and $\bar{\beta}_4$. Also, because the tail of the nuclear ion-ion potential is largely determined by the radius and diffuseness parameters, in the ensuing analyses $\bar{\beta}_2$ and $\bar{\beta}_4$ were fixed at values reported for the corresponding nuclear deformation parameters β_2 and β_4 from previous

Coulomb excitation measurements (Erb et al., 1972; Wollersheim and Elze, 1977) or from theoretical predictions (Gareev, Ivanova, and Pashkevich, 1970). As noted in Section II of this chapter, $\bar{\beta}_2$ and $\bar{\beta}_4$ need not have any direct relationship to the standard nuclear deformation parameters. As long as they are given reasonable values there will not be much difference in the final potential contours.

Hence, in the fits to the experimental excitation functions only R_0^R, a_R, R_0^I, and a_I were allowed to vary. The fitting was accomplished with a FORTRAN nonlinear least-squares routine based on the method of Powell (1965) which called KULEXA to calculate the Chi-squared function for the experimental excitation probabilities. Although some ambiguities in the potentials determined for the individual states were noted, these could be attributed to valleys and local minima in the five-dimensional Chi-squared surface caused by the oscillatory nature of the excitation functions. The ambiguities were resolved with the requirement that in the region where contours from two different states overlap they should lie within experimental uncertainty of each other. (Such overlap occurs due to finite rotation of the target nucleus during the interaction.) This continuity argument was employed to reject spurious fits to the individual states. In all cases, only one consistent set of potentials could be found. Best fits for each system are shown in Figures VI-2 through VI-6 and the associated parameters are listed in Tables VI-2 through VI-6. In all cases it is clear that the effect of the imaginary potential is small except at the highest energies. Part of the reason for the small value for W is the fact that Coulomb excitation and inelastic channels are treated explicitly. Thus, the part of the imaginary potential

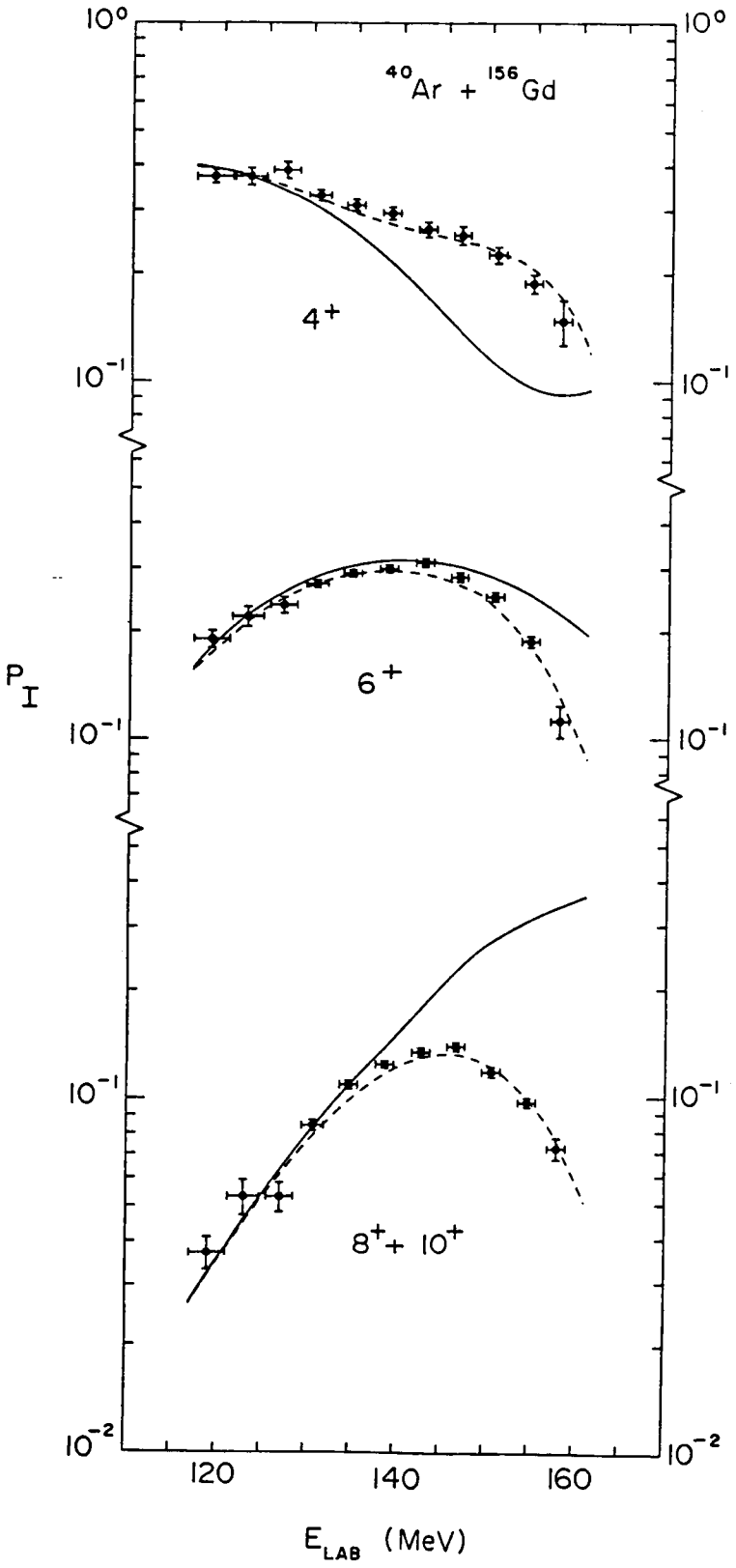


Figure VI-2. Fits to the experimental excitation functions for the $^{40}Ar + ^{156}Gd$ system. The dashed curves were calculated using the parameter set in Table VI-2. The solid curves were calculated assuming pure Coulomb excitation.

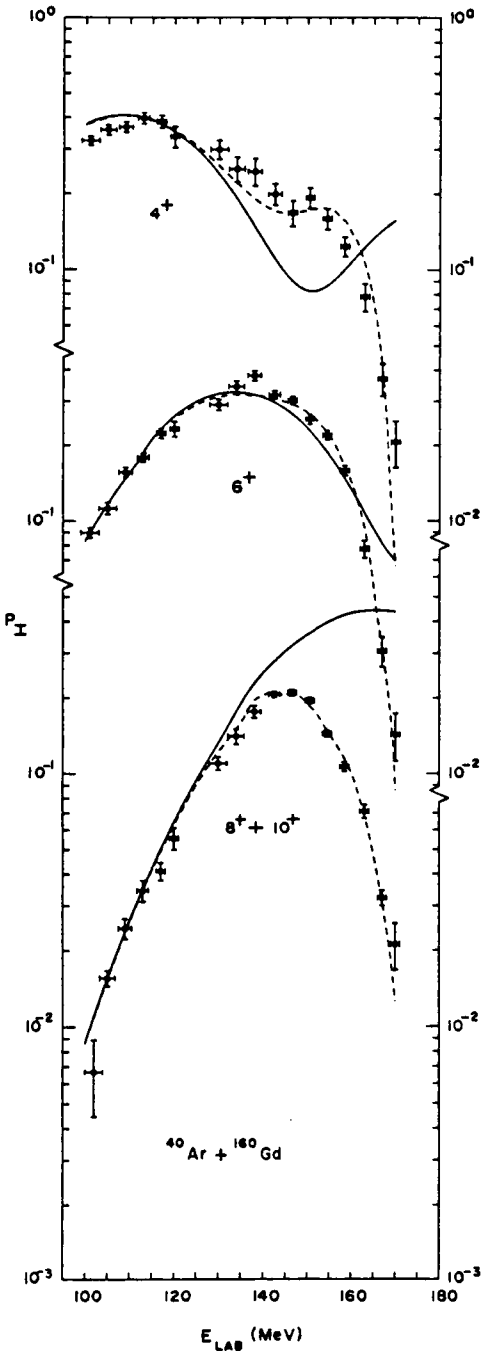


Figure VI-3. Same as Figure VI-2, except for the $^{40}Ar + ^{160}Gd$ system. The parameter set in Table VI-3 was used for the dashed curves.

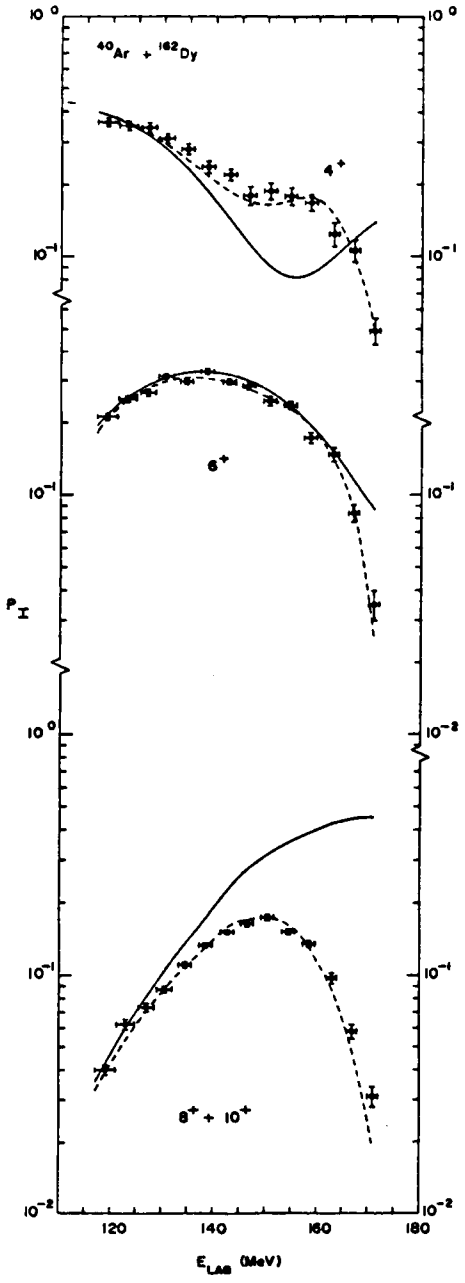


Figure VI-4. Same as Figure VI-2, except for the $^{40}Ar + ^{162}Dy$ system. The parameter set in Table VI-4 was used for the dashed curves.

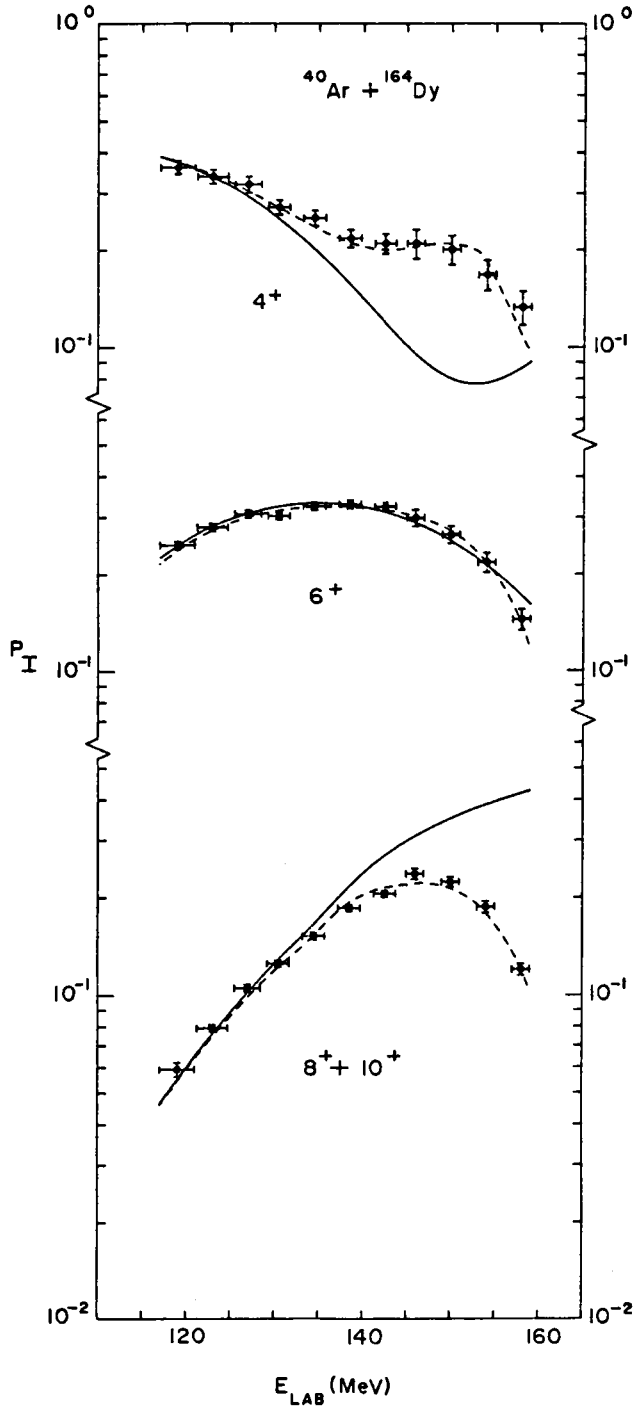


Figure VI-5. Same as Figure VI-2, except for the $^{40}Ar + ^{164}Dy$ system. The parameter set in Table VI-5 was used for the dashed curves.

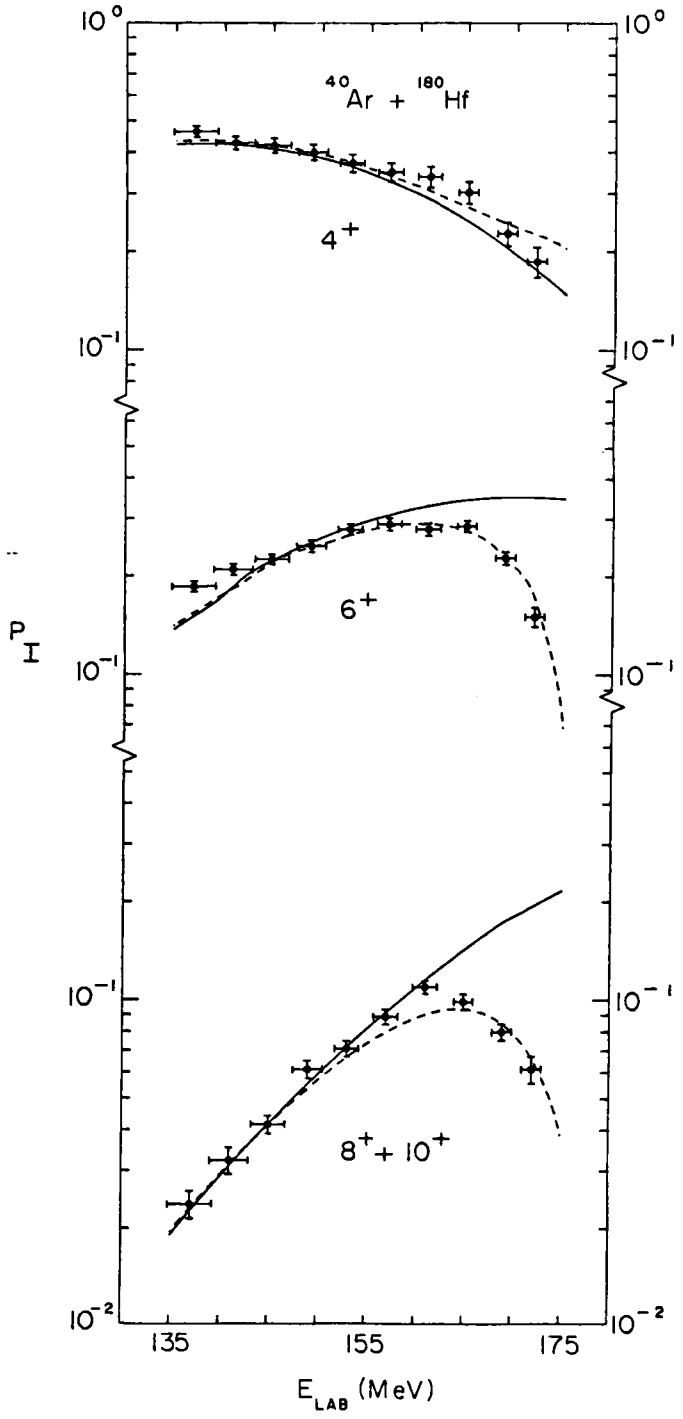


Figure VI-6. Same as Figure VI-2, except for the $^{40}Ar + ^{180}Hf$ system. The parameter set in Table VI-6 was used for the dashed curves.

TABLE VI-2

BEST-FIT PARAMETERS FOR THE $^{40}Ar + ^{156}Gd$ ION-ION POTENTIAL

Parameter	4^+ State	6^+ State	$\Sigma 8^+$-10^+ States
V_0 (MeV)	50.	50.	50.
R_0^R (fm)	1.230	1.229	1.200
a_R (fm)	0.750	0.704	0.717
W_0 (MeV)	25.	25.	25.
R_0^I (fm)	1.187	1.150	1.252
a_I (fm)	0.671	0.650	0.536
$\bar{\beta}_2$	0.32	0.32	0.32
$\bar{\beta}_4$	0.060	0.060	0.060

Note: Only R_0^R, a_R, R_0^I, and a_I were varied. The other parameters were fixed.

TABLE VI-3

BEST-FIT PARAMETERS FOR THE ^{40}Ar + ^{160}Gd ION-ION POTENTIAL

Parameter	4^+ State	6^+ State	$\Sigma 8^+$-10^+ States
V_0 (MeV)	50.	50.	50.
R_0^R (fm)	1.180	1.180	1.160
a_R (fm)	0.825	0.796	0.864
W_0 (MeV)	25.	25.	25.
R_0^I (fm)	1.150	1.065	0.833
a_I (fm)	0.719	0.771	0.798
$\overline{\beta}_2$	0.34	0.34	0.34
$\overline{\beta}_4$	0.032	0.032	0.032

Note: Only R_0^R, a_R, R_0^I, and a_I were varied. The other parameters were fixed.

TABLE VI-4

BEST-FIT PARAMETERS FOR THE $^{40}Ar + ^{162}Dy$ ION-ION POTENTIAL

Parameter	4^+ State	6^+ State	$\Sigma\, 8^+$-10^+ States
V_0 (MeV)	50.	50.	50.
R_0^R (fm)	1.180	1.200	1.166
a_R (fm)	0.836	0.663	0.794
W_0 (MeV)	25.	25.	25.
R_0^I (fm)	1.213	1.055	0.234
a_I (fm)	0.602	0.918	2.333
$\bar{\beta}_2$	0.33	0.33	0.33
$\bar{\beta}_4$	0.010	0.010	0.010

Note: Only R_0^R, a_R, R_0^I, and a_I were varied. The other parameters were fixed.

TABLE VI-5

BEST-FIT PARAMETERS FOR THE $^{40}Ar + ^{164}Dy$ ION-ION POTENTIAL

Parameter	4^+ State	6^+ State	$\Sigma\, 8^+$-10^+ States
V_0 (MeV)	50.	50.	50.
R_0^R (fm)	1.234	1.220	1.179
a_R (fm)	0.822	0.786	0.793
W_0 (MeV)	25.	25.	25.
R_0^I (fm)	1.160	1.163	1.121
a_I (fm)	0.800	0.684	0.778
$\overline{\beta}_2$	0.34	0.34	0.34
$\overline{\beta}_4$	0.008	0.008	0.008

Note: Only R_0^R, a_R, R_0^I, and a_I were varied. The other parameters were fixed.

TABLE VI-6

BEST-FIT PARAMETERS FOR THE $^{40}Ar + ^{180}Hf$ ION-ION POTENTIAL

Parameter	4^+ State	6^+ State	$\Sigma\, 8^+$-10^+ States
V_0 (MeV)	50.	50.	50.
R_0^R (fm)	1.150	1.178	1.157
a_R (fm)	0.700	0.718	0.706
W_0 (MeV)	25.	25.	25.
R_0^I (fm)	1.130	1.235	1.166
a_I (fm)	0.650	0.453	0.545
$\bar{\beta}_2$	0.250	0.250	0.250
$\bar{\beta}_4$	-0.040	-0.040	-0.040

Note: Only R_0^R, a_R, R_0^I, and a_I were varied. The other parameters were fixed.

arising from rotational inelastic scattering in optical model calculations with heavy ions (Love, Teresawa, and Satchler, 1977) does not appear here. Also note that in all cases the onset of the interference is as predicted by the simple rule for CNI (see Chapter III).

V. THE GLOBAL ION-ION POTENTIALS

Using the trajectories of the semiclassical calculations to identify the regions of the nuclear surface sampled by each state, the global real potentials were then constructed piece by piece as shown in Figures VI-7 through VI-11. In each case the contributions from each separate state and the composite potential are shown for the 0.1 and 1.0 MeV contours. The rather small scatter about the average contour is taken to represent the uncertainty in contour position and is presumed due to experimental and theoretical uncertainties. [Note that the largest scatter occurs for the $^{40}Ar + ^{162}Dy$ contours (Figure VI-9) and the $^{40}Ar + ^{164}Dy$ contours (Figure VI-10). There may be some correlation of this behavior with the large differences between the normalization factors for the different states in the ORIC I runs (see Table V-5, p. 92) for these systems.] The individual potential contours V are conveniently represented by fitting a spherical harmonic expansion to each individual contour of the form

$$R(V) = R_0(V)\,[A_P^{1/3} + A_T^{1/3}\,(1 + \alpha_2(V)Y_{20}(x) + \alpha_4(V)Y_{40}(x))]\,, \qquad \text{(VI-19)}$$

where $R_0(V)$, $\alpha_2(V)$, and $\alpha_4(V)$ are adjustable parameters. The solid lines in the (d) parts of Figures VI-7 through VI-11 represent such fits.

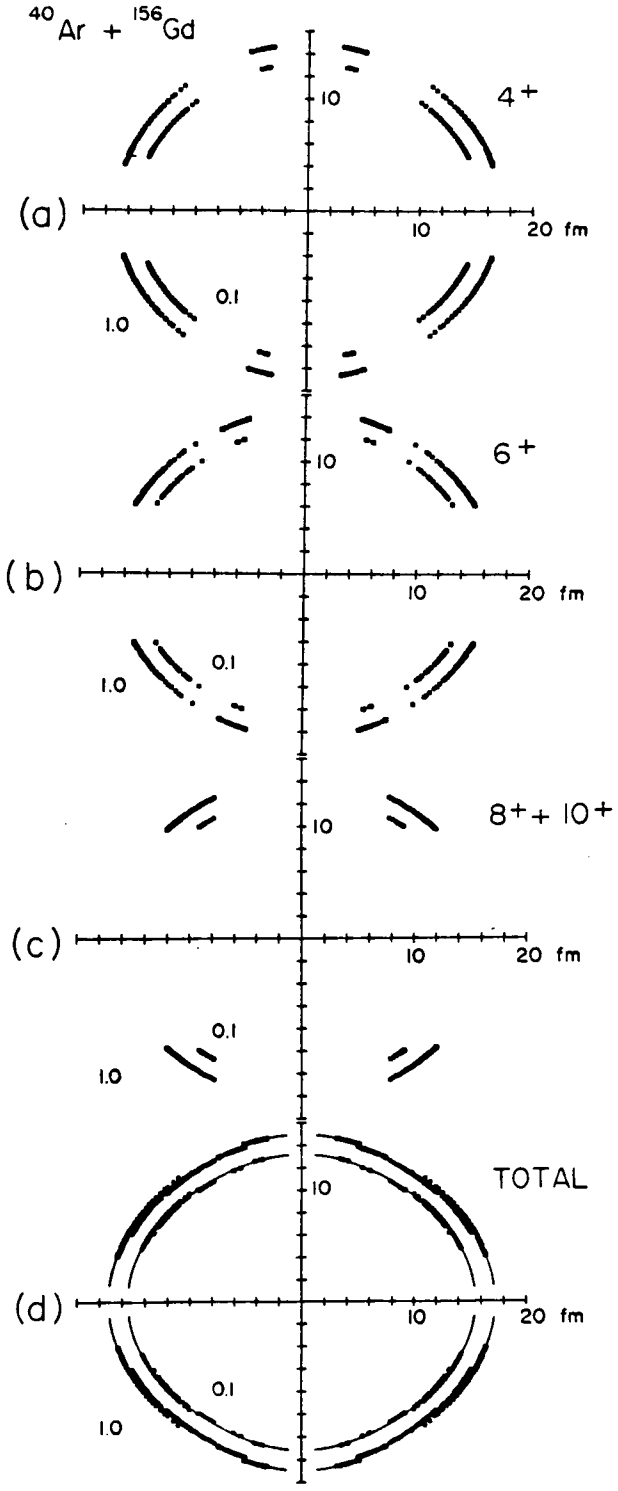


Figure VI-7. The deformed ion-ion potential contours for ^{40}Ar + ^{156}Gd. The contributions from each state for the 0.1 Mev and 1.0 MeV contours are shown in (a)-(c). The composite nuclear potential energy surface for the ion-ion interaction is shown in (d). The solid curves in (d) are spherical harmonic representations of each contour (see Eq. VI-19 and Table VI-7). In (d) the gaps near the axes occur because no information was obtained for the 0^+ and 2^+ states.

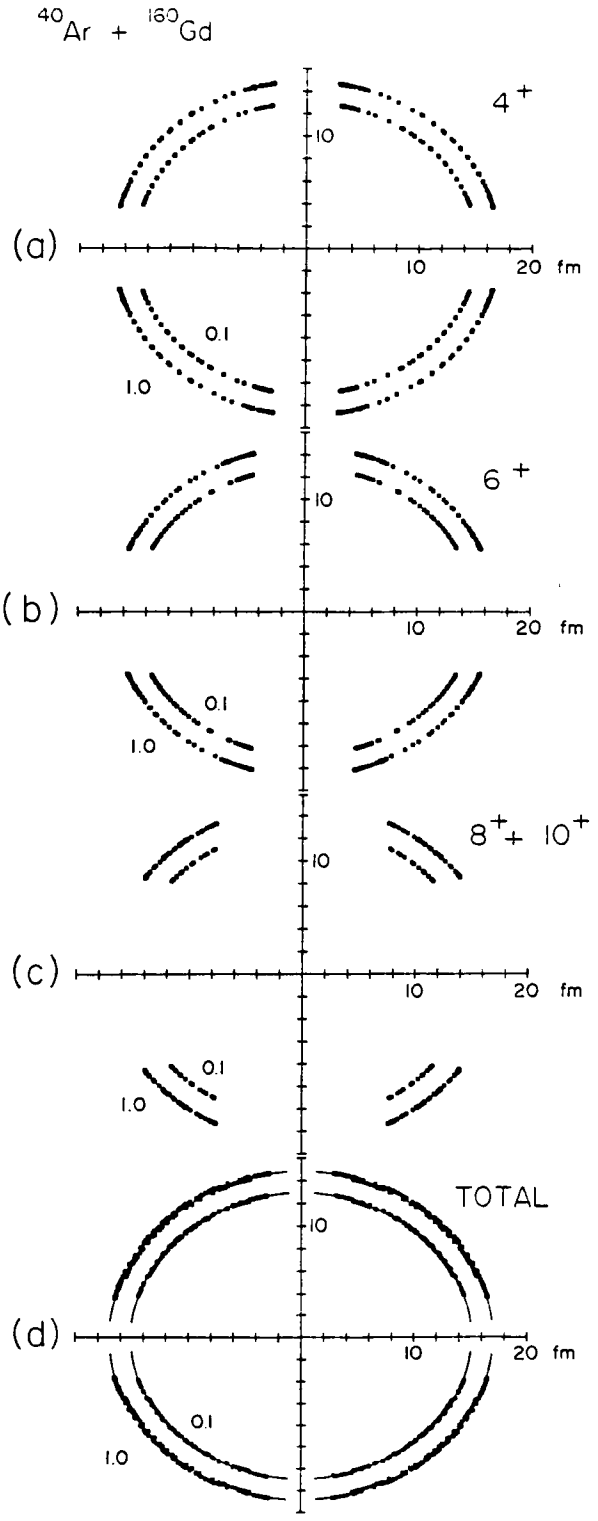


Figure VI-8. Same as Figure VI-7, except for $^{40}Ar + ^{160}Gd$.

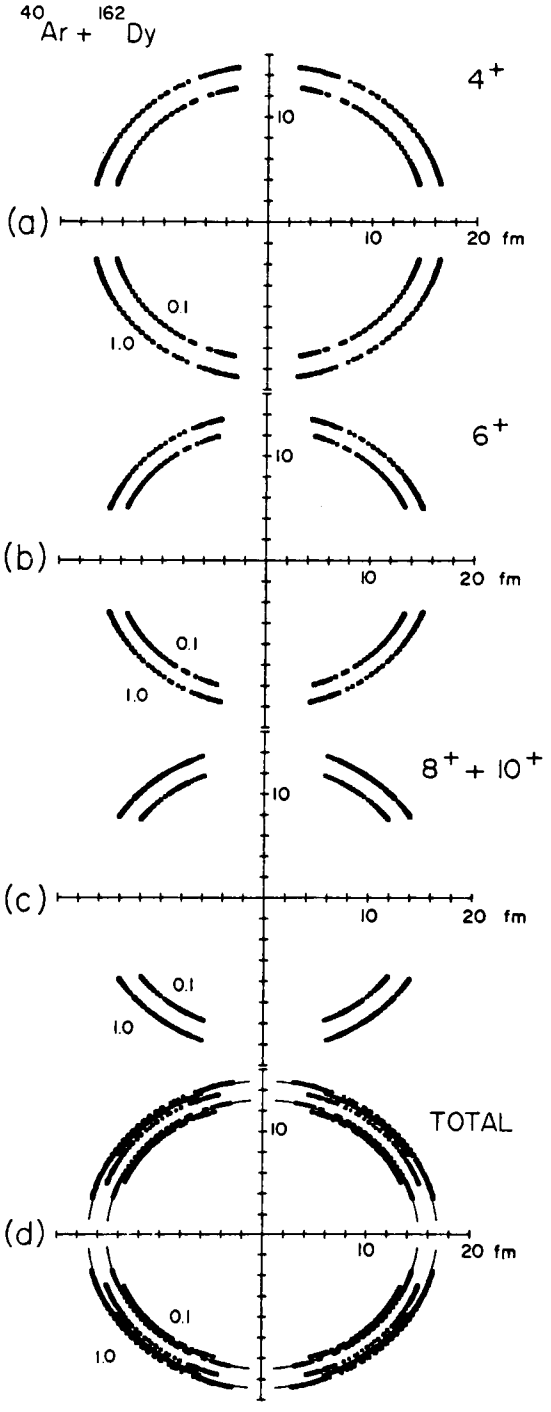


Figure VI-9. Same as Figure VI-7, except for $^{40}Ar + ^{162}Dy$.

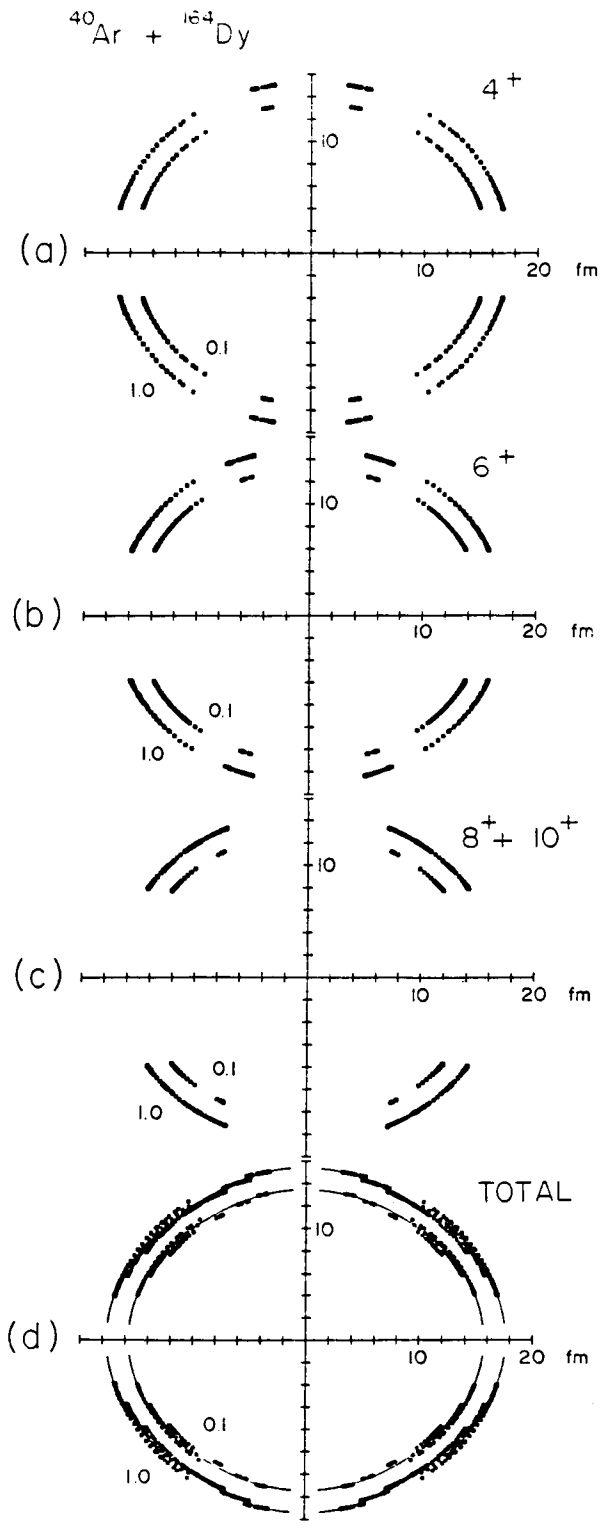


Figure VI-10. Same as Figure VI-7, except for $^{40}Ar + ^{164}Dy$.

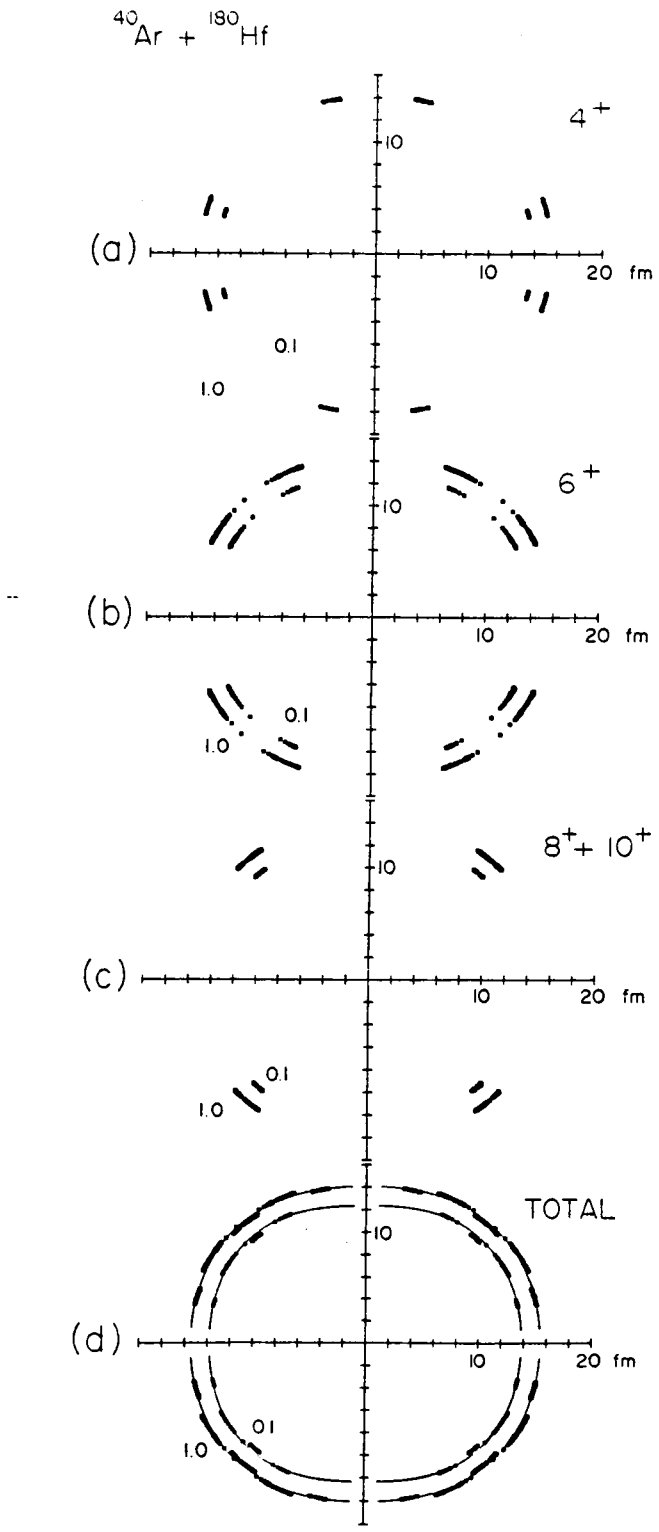


Figure VI-11. Same as Figure VI-7, except for $^{40}Ar + ^{180}Hf$.

Table VI-7 contains the parameters $R_0(V)$, $\alpha_2(V)$, and $\alpha_4(V)$ for the 0.1, 0.5, and 1.0 MeV contours for each system studied.

This approach differs from previous studies of the shape of nuclei in that the directly-determined equipotential contours are taken to be fundamental, whereas most other approaches introduce at least partially ambiguous deformation parameters designed to describe the deformed nucleus in terms of distorting a spherical nucleus. Since this approach starts immediately with the deformed potential, the problem of a unique prescription for distorting a spherical potential does not arise.

The approach further differs in that angular localization is expected to be greater for heavy ions than say for α-particles or electrons. Therefore heavy ions ought to be more sensitive to finer details of the nuclear surface, as long as the interaction is confined to the surface, than lighter projectiles. This paradox is based on the fact that although the α-particle has a smaller spatial extent than a heavy ion, interactions with α-particles are not as localized in angle by uncertainty principle considerations because they cannot transfer much average angular momentum in the interaction. The angular localization advantage of the heavy ion begins to break down if the ions overlap too much, due to the sheer spatial extent of the heavy system. However, the confinement of quasielastic heavy-ion reactions to the nuclear surface by strong absorption serves to reduce this possibility.

This approach also differs from pure electromagnetic methods in that it probes both electromagnetic and strong interactions. Therefore it is sensitive to both charge and mass parameters and can provide

TABLE VI-7

THE PARAMETERS $R_0(V)$, $\alpha_2(V)$, AND $\alpha_4(V)$ FOR THE DEFORMED ION-ION POTENTIALS

System	V (MeV)	$R_0(V)$ (fm)	$\alpha_2(V)$	$\alpha_4(V)$
$^{40}Ar + ^{156}Gd$	0.1	1.735	0.203	0.095
	0.5	1.603	0.233	0.087
	1.0	1.546	0.249	0.082
$^{40}Ar + ^{160}Gd$	0.1	1.744	0.226	0.028
	0.5	1.594	0.247	0.032
	1.0	1.529	0.258	0.033
$^{40}Ar + ^{162}Dy$	0.1	1.728	0.202	0.049
	0.5	1.582	0.223	0.049
	1.0	1.525	0.236	0.047
$^{40}Ar + ^{164}Dy$	0.1	1.772	0.198	0.082
	0.5	1.630	0.229	0.068
	1.0	1.571	0.246	0.054
$^{40}Ar + ^{180}Hf$	0.1	1.640	0.201	-0.073
	0.5	1.517	0.220	-0.083
	1.0	1.462	0.243	-0.101

information on possible neutron and proton density differences (isovector) potential) in the nuclear surface. The internal details of this method are much more transparent than the microscopic technique of Seiwert et al. (1981). However, much higher quality data than presented in Figures VI-2 through VI-6 (pp. 112-116) would be necessary for so sensitive an analysis.

The contours shown in Figures VI-7 through VI-11 do not represent the intrinsic shapes of the respective target nuclei. Instead, the ion-ion potential represents a convolution of contributions from both collision partners which must be unfolded in some manner to obtain the true shape for each. Once the equipotential contours have been determined, model-dependent deformation parameters could be deduced by invoking the usual assumptions. For example, from the $^{40}Ar + ^{160}Gd$ data, if one assumes that the 1-MeV contour defines a surface generated by deforming a sharp charge radius $r_c = 1.2\ A_2^{1/3}$ fm and one assumes a spherical projectile, one deduces that $\beta_2 \sim 0.33$ and $\beta_4 \sim 0.04$. These values are in reasonable agreement with other determinations of these quantities (e.g., Erb et al., 1972) but are model dependent. As argued above, the potential contours are more fundamental than the deformation parameters. A still more fundamental approach would be to use folding or proximity descriptions to reproduce the contours.

Guidry, Neese, and Nichols (1981) have applied a deformed folding potential calculation and a deformed proximity potential calculation to the contours determined for the $^{40}Ar + ^{160}Gd$ system. The folding calculation was performed using the Satchler formalism (Satchler and Love, 1979; Satchler, 1979) with two-particle Fermi densities and the ^{160}Gd nuclear density deformed as in Eq. B-6 with $\beta_2 = 0.33$. The

deformed proximity calculation followed the formalism of Randrup and Vaagen (1978) with $\beta_2 = 0.30$. The experimental and theoretical comparisons are shown in Figures VI-12 and VI-13. The theoretical contours agree rather well with the experimental ones, with no parameter adjustment. Therefore, one may conclude that folding and proximity potentials can give a correct description of the average field acting between heavy ions when one of the collision partners is strongly deformed. Since static and dynamical deformations undoubtedly play a significant role in processes such as deep inelastic ones, this provides a necessary (but not a sufficient) test of the ability of these theoretical potentials to describe more general heavy-ion collisions.

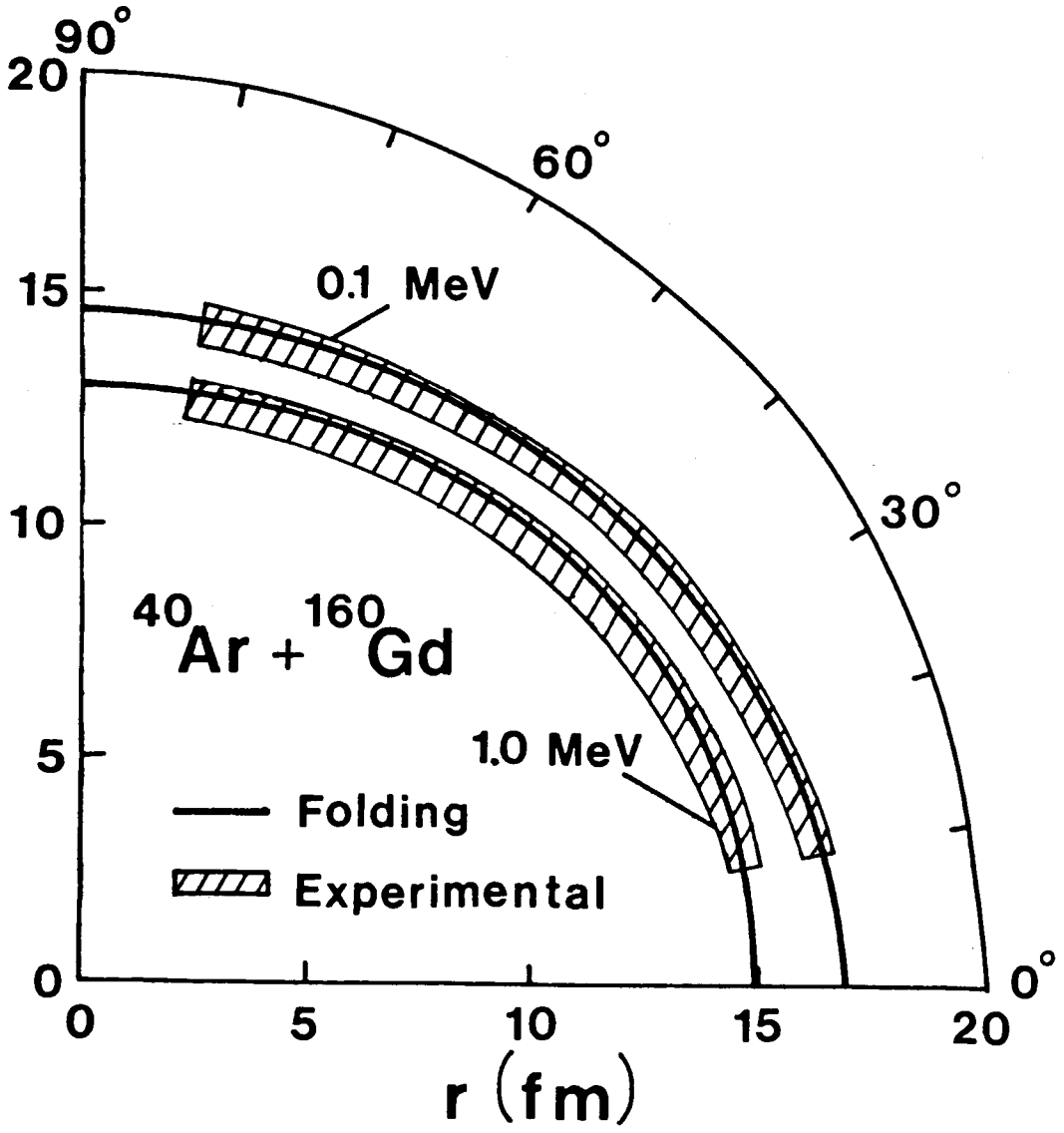


Figure VI-12. Comparison of experimental contours of the ion-ion potential for ^{40}Ar + ^{160}Gd with those calculated using a deformed folding potential. The calculations are indicated by the solid lines and the hashed boxes denote the experimental uncertainties in the contours of Figure VI-8.

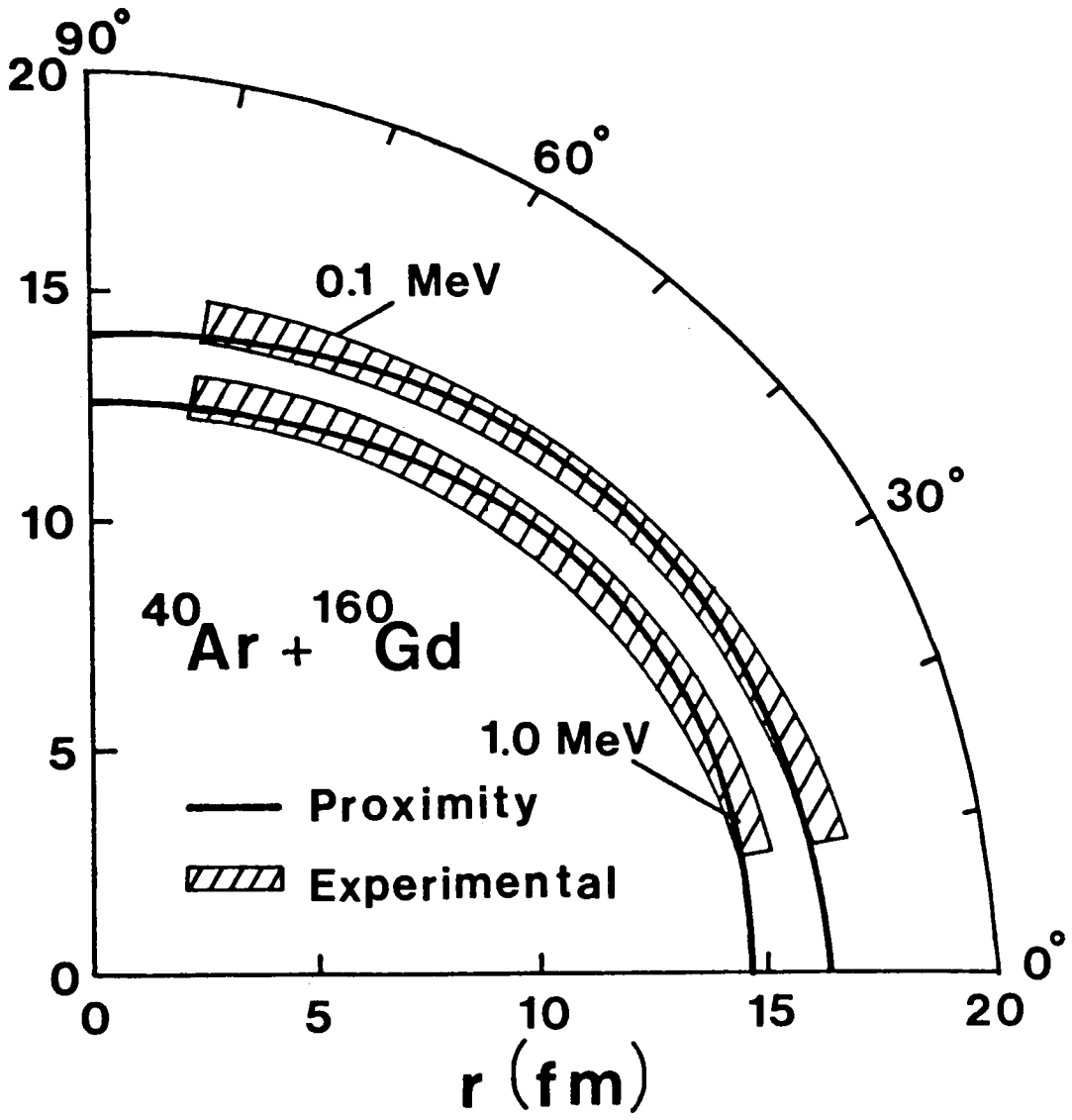


Figure VI-13. Same as Figure VI-12, but for a deformed proximity potential.

CHAPTER VII

CONCLUSIONS AND SUGGESTIONS FOR FUTURE STUDY

Theoretical and experimental methods have been described which allow the study of heavy-ion inelastic scattering from deformed targets. The theoretical methods exploit the classical limit S-matrix (CLSM) formalism to allow tractable calculations and transparent interpretations. The experimental difficulties associated with charged-particle spectroscopy for heavy ions on deformed targets have been circumvented by employing particle-γ-ray coincidence methods. The data obtained by such methods may be interpreted in terms of remarkably simple physical principles, and they demonstrate strikingly the characteristic features associated with imposition of the quantum principles of superposition and uncertainty on classical dynamics. As such, they constitute a quite beautiful example of the relationship between classical and quantum physics, and of the nature of semiclassical approximations. The complementary roles of semiclassical techniques and newly developed heavy-ion quantum-mechanical coupled-channels methods in the study of the structure of heavy deformed nuclei has been emphasized.

This work demonstrates that sensitivity due to phase effects associated with quantum interference structure, localization in radial and angle space, and strong absorption combine to make heavy-ion inelastic scattering an extremely sensitive probe of the surface region of deformed nuclei. These ideas were exploited to demonstrate a method of determining the contours of the global ion-ion potential in a direct manner which is independent of particular parametrizations of the potential. The

contribution to the ion-ion potential of terms associated with adiabatic giant resonance polarization was included explicitly.

It would appear that a systematic and exhaustive study of deformed nuclei using the methods outlined in this dissertation can serve as a definitive testing ground for theories purporting to describe the surface structure of deformed nuclei. Since that surface structure plays a pivotal role in the collective and residual interaction aspects of deformed nuclei, such a systematic study can provide an important contribution to the understanding of low-energy nuclear structure.

Perhaps the best way to proceed would be to obtain precise and complete (i.e., including the states ignored in this analysis) excitation functions for the deformed rare-earths and actinides. Thin targets should be used and the incident beam flux should be measured separately for precise normalization of the excitation probabilities. A wide selection of heavy-ion projectiles should be employed, with beam energies completely spanning the pure Coulomb excitation, CNI, and strong absorption regions. The advent of high-duty-cycle tandem accelerators capable of producing heavy-ion beams at energies near the Coulomb barrier for most deformed nuclei seems conducive to just such a study.

Because of the ambiguous electric moments measured for ^{180}Hf, a detailed investigation of the nuclei in the region where the hexadecapole moments change sign should be made. These nuclei should be studied with both heavy-ion CNI and transfer reactions [perhaps with the method suggested by Guidry et al. (1981b)] to understand the structural basis for the change from "football" to "tin-can" shape.

Any biasing of the final ion-ion potentials, which is due to the Woods-Saxon form used for the nuclear potential, could be removed by employing more general potential forms in the CLSM Hamiltonian. In fact, either a deformed folding potential or deformed proximity potential could be included directly in the CLSM Hamiltonian and the same procedure as outlined in Chapter VI followed to obtain the final contours.

The localization concepts discussed in Chapter IV can be extended to other collective degrees of freedom and hence be exploited to determine other features of nuclear structure. For example, in the context of one- and two-particle heavy-ion transfer reactions, Guidry et al. (1981b) have discussed the possibility of studying single-particle motion and pairing forces in a multi-dimensional space consisting of two (or possibly three, if triaxial degrees of freedom are allowed) spatial dimensions and dimensions corresponding to collective degrees of freedom. Because large amounts of collective stress are involved, some of the collective variables take on large values so that localizations in their conjugate variables are possible in the transfer reaction.

Such localization effects are not restricted to nuclear systems, but occur in any quantum-mechanical system for which a dynamical variable takes on large values and approaches the classical analogue. Furthermore, these localizations should be exploited whenever possible as a precursor to more elaborate quantum-mechanical treatments.

BIBLIOGRAPHY

BIBLIOGRAPHY

Abramowitz, M., and I. A. Stegun, eds., Handbook of Mathematical Functions (Dover, New York, 1972).

Alder, K., and A. Winther, eds., Coulomb Excitation (Academic Press, New York, 1966).

Alder, K., and A. Winther, Electromagnetic Excitation (North-Holland, Amsterdam, 1975).

Baker, F. T., Phys. Rev. Lett. 35, 469 (1975).

Barrett, R. C., and D. F. Jackson, Nuclear Sizes and Structure (Clarendon Press, Oxford, 1977).

Bemis, C. E., Jr., F. K. McGowan, J. L. C. Ford, Jr., W. T. Milner, P. H. Stelson, and R. L. Robinson, Phys. Rev. C8, 1466 (1973).

Bethe, H. A., Phys. Rev. 57, 1125 (1940).

Bingham, C. R., Ph.D. Dissertation, The University of Tennessee, Knoxville (1965), unpublished.

Blocki, J., J. Randrup, W. J. Swiatecki, and C. F. Tsang, Ann. Phys. 105, 427 (1977).

Bohr, A., K. Danske Vidensk. Selsk. Mat.-Fys. Medd. 26, No. 14 (1952).

Bohr, A., and B. R. Mottelson, K. Danske Vidensk. Selsk. Mat.-Fys. Medd. 27, No. 16 (1953).

Bohr, A., and B. R. Mottelson, Nuclear Structure, Vol. I (W. A. Benjamin, New York, 1969).

Bohr, A., and B. R. Mottelson, Nuclear Structure, Vol. II (W. A. Benjamin, New York, 1975).

Broglia, R. A., and A. Winther, Nucl. Phys. A182, 112 (1972a).

Broglia, R. A., and A. Winther, Phys. Rep. 4C, 153 (1972b).

Broglia, R. A., S. Landowne, R. A. Malfliet, V. Rostokin, and A. Winther, Phys. Rep. 11C, 1 (1974).

Broglia, R. A., and A. Winther, Heavy Ion Reactions, Vol. I (Addison-Wesley, Reading, 1981).

Brueckner, K. A., J. R. Buchler, S. Jorna, and R. J. Lombard, Phys. Rev. 171, 1188 (1968).

Camp, D. C., and A. L. Van Lehn, Nucl. Instr. and Meth. 76, 192 (1969).

Collard, H. R., L. R. B. Elton, and R. Hofstadter, in Nuclear Radii, Vol. 2, Group I, Landolt-Börnstein Numerical Data and Functional Relationships in Science and Technology, ed. by K.-H. Hellwege (Springer-Verlag, Berlin, 1967).

Devries, R. M., and M. R. Clover, Nucl. Phys. A243, 528 (1975).

Donangelo, R., Ph.D. Thesis, University of California, Berkeley (1977), report no. LBL-5825.

Donangelo, R., M. W. Guidry, J. P. Boisson, and J. O. Rasmussen, Phys. Lett. 64B, 377 (1976).

Donangelo, R., L. F. Oliviera, J. O. Rasmussen, and M. W. Guidry, Nucl. Phys. A308, 136 (1978).

Donangelo, R., M. W. Guidry, R. E. Neese, and M. J. Rhoades-Brown, submitted to Phys. Lett. B (1981).

Dover, C. B., and J. P. Vary, in Classical and Quantum Mechanical Aspects of Heavy Ion Collisions, ed. by H. L. Harney, P. Braun-Munzinger, and C. K. Gelbke (Springer-Verlag, Berlin, 1975), p. 1.

Dragoun, O., Z. Plajner, and F. Schmutzler, in Internal Conversion Coefficients for Multipolarities E1, ... , E4, M1, ... , M4, ed. by K. Way (Academic Press, New York, 1973), p. 329; reprinted from Nucl. Data A9, 119 (1971).

Drisko, R. M., G. R. Satchler, and R. H. Bassel, Phys. Rev. Lett. 5, 347 (1963).

Eichler, E., N. R. Johnson, R. O. Sayer, D. C. Hensley, and L. L. Riedinger, Phys. Rev. Lett. 30, 568 (1973).

Erb, K. A., J. E. Holden, I. Y. Lee, J. X. Saladin, and T. K. Saylor, Phys. Rev. Lett. 29, 1010 (1972).

Feshbach, H., C. E. Porter, and V. F. Weisskopf, Phys. Rev. 90, 166 (1953).

Feshbach, H., C. E. Porter, and V. F. Weisskopf, Phys. Rev. 96, 448 (1954).

Flocard, H., P. Quentin, and D. Vautherin, Phys. Lett. 46B, 304 (1973).

Ford, K. W., and J. A. Wheeler, Ann. Phys. (N.Y.) 7, 259 (1959a).

Ford, K. W., and J. A. Wheeler, Ann. Phys. (N.Y.) 7, 287 (1959b).

Fukuda, S., and Y. Torizuka, Phys. Rev. Lett. 29, 1109 (1972).

Gareev, J. A., S. P. Ivanova, V. V. Pashkevich, Yad. Fiz. 11, 1200 (1970) [Sov. J. Nucl. Phys. 11, 667 (1970)].

Glendenning, N. K., Rev. Mod. Phys. 47, 659 (1975).

Goldberg, A., H. M. Schey, and J. L. Schwartz, Am. J. Phys. 35, 177 (1967).

Grunder, H. A., and F. B. Selph, Ann. Rev. Nucl. Sci. 27, 353 (1977).

Guidry, M. W., H. Massmann, R. Donangelo, and J. O. Rasmussen, Nucl. Phys. A274, 183 (1976a).

Guidry, M. W., P. A. Butler, P. Colombani, I. Y. Lee, D. Ward, R. M. Diamond, F. S. Stephens, E. Eichler, N. R. Johnson, and R. Sturm, Nucl. Phys. A266, 228 (1976b).

Guidry, M. W., P. A. Butler, R. Donangelo, E. Grosse, Y. El Masri, I. Y. Lee, F. S. Stephens, R. M. Diamond, L. L. Riedinger, C. R. Bingham, A. C. Kahler, J. A. Vrba, E. L. Robinson, and N. R. Johnson, Phys. Rev. Lett. 40, 1016 (1978a).

Guidry, M. W., R. Donangelo, J. O. Rasmussen, and J. P. Boisson, Nucl. Phys. A295, 482 (1978b).

Guidry, M. W., R. E. Neese, and T. L. Nichols, invited paper presented at the Workshop in Nuclear Physics, Drexel University, September, 1980, to be published in Contemporary Research in Nuclear Physics (Plenum Press, New York, 1981).

Guidry, M. W., R. E. Neese, C. R. Bingham, L. L. Riedinger, J. A. Vrba, I. Y. Lee, N. R. Johnson, P. A. Butler, R. Donangelo, and J. O. Rasmussen, submitted to Nucl. Phys. A (1981a).

Guidry, M. W., T. L. Nichols, R. E. Neese, J. O. Rasmussen, L. F. Oliviera, and R. Donangelo, Nucl. Phys. A361, 275 (1981b).

Hager, R. S., and E. C. Seltzer, in Internal Conversion Coefficients for Multipolarities E1, ... , E4, M1, ... , M4, ed. by K. Way (Academic Press, New York, 1973), p. 1; reprinted from Nucl Data A4, 1 (1968).

Harney, H. L., P. Braun-Munzinger, and C. K. Gelbke, Z. Physik 269, 339 (1974).

Heath, R. L., Scintillation Spectrometry Gamma-Ray Spectrum Catalogue, Vol. I, A.E.C. Report IDO-16880-1 (1964).

Hodgson, P. E., Nuclear Reactions and Nuclear Structure (Clarendon Press, Oxford, 1971).

Hodgson, P. E., Nuclear Heavy-Ion Reactions (Clarendon Press, Oxford, 1978).

Hubert, F., A. Fleury, R. Bimbot, and D. Gardes, Report CENBG 7821/ IPNO-RC-7807, Centre D'Etudes Nucleaires de Bordeaux-Gradignan/ Institut de Physique Nucleaire Orsay (1978).

Hubert, F., A. Fleury, R. Bimbot, and D. Gardes, Ann. Phys. (Fr.) 5 (Suppl.), 1 (1980).

Igo, G., Phys. Rev. 115, 1665 (1959).

Kahler, A. C., Ph.D. Dissertation, The University of Tennessee, Knoxville (1978), unpublished.

Krane, K. S., Nucl. Instr. and Meth. 109, 401 (1973).

Krappe, H. J., Ann. Phys. (N.Y.) 99, 142 (1976).

Krappe, H. J., J. R. Nix, and A. J. Sierk, Phys. Rev. C20, 992 (1979).

Lee, I. Y., private communication (1978).

Lee, I. Y., private communication (1981).

Lee, I. Y., J. X. Saladin, J. Holden, J. O'Brien, C. Baktash, C. Bemis, Jr., P. H. Stelson, F. K. McGowan, W. T. Milner, J. L. C. Ford, Jr., R. L. Robinson, and W. Tuttle, Phys. Rev. C12, 1483 (1975).

Levit, S., U. Smilansky, and D. Pelte, Phys. Lett. 53B, 39 (1974).

Lombard, R. J., Ann. Phys. (N.Y.) 77, 380 (1973).

Love, W. G., T. Teresawa, and G. R. Satchler, Nucl. Phys. A291, 183 (1977).

Mackintosh, R. S., Nucl. Phys. A245, 255 (1975).

Mackintosh, R. S., Rep. Prog. Phys. 40, 731 (1977).

Malfliet, R. A., S. Landowne, and V. Rostokin, Phys. Lett. 44B, 238 (1973).

Marmier, P., and E. Sheldon, Physics of Nuclei and Particles, Vol. II (Academic Press, New York, 1970).

Massmann, H., Ph.D. Thesis, University of California, Berkeley (1975), report no. LBL-4316.

Massmann, H., and J. O. Rasmussen, Nucl. Phys. A243, 155 (1975).

Moffa, P. J., C. B. Dover, and J. P. Vary, Phys. Rev. C13, 147 (1976).

Mottelson, B. R., and S. G. Nilsson, K. Danske Vidensk. Selsk. Mat.-Fys. Skr. 1, No. 8 (1959).

Myers, W. D., Nucl. Phys. A204, 465 (1973).

Neese, R. E., M. W. Guidry, R. Donangelo, and J. O. Rasmussen, Phys. Lett. 85B, 201 (1979).

Neese, R. E., and M. W. Guidry, submitted to Phys. Rev. C (1981).

Nerlo-Pomorska, B., Nucl. Phys. A259, 481 (1976).

Ngô, C., B. Tamain, M. Beiner, R. J. Lombard, D. Mas, and H. H. Deubler, Nucl. Phys. A252, 237 (1975).

Nilsson, S. G., K. Danske Vidensk. Selsk. Mat.-Fys. Medd. 29, No. 16 (1955).

Nörenberg, W., and H. A. Weidenmüller, Introduction to the Theory of Heavy-Ion Collisions (Springer-Verlag, Berlin, 1980).

Northcliffe, L. C., and R. F. Schilling, Nucl. Data A7, 233 (1970).

Oberacker, V., and G. Soff, Z. Naturforsch. 32a, 1465 (1977).

Powell, M. J. D., Comp. J. 7, 303 (1965).

Preston, M. A., and R. K. Bhaduri, Structure of the Nucleus (Addison-Wesley, Reading, 1975).

Rainwater, J., Phys. Rev. 79, 432 (1950).

Randrup, J., and J. S. Vaagen, Phys. Lett. 77B, 170 (1978).

Rasmussen, J., P. Möller, M. Guidry, and R. Neese, Nucl. Phys. A341, 149 (1980).

Rhoades-Brown, M., M. H. Macfarlane, and S. C. Pieper, Phys. Rev. C21, 2417 (1980a).

Rhoades-Brown, M., M. H. Macfarlane, and S. C. Pieper, Phys. Rev. C21, 2436 (1980b).

Rhoades-Brown, M., R. Donangelo, M. W. Guidry, and R. E. Neese, submitted to Phys. Rev. Lett. (1981).

Roesel, F., J. X. Saladin, and K. Alder, Comp. Phys. Comm. 8, 35 (1974).

Ronningen, R. M., J. H. Hamilton, L. Varnell, J. Lange, A. V. Ramayya, G. Garcia-Bermudez, W. Lourens, L. L. Riedinger, F. K. McGowan, P. H. Stelson, R. L. Robinson, and J. L. C. Ford, Jr., Phys. Rev. C16, 2208 (1977).

Rook, J. R., Phys. Lett. 48B, 148 (1974).

Rutherford, E., Phil. Mag. 21, 669 (1911).

Satchler, G. R., Phys. Lett. 59B, 121 (1975).

Satchler, G. R., Nucl. Phys. A329, 233 (1979).

Satchler, G. R., private communication (1980).

Satchler, G. R., private communication (1981).

Satchler, G. R., and W. G. Love, Phys. Rep. C55, 183 (1979).

Sayer, R. O., Ph.D. Dissertation, The University of Tennessee, Knoxville (1968), unpublished.

Sayer, R. O., J. S. Smith III, and W. T. Milner, Atomic Data and Nuclear Data Tables 15, 85 (1975).

Scheid, W., and W. Greiner, Z. Physik 226, 364 (1969).

Schmidt-Böcking, H., in Experimental Methods in Heavy Ion Physics, ed. by K. Bethge (Springer-Verlag, Heidelberg, 1978), p. 81.

Seiwert, M., P. O. Hess, J. A. Maruhn, and W. Greiner, Phys. Rev. C23, 2335 (1981).

Sinha, B., Phys. Rep. C20, 1 (1975).

Spear, R. H., T. H. Zabel, D. C. Kean, A. M. R. Joye, A. M. Baxter, M. P. Fewell, and S. Hinds, Phys. Lett. 76B, 559 (1978).

Strutinski, V. M., Zh. Eksp. Teor. Fiz. 46, 2078 (1964) [Sov. Phys. JETP 19, 1401 (1964)].

Tamura, T., Ann. Rev. Nucl. Sci. 19, 99 (1969).

Torizuka, Y., Y. Kojima, K. Itoh, A. Nakada, S. Mitsunobu, M. Nagao, K. Hosoyama, S. Fukuja, and H. Miua, in Proc. Int. Conf. on Photonuclear Reactions and Applications, March, 1973, ed. by B. Berman (CONF-730301).

Vassy, D., and J. Smith, FORTRAN computer program SOLCOR (1973), unpublished.

Ward, D., P. Colombani, I. Y. Lee, P. A. Butler, R. S. Simon, R. M. Diamond, and F. S. Stephens, Nucl. Phys. A266, 194 (1976).

Winther, A., and J. de Boer, in Coulomb Excitation, ed. by K. Alder and A. Winther (Academic Press, New York, 1966), p. 303.

Wollersheim, H. J., and T. W. Elze, Nucl. Phys. A278, 87 (1977).

Woods, R. D., and D. S. Saxon, Phys. Rev. 95, 577 (1954).

APPENDICES

APPENDIX A

EFFECTIVE POLARIZATION POTENTIALS FOR ADIABATIC COULOMB COUPLING TO GIANT RESONANCES IN HEAVY-ION SCATTERING

Recently, Rasmussen et al. (1980) have demonstrated that terms arising from adiabatic Coulomb coupling to the isovector giant dipole resonance and isoscalar and isovector giant quadrupole resonances in heavy-ion collisions can dominate the far tail of the effective ion-ion potential. Because Coulomb-nuclear interference experiments with heavy ions represent such a sensitive probe of the nucleus-nucleus potential in the far tail, care should be taken to incorporate rigorously all significant terms. Although the relative magnitude of such polarization potentials was found to be small for the ion-ion potentials determined in Chapter VI, forms for the adiabatic giant dipole and quadrupole resonances analogous to those of Rasmussen et al. (1980) were incorporated directly into the CLSM model Hamiltonian (Eq. III-3), where they are collectively represented by the term $V_{pol}(r,\chi)$. This appendix contains derivations of the specific expressions used for $V_{pol}(r,\chi)$ in the computer codes to calculate excitation probabilities.

I. THE GIANT ELECTRIC DIPOLE POLARIZATION POTENTIAL

To begin with, consider the simple case of a spherical projectile and a spherical target nucleus and allow only the target nucleus to be excited. Let α represent the displacement of the center of charge from the center of mass in the nucleus excited into the giant resonance and

let r be the distance between the center of the projectile and the center of the target nucleus (see Figure A-1). Because the excitation is assumed to be adiabatic, only the potential energy part of the Hamiltonian,

$$V = \frac{Z_P Z_T e^2}{r(1+\frac{\alpha}{r})} + \frac{1}{2} C \alpha^2 , \tag{A-1}$$

needs to be considered. In Eq. A-1, $Z_P e$ and $Z_T e$ are the charges of the projectile and target nucleus, respectively, and C is a vibrational spring constant for the resonance. In general,

$$\frac{\alpha}{r} << 1 \tag{A-2}$$

so that the first term on the right-hand side of Eq. A-1 can be expanded in terms of $(\frac{\alpha}{r})$. Hence, to first order in $(\frac{\alpha}{r})$,

$$V \approx \frac{Z_P Z_T e^2}{r} - \frac{\alpha Z_P Z_T e^2}{r^2} + \frac{1}{2} C \alpha^2 . \tag{A-3}$$

Differentiating Eq. A-3 with respect to α and setting the result equal to zero, one obtains

$$\frac{\partial V}{\partial \alpha} = 0 = - \frac{Z_P Z_T e^2}{r^2} + C \alpha . \tag{A-4}$$

Solving Eq. A-4 for the value of α at the potential minimum, one gets

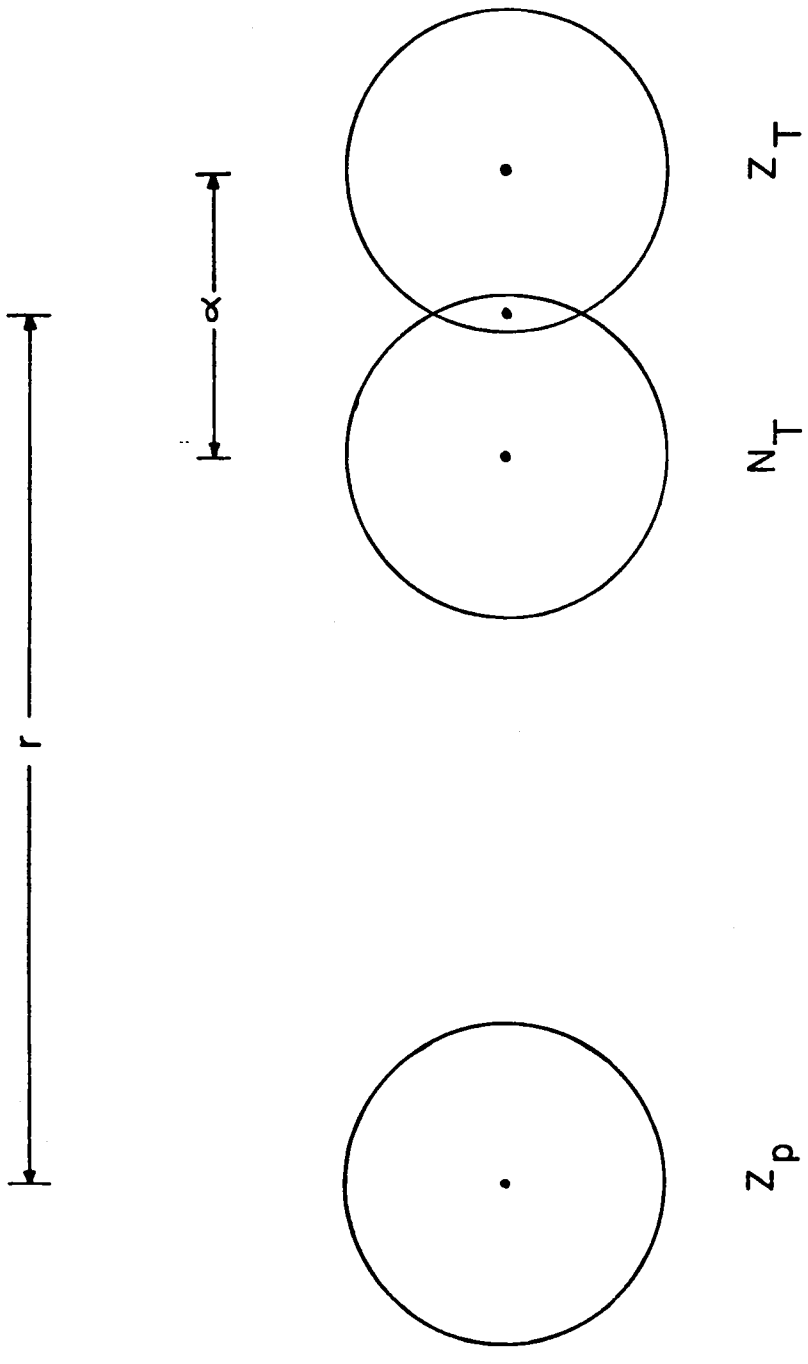


Figure A-1. Simple model of giant dipole resonance excitation.

$$\alpha_{min} \approx \frac{1}{C} \frac{Z_P Z_T e^2}{r^2} . \qquad \text{(A-5)}$$

Substitution of Eq. A-5 into Eq. A-3 gives

$$V_{min} \approx \frac{Z_P Z_T e^2}{r} - \frac{1}{2C} \frac{(Z_P Z_T e^2)^2}{r^4} , \qquad \text{(A-6)}$$

the value of the potential at the minimum. The potential due to excitation of the giant dipole resonance, $V_{pol}^{\lambda=1}(r)$, is obtained by subtracting the monopole-monopole Coulomb potential V_{Coul} from V_{min}. That is,

$$\begin{aligned} V_{pol}^{\lambda=1}(r) &\approx V_{min} - V_{Coul} \\ &\approx \left[\frac{Z_P Z_T e^2}{r} - \frac{1}{2C} \frac{(Z_P Z_T e^2)^2}{r^4}\right] - \frac{Z_P Z_T e^2}{r} \\ &\approx -\frac{1}{2C} \frac{(Z_P Z_T e^2)^2}{r^4} . \end{aligned} \qquad \text{(A-7)}$$

Equation A-7 shows that the giant dipole polarization potential is attractive and varies as the inverse fourth power of the radial separation. Because both projectile and target nucleus can be polarized, the net giant dipole polarization potential for spherical collision partners is given by

$$V_{pol}^{\lambda=1}(r) \approx -\left(\frac{1}{C_P} + \frac{1}{C_T}\right) \frac{(Z_P Z_T e^2)^2}{2r^4} \qquad \text{(A-8)}$$

where C_P and C_T are the spring constants for the projectile and target nucleus, respectively.

Now consider the more complicated case of a spherical projectile and an axially symmetric statically deformed target nucleus. The electric field $\vec{E}$ of the projectile can induce an average dipole moment $\langle\vec{d}\rangle$ in the target nucleus (see Figure A-2). The direction of $\langle\vec{d}\rangle$ in general is not parallel to that of $\vec{E}$, but depends instead on the orientation of the rotor (specified by the angle χ in Figure A-2). [That is, $\theta = \theta(\chi)$. However, as a first order estimate assume $\theta \approx \chi$.] A torque which can rotationally excite the rotor arises from the interaction between $\langle\vec{d}\rangle$ and $\vec{E}$ (analogous to the typical monopole-multipole torque in Coulomb excitation). The dipole polarization potential for excitation of the target nucleus is given by

$$V_T^{\lambda=1}(r,\chi) = -\frac{1}{2}\langle\vec{d}\rangle \cdot \vec{E} \ . \qquad \text{(A-9)}$$

Alder and Winther (1975, Appendix H) show that the component of $\langle\vec{d}\rangle$ in the direction of $\vec{E}$ is

$$d_E = EP_{0T}R_T^2(\chi)/R_{0T}^2 \ , \qquad \text{(A-10)}$$

where E is the magnitude of $\vec{E}$, P_{0T} is the polarizability of the target nucleus, and the nuclear surface $R_T(\theta,\phi)$ is defined by Eq. II-4 with the radius parameter R_{0T}. For an axially symmetric nucleus, by using Eq. II-6 and the approximation that volume conservation terms can be neglected, Eq. A-10 can be recast as

$$d_E = EP_{0T}[1 + \beta_2 Y_{20}(\chi) + \ldots]^2 \ . \qquad \text{(A-11)}$$

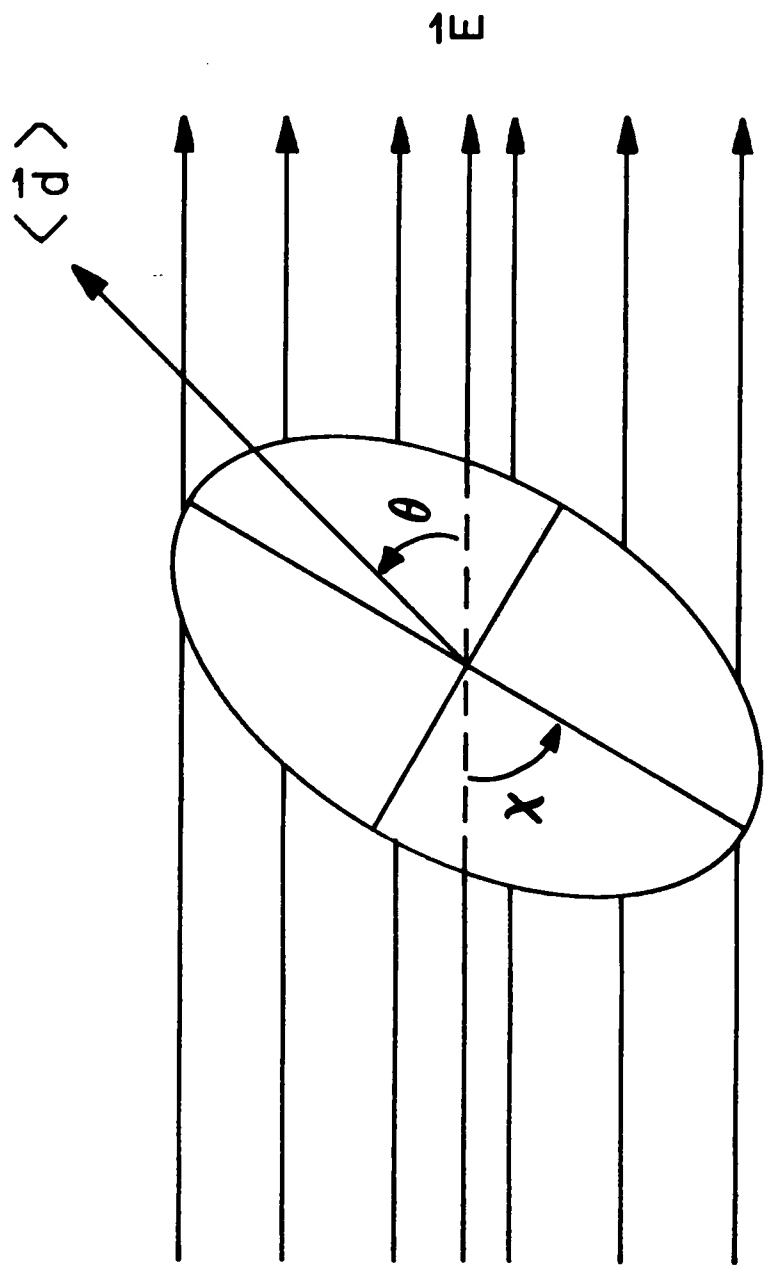


Figure A-2. The induced dipole moment $\langle\vec{d}\rangle$ for an axially symmetric deformed nucleus in an external homogeneous electric field $\vec{E}$. The angles θ and χ specify the direction of $\langle\vec{d}\rangle$ and the orientation angle of the rotor, respectively. The torque from the interaction between $\langle\vec{d}\rangle$ and $\vec{E}$ can cause rotational excitation of the nucleus. This figure is an adaptation of one due to Alder and Winther (1975, Appendix J, Figure 1).

where $B(E1;\ n_1 = 0 \rightarrow n_1 = 1)$ is a reduced transition strength for dipole transitions to the giant resonance and $\hbar\omega_1$ is the energy of the resonance. If one assumes that the giant dipole resonance exhausts all of the E1 strength in the energy-weighted dipole sum rule (Bohr and Mottleson, 1975, Eqs. 6-172 and 6-176), then

$$S(E1) \approx \hbar\omega_1 B(E1;\ n_1 = 0 \rightarrow n_1 = 1)$$

$$\approx \frac{9}{4\pi} \frac{\hbar^2}{2M_0} \frac{NZ}{A} e^2 \ . \qquad \text{(A-17)}$$

In Eq. A-17, M_0 is the nuclear mass constant and N, Z, and A are the neutron number, atomic number, and atomic mass number of the excited nucleus, respectively. Substitution of Eq. A-17 into Eq. A-16 results in

$$P_0 \approx \frac{NZ\ e^2}{M_0 A \omega_1^2} \ . \qquad \text{(A-18)}$$

Using the semiempirical value

$$\hbar\omega_1 \approx 80A^{1/3}\ \text{MeV} \qquad \text{(A-19)}$$

for the energy of the giant dipole resonance and substituting the values of the constants, one arrives at the convenient expression

$$P_0 \approx 9.34 \times 10^{-3}\ NZA^{-1/3}\ \ \text{fm}^3 \ . \qquad \text{(A-20)}$$

Using Eq. A-20 and substituting values for physical constants enables one to recast Eq. A-15 as follows:

$$V_{pol}^{\lambda=1}(r,\chi) = -\frac{k_1}{r^4}\{1 + k_2[1 + 2\beta_2 Y_{20}(\chi)]\}\ , \qquad \text{(A-21)}$$

where

$$k_1 = 6.72 \times 10^{-3}\ Z_T^2 N_P Z_P A_P^{-1/3}\ \ \text{MeV - fm}^4 \qquad \text{(A-22)}$$

and

$$k_2 = \frac{Z_P N_T}{Z_T N_P}\left(\frac{A_P}{A_T}\right)^{1/3}\ . \qquad \text{(A-23)}$$

(In Eq. A-21, r should be measured in fm.) Equation A-21 provides the precise form of $V_{pol}^{\lambda=1}(r,\chi)$ used in the computer codes to make the calculations discussed in Chapter VI.

II. THE GIANT QUADRUPOLE POLARIZATION POTENTIALS

Consider the scattering of a spherical on spherical system (the complication of static deformation effects will be neglected in first order because quadrupole polarization potentials were found to be much less than dipole polarization potentials). The quadrupole polarization potential receives contributions from induced quadrupole moments in both collision partners and a contribution from the potential energy from induced deformations. First, treat the case of the isoscalar (T = 0) giant quadrupole resonance. Once again, because the excitation process is assumed to be adiabatic, only the potential energy for the polarization effects must be considered:

$$V = (Z_P Q_T + Z_T Q_P) \frac{e^2}{2r^3} + \frac{1}{2} C_P \beta_P{}^2 + \frac{1}{2} C_T \beta_P{}^2 \qquad \text{(A-24)}$$

In Eq. A-24, $Z_P e$ and $Z_T e$ are the charges of the projectile and target nucleus respectively, Q_P and Q_T are the respective induced quadrupole moments, β_P and β_T are the respective induced deformations, and C_P and C_T are the respective spring constants for the resonances. Assume that the induced deformation is well described (to lowest order in the deformation parameter β) by a uniform sharp cutoff charge distribution with a time-varying surface given by

$$R(\theta) = R_{oi}[1 + \beta_i Y_{20}(\theta)] , \qquad \text{(A-25)}$$

where $R_{oi} = 1.2\ A_i^{1/3}$ $(i = P,T)$ and θ is a polar angle in the intrinsic frame. Hence, to first order in β,

$$Q_i = \frac{3Z_i R_{oi}^2 \beta_i}{\sqrt{5\pi}} . \qquad \text{(A-26)}$$

Substitution of Eq. A-26 into Eq. A-24 gives

$$V = \alpha_T Z_P \beta_T + \alpha_P Z_T \beta_P + \frac{1}{2} C_P \beta_P^2 + \frac{1}{2} C_T \beta_T^2 , \qquad \text{(A-27)}$$

where

$$\alpha_i \equiv \frac{3Z_i R_{oi}^2}{\sqrt{5\pi}} \frac{e^2}{2r^3} . \qquad \text{(A-28)}$$

In the adiabatic limit one is interested in the minimum of V with respect to the induced deformation parameters β_P and β_T. Performing the partial differentiations on Eq. A-27 and setting results equal to zero, one obtains

$$\frac{\partial V}{\partial \beta_P} = \alpha_P Z_T + C_P \beta_P = 0 \; ; \tag{A-29}$$

$$\frac{\partial V}{\partial \beta_T} = \alpha_T Z_P + C_T \beta_T = 0 \; . \tag{A-30}$$

Hence, at equilibrium

$$\beta_P = - \frac{\alpha_P Z_T}{C_P} \tag{A-31}$$

and

$$\beta_T = - \frac{\alpha_T Z_P}{C_T} \; . \tag{A-32}$$

Substitution of Eq. A-31 and Eq. A-32 into Eq. A-27 yields the following expression for the adiabatic isoscalar giant quadrupole resonance:

$$V_{pol}^{\lambda=2,T=0}(r) = - \frac{9}{40\pi} \left[\frac{R_{0T}^4}{C_T} + \frac{R_{0P}^4}{C_P} \right] \frac{Z_P^2 Z_T^2 e^2}{r^6} \; . \tag{A-33}$$

Note that the adiabatic isoscalar giant quadrupole resonance is attractive and varies as the inverse sixth power of the radial separation.

The spring constants C_p and C_T for the isoscalar giant quadrupole resonance can be estimated with the aid of the classical oscillator

sum rule (Bohr and Mottleson, 1975, Eq. 6-179a)

$$S(T=0;\lambda)_{class} = \frac{\lambda(2\lambda+1)^2}{4\pi}\frac{\hbar^2}{2M_0} A \langle r^{2\lambda-2}\rangle , \qquad (A-34)$$

where A and M_0 are defined as in Eq. A-17 and $\langle r^\lambda\rangle$ is a radial moment of order λ. Setting $\lambda = 2$ and evaluating constants in Eq. A-34, one gets

$$S(T=0;\lambda=2)_{class} = 82.6\ A \langle r^2\rangle \ \text{MeV-fm}^2 . \qquad (A-35)$$

For an oscillator potential the radial moments are defined by (Bohr and Mottleson, 1969, Eq. 2-65)

$$\langle r^\lambda\rangle \approx \frac{3}{\lambda+3} R^\lambda , \qquad (A-36)$$

where $R(\approx 1.2\ A^{1/3})$ is the effective nuclear radius. Hence,

$$\langle r^2\rangle \approx 0.864\ A^{2/3}\ \text{fm}^2 , \qquad (A-37)$$

from which one can write

$$S(T=0;\lambda=2)_{class} \approx 71.4\ A^{5/3}\ \text{MeV - fm}^4 . \qquad (A-38)$$

Assume that the $\lambda = 2$, $T = 0$ resonance lies at an energy

$$\hbar\omega_2 \approx 60\ A^{-1/3}\ \text{MeV} \qquad (A-39)$$

and completely exhausts the strength of the energy-weighted sum rule. That is,

$$S(T=0;\lambda=2)_{class} \approx B(T=0;\lambda=2)\hbar\omega_2 \ , \qquad \text{(A-40)}$$

where $B(T=0;\lambda=2)$ is a reduced transition rate for excitation of the isoscalar quadrupole resonance. From Eqs. A-38 through A-40,

$$B(T=0;\lambda=2) \approx 1.2\ A^2 \ \ \text{fm}^4 \ . \qquad \text{(A-41)}$$

If the ratio of the proton and neutron densities is assumed to be constant in the vibrational motion, then (Bohr and Mottleson, 1975, Eq. 6-182) -

$$B(T=0;\lambda=2) \approx \left(\frac{A}{Ze}\right)^2 B(E2;\ n_2 = 0 \rightarrow n_2 = 1) \ . \qquad \text{(A-42)}$$

Bohr and Mottleson (1975, Eq. 6-180) show that

$$B(E2;\ n_2 = 0 \rightarrow n_2 = 1) = \frac{5\hbar^2}{2D_2(\hbar\omega_2)} \left(\frac{3ZeR^2}{4\pi}\right)^2 \ , \qquad \text{(A-43)}$$

where D_2 is the inertial mass parameter for the $\lambda = 2$ vibration. Now (Bohr and Mottleson, 1975, Eq. 6-13)

$$\omega_2 = \left(\frac{C_2}{D_2}\right)^{1/2} \ , \qquad \text{(A-44)}$$

where C_2 is the $\lambda = 2$ spring constant, so that

$$D_2 = \frac{C_2}{\omega_2^2} \ . \qquad \text{(A-45)}$$

Substituting Eqs. A-43 and A-45 into Eq. A-42 and solving for C_2, one finds

$$C_2 \approx \frac{5}{2} \frac{\hbar\omega_2}{B(T=0;\lambda=2)} \left(\frac{3}{4\pi} A R^2\right)^2 . \qquad \text{(A-46)}$$

Hence, using Eqs. A-39 and A-41, setting $R \approx 1.2 A^{1/3}$, and substituting values for the constants enables one to write a simple formula for the spring constant:

$$C_2 \approx 14.8 A \quad \text{MeV} . \qquad \text{(A-47)}$$

The isoscalar giant quadrupole potential now can be written in the very simple form

$$V_{pol}^{\lambda=2,T=0}(r) \approx - \frac{k_3}{r^6} , \qquad \text{(A-48)}$$

where

$$k_3 = \frac{9}{40\pi} \left[\frac{R_{0T}^4}{C_T} + \frac{R_{0P}^4}{C_P}\right] Z_P^2 Z_T^2 e^2 \quad \text{MeV - fm}^6$$

$$= \frac{9}{40\pi} \left[\frac{(1.2 A_T^{1/3})^4}{14.8 A_T} + \frac{(1.2 A_P^{1/3})^4}{14.8 A_P}\right] Z_P^2 Z_T^2 e^2 \quad \text{MeV - fm}^6$$

$$= 2.09 \times 10^{-2} [A_T^{1/3} + A_P^{1/3}] Z_P^2 Z_T^2 \quad \text{MeV - fm}^6 . \qquad \text{(A-49)}$$

The isovector (T = 1) giant quadrupole resonance is presumed to lie at approximately twice the energy of the isoscalar (T = 0) giant quadrupole resonance [see Torizuka et al. (1973, Figure 12) and Fukuda and Torizuka (1972)]. The inertial mass parameter D_2 for the isovector mode should be roughly the same as for the isoscalar mode, at least for nuclei with $N \sim Z$. Hence, from Eq. A-45, the spring constant

C_2 for the isovector mode should be approximately four times that of the isoscalar mode. Therefore,

$$V_{pol}^{\lambda=2,T=1}(r) \approx - \frac{k_3}{4r^6} . \qquad \text{(A-50)}$$

Let

$$k_4 = \frac{5}{4} k_3 = 2.61 \times 10^{-2} \left[A_T^{1/3} + A_p^{1/3}\right] Z_p^2 Z_T^2 \ \text{MeV - fm}^6 . \qquad \text{(A-51)}$$

Hence, the net adiabatic giant quadrupole resonance potential (including both isoscalar and isovector terms) used in the calculations described in Chapter VI is given by

$$V_{pol}^{\lambda=2}(r) \approx - \frac{k_4}{r^6} . \qquad \text{(A-52)}$$

To summarize, the total giant resonance adiabatic polarization potential is given by

$$\begin{aligned} V_{pol}(r,\chi) &\approx V_{pol}^{\lambda=1}(r,\chi) + V_{pol}^{\lambda=2}(r) \\ &\approx - \frac{k_1}{r^4} \{1 + k_2[1 + 2\beta_2 Y_{20}(\chi)]\} - \frac{k_4}{r^6} . \end{aligned} \qquad \text{(A-53)}$$

APPENDIX B

JUSTIFICATION FOR NEGLECTING TERMS DUE TO CHARGE DISTRIBUTION OVERLAP IN THE ELECTRIC INTERACTION POTENTIAL

A commonly used form for the electric interaction potential V_c in heavy-ion reactions is the "point charge potential" (sometimes referred to as the "shielded Coulomb potential")

$$V_c(R) = \begin{cases} Z_1 Z_2 e^2/R, & R \geq R_1 + R_2 \\ \dfrac{Z_1 Z_2 e^2}{2(R_1 + R_2)} \left[3 - \left(\dfrac{R}{R_1 + R_2}\right)^2\right], & R < R_1 + R_2 \,. \end{cases} \qquad \text{(B-1)}$$

In Eq. B-1, $Z_1 e$ and $Z_2 e$ are the charges of the projectile and target nucleus, respectively, R_1 and R_2 (where $R_i = 1.2\ A_i^{1/3}$) are equivalent sharp cutoff radii, and R is the distance between centers.

Devries and Clover (1975) demonstrate that the point charge potential is a very good approximation for elastic scattering and transfer reaction calculations, so long as R is not too small. Their arguments are based on comparisons to more correct double sharp cutoff folded potentials and double Fermi folded potentials. Three important points are made in their paper.

1. Beyond $R = 1.2\ (A_1^{1/3} + A_2^{1/3})$ the values obtained for V_c using the three prescriptions differ by less than 0.1%.

2. At R = 0 the point charge V_c is 40-50% less than the double Fermi folded V_c.
3. Beyond R = 0.86 $(A_1^{1/3} + A_2^{1/3})$ the double sharp folded V_c differs from the double Fermi folded V_c by less than 0.1%. At R = 0 they differ by no more than 7%.

(They also provide analytic expressions for the double sharp folded potential valid for $0 \leq R < \infty$).

Clearly, from points one and three above, the standard monopole-monopole Coulomb interaction is sufficient for $R \geq R_1 + R_2$ (especially for the case of Fermi-like distributions with small diffuseness). Any corrections would be obscured by the experimental uncertainties in the nuclear potentials determined via the technique described in Chapter VI. Table B-1 lists values of the sum

$$R_1 + R_2 = 1.2\ (A_1^{1/3} + A_2^{1/3}) \qquad \text{(B-2)}$$

for the systems studied in this work. Based on typical CLSM calculations for those systems for energies in the range sampled experimentally, trajectories for which $R \lesssim 1.8$ a [where a is half of the distance of closest approach for a monopole-monopole Coulomb potential (see Eq. VI-18)] are strongly damped by the imaginary nuclear potential. Define

$$D_{min} = 1.8\ a\ . \qquad \text{(B-3)}$$

Therefore, for values of $R < D_{min}$, corrections to any of the electric interaction terms are irrelevant because they are masked by effects from a multitude of nuclear reaction channels. Values of D_{min} for the

TABLE B-1

VALUES OF THE SUM $R_1 + R_2$ AND D_{min} FOR THE SYSTEMS STUDIED

System	$R_1 + R_2$ (Fm)	D_{min} (Fm)
$^{40}Ar + ^{156}Gd$	10.56	10.72
$^{40}Ar + ^{160}Gd$	10.62	10.66
$^{40}Ar + ^{162}Dy$	10.65	10.97
$^{40}Ar + ^{164}Dy$	10.67	10.94
$^{40}Ar + ^{180}HF$	10.88	11.73

Note: $R_1 + R_2$ is calculated with Eq. B-2 and D_{min} is calculated with Eq. B-3.

scattering of 175-MeV ^{40}Ar projectiles from the rare-earth target nuclei of this study are also listed in Table B-1. Note that in all cases $D_{min} \gtrsim R_1 + R_2$. Therefore, to a very good approximation, corrections to the monopole-monopole Coulomb potential can be neglected when extracting the nuclear potentials for these systems.

One might immediately assume that similar corrections to the monopole-quadrupole and monopole-hexadecapole electric potentials in the region $R \gtrsim D_{min}$ are negligible because the monopole-monopole Coulomb potential dominates the potential part of the Hamiltonian in that region. Such an assumption is not justified on that basis (at least not without further investigation). Although the monopole-monopole Coulomb term dominates the radial momentum equation (see Eq. VI-8) and largely determines the values of the radial coordinate which enters into the terms in the torque equation (see Eq. VI-10), the effective $Q_0^{(2)}$ and $Q_0^{(4)}$ moments have a strong effect on the coupling to the torque equation. The leading term in the torque equation is that due to the monopole-quadrupole electric potential (until the radial coordinate becomes small enough that terms from the nuclear potential dominate).

Corrections to the monopole-quadrupole and monopole-hexadecapole electric interaction become necessary at larger values of R than for the monopole-monopole Coulomb potential. [As the surfaces overlap, changes in the charge density will have a greater effect on $Q_0^{(2)}$ and $Q_0^{(4)}$ because of the r^λ weighting in their definition (Eq. III-4).] To investigate these corrections note that the electric interaction between two charge distributions can be parametrized in terms of a double-folding integral of the individual charge distributions. Assuming axial symmetry, the

resulting expression can be expanded in terms of Legendre polynomials $P_\lambda(\cos \chi)$ as follows:

$$V(R,\chi) = V^{\lambda=0}(R) + V^{\lambda=2}(R)P_2(\cos \chi) + V^{\lambda=4}(R)P_4(\cos \chi) , \qquad \text{(B-4)}$$

where the $V^\lambda(R)$ give the radial dependence for each multipole in the expression. Equation B-4 can then be compared to the expansion in terms of the multipole moments $Q_0^{(\lambda)}$,

$$V(R,\chi) = \frac{Z_1 Z_2 e^2}{R} + \frac{Z_1 e^2 Q_0^{(2)}}{2R^3} P_2(\cos \chi) + \frac{Z_1 e^2 Q_0^{(4)}}{2R^5} P_4(\cos \chi) . \qquad \text{(B-5)}$$

Satchler (1980) has calculated such a double-folding potential for the $^{40}Ar + ^{160}Gd$ system for the case of a pure β_2 deformation of ^{160}Gd. Table B-2 contains the pertinent parameters for the deformed Fermi charge distribution

$$\rho = \frac{\rho_0}{1 + \exp\{[R - c(1 + \beta_2 Y_{20}(\theta,\phi))]/A\}} \qquad \text{(B-6)}$$

employed in the calculation. In Eq. B-6, ρ_0 is the mean central charge density, c is the half-density radius, A is a diffuseness parameter, and θ and ϕ are intrinsic polar and azimuthal angles. Figures B-1 through B-3 show comparisons of the λ = 0, 2, 4 radial dependences, respectively, determined with Eqs. B-4 and B-5. Note that for $R \geq D_{min}$ = 10.66 fm (Table B-1) corrections to the monopole-monopole potential can be ignored (as justified above). Note, however, that the terms for the monopole-quadrupole and monopole-hexadecapole electric interactions show

TABLE B-2

PARAMETERS USED IN THE DOUBLE-FOLDING CALCULATION
OF FIGURES B-1 THROUGH B-3

Nucleus	ρ_0 (fm^{-3})	c (fm)	A (fm)	β_2
^{40}Ar	0.1548	3.70	0.55	0.00
^{160}Gd	0.1430	6.243	0.52	0.35

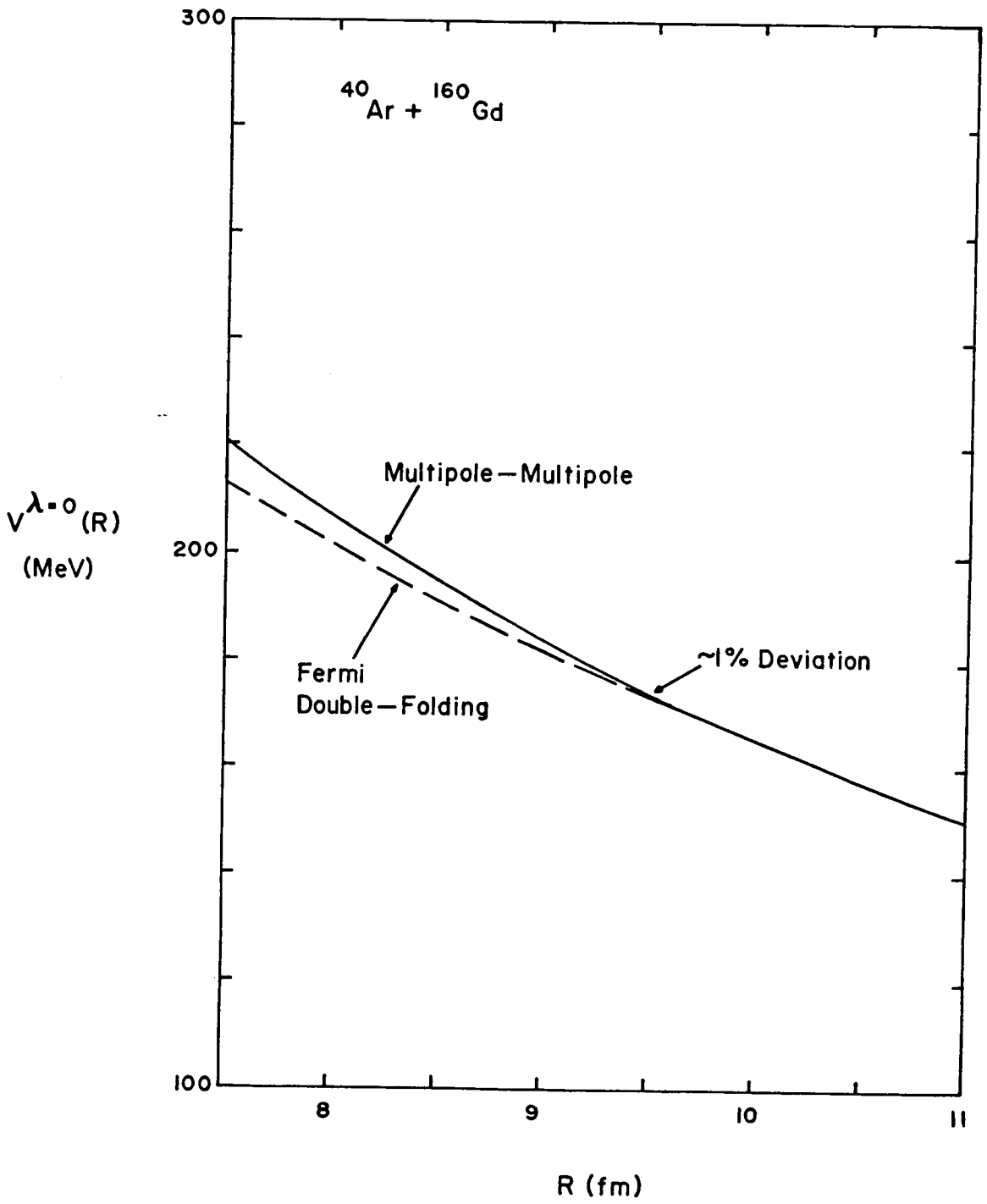


Figure B-1. Comparison of the $\lambda = 0$ radial dependence for the Fermi double-folding expansion (Eq. B-4) and the multipole-multipole expansion (Eq. B-5). The calculations are for the $^{40}Ar + ^{160}Gd$ system. Noticeable deviations do not occur until $R \lesssim 9.5$ fm.

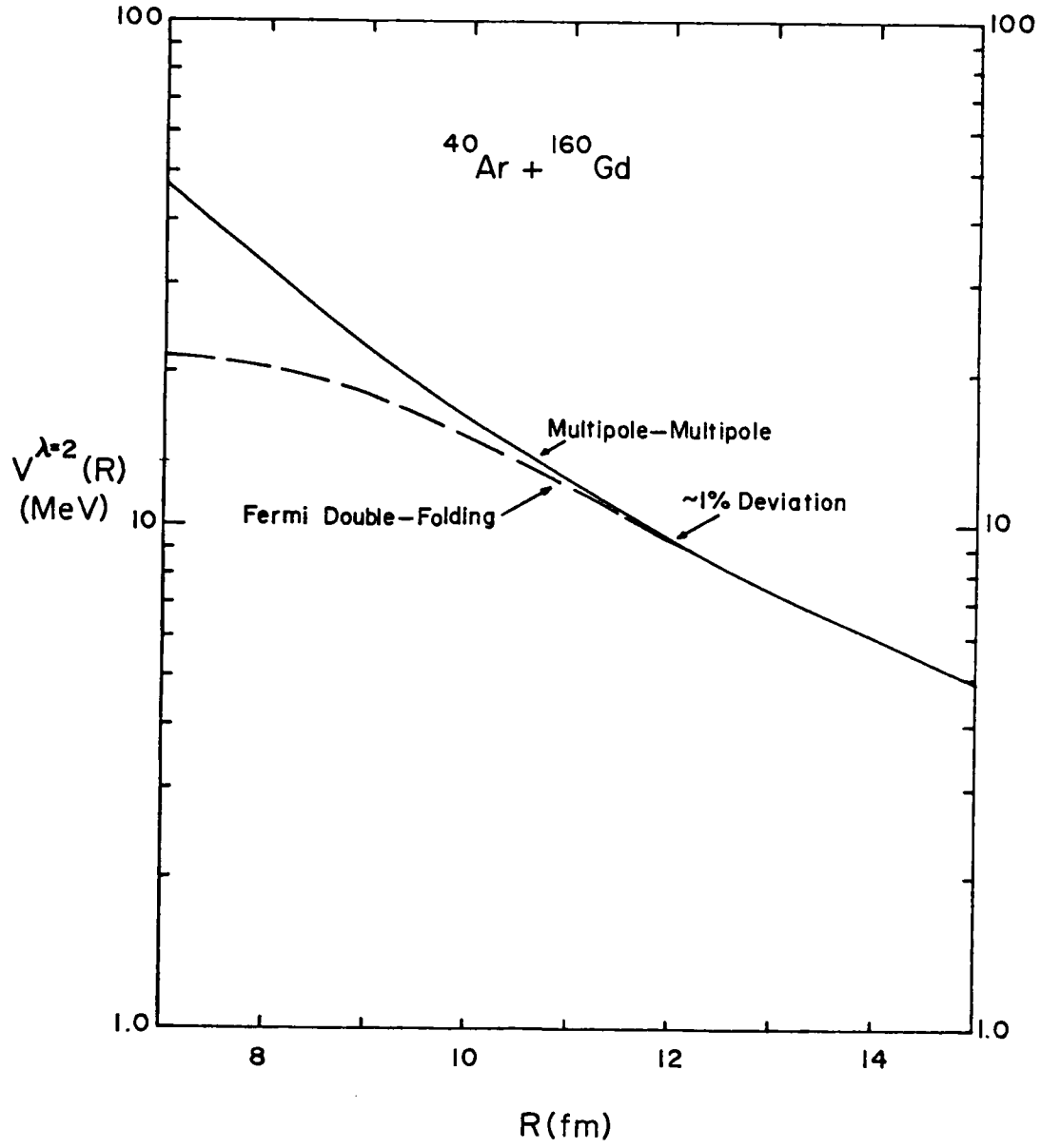


Figure B-2. The same as Figure B-1 for $\lambda = 2$. Note that deviations become noticeable for $R \lesssim 12$ fm, a larger radius than for the $\lambda = 0$ case.

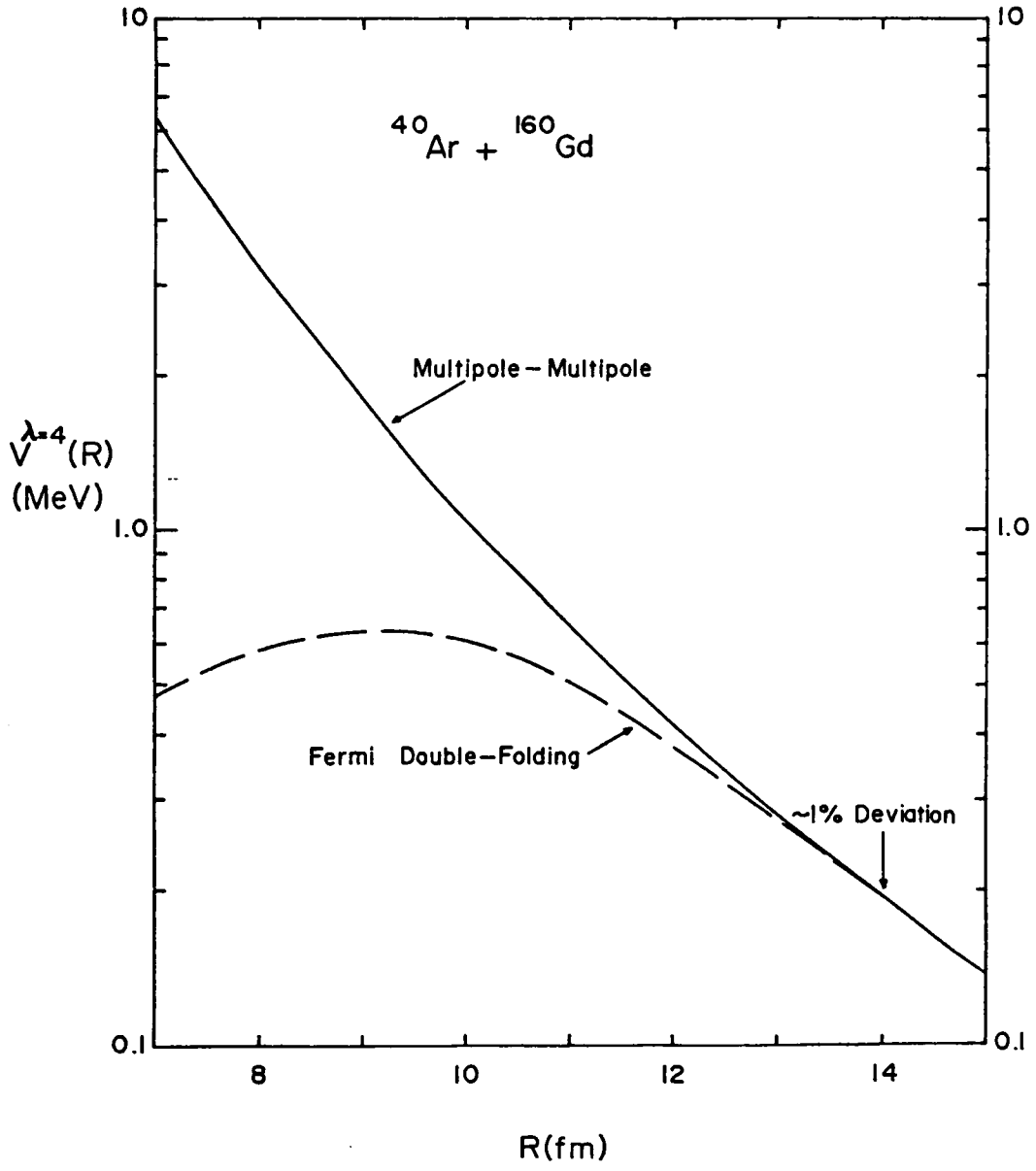


Figure B-3. The same as Figure B-1 for $\lambda = 4$. In this case, the deviations become noticeable for $R \lesssim 14$ fm, an even larger radius than for the $\lambda = 2$ case.

deviations which begin at $\sim$ 12 fm and $\sim$ 14 fm, respectively, and which are 4% and 27%, respectively, of the values at D_{min} = 10.66 fm for the multipole-multipole potentials. Because pure Coulomb inelastic excitation is extremely sensitive to relatively small changes in the effective $Q_0^{(2)}$ moment (and less so for the $Q_0^{(4)}$ moment), care must be taken to insure that corrections of the magnitudes indicated above do not become necessary before terms from the nuclear potential totally dominate the torque equation in the CNI region. Consider the ratios

$$\Delta_1 = \frac{\left(\frac{\bar{b}_2^R \exp(\rho r - \bar{R}(X))}{[1 + \exp(\rho r - \bar{R}(X))]^2} \right)}{\left(\frac{3\bar{q}_2}{\hat{r}^3} + \frac{5\bar{q}_4}{4\hat{r}^5} \right)} \tag{B-7}$$

$$\Delta_2 = \frac{\left(\frac{\bar{b}_4^R \exp(\rho \hat{r} - \bar{R}(X))}{[1 + \exp(\rho \hat{r} - \bar{R}(X))]^2} \right)}{\left(\frac{35\bar{q}_4}{8\,\hat{r}^5} \right)} \tag{B-8}$$

where all quantities are defined in Eq. E-9. Clearly, Δ_1 represents the ratio of the nuclear and electric cofactors of the sin(2X) term in the torque equation, while Δ_2 is a similar ratio for the sin(4X) term. Values of Δ_1 and Δ_2 were obtained by integrating the equations of motion for the systems studied. Typically, at those radii where the electric monopole-quadrupole and monopole-hexadecapole terms began to show deviations, $\Delta_1 \gtrsim 2$ and $\Delta_2 \gtrsim 3$. Thus, at those radii a 1-2% discrepancy in the electric interaction would be undetectable due to 10-15% uncertainties in the experimental nuclear potential. At radii near

D_{min}, $\Delta_1 >> 1$ and $\Delta_2 >> 1$, so that even the large uncertainties in the monopole-quadrupole electric potential can be ignored.

For the above reasons, no corrections in the electric interaction potential to account for charge overlap were included in this data analysis. If the need should arise to account for the effect of charge overlap, then the double-folding prescription of Mackintosh (1975), the analytic formulas for the Coulomb interaction between diffuse nuclear charge distributions of Krappe (1976), or the expressions involving limits of the Yukawa integral of Oberacker and Soff (1977) might be employed. However, for the analysis of data involving inelastic excitation of rare-earth target nuclei by ^{40}Ar projectiles in the CNI region, such complications appear needless, considering the current magnitudes of uncertainties expected for experimental nuclear potentials.

APPENDIX C

THICK TARGET KINEMATICAL RELATIONS AND THE CALCULATED BACKSCATTERED HEAVY-ION SPECTRUM

As discussed in Chapter V, if the beam energy is high enough to cause significant deviations from Rutherford scattering, the backscatter spectrum from the thick target must be calculated to properly determine N_B in Eq. V-1. In addition, the relation between energy in the particle detector and energy incident on the nucleus in the thick target is required in the data analysis. This appendix summarizes the basic equations required for these calculations.

The beam is incident on the thick target, loses energy passing through the target until encountering the scattering center, and is scattered back out of the target, again losing energy. The backscattered heavy ions will also lose energy in any electron suppression foil covering the annular detector. The energy of the heavy ion backscattered into the detector is given by the following relations:

$$E_{inc}(x,E_{lab}) = R^{-1}[R(E_{lab}) - x] \; ; \tag{C-1}$$

$$E_{back}(x,E_{lab}) = \left(\frac{A_p}{A_p + A_T}\right)^2 \left[\cos\theta + \sqrt{\left(\frac{A_T}{A_p}\right)^2 - \sin^2\theta}\right]^2 \times \left(E_{inc}(x,E_{lab}) - \frac{\bar{E}_{exc}}{2}\right) \; ; \tag{C-2}$$

$$E_{vac}(x,E_{lab}) = R^{-1}[R(E_{back}(x,E_{lab})) - \bar{X}(x)/\cos\theta] \; ; \qquad \text{(C-3)}$$

$$E_{det}(x,E_{lab}) = R^{-1}[R(E_{vac}(x,E_{lab})) - t/\cos\theta] \; . \qquad \text{(C-4)}$$

In Eqs. C-1 through C-4, E_{lab} is the beam energy, x is the effective penetration depth, E_{inc} is energy of the projectile incident on the target nucleus, R is the range of the projectile in the target material as a function of incident energy [from tables such as those of Northcliffe and Schilling (1970) and Hubert et al. (1978, 1980)], R^{-1} is the inverse function, A_p and A_T are the atomic mass numbers of the projectile and target nucleus, $\bar{E}_{exc}$ is the average rotational excitation energy of the deformed rotor in the collision, E_{vac} is the energy of the backscattered projectile when it leaves the target, t is the thickness of any foil covering the annular detector and E_{det} is the energy of the projectile which strikes the detector. In Eqs. C-2 through C-3, θ is the average scattering angle in the lab system defined by

$$\theta = \cos^{-1}\left[\frac{\cos\theta_{min} + \cos\theta_{max}}{2}\right] , \qquad \text{(C-5)}$$

where θ_{min} and θ_{max} are the minimum and maximum scattering angle subtended by the annular particle detector, respectively. In Eq. C-2 the term $E_{inc} - \bar{E}_{exc}/2$ represents an approximation to the incident energy of the projectile which allows for some average rotational excitation of the target nucleus. In Eq. C-3, $\bar{X}(x)$ is the effective emergent distance which in general depends on the inclination angle of the target.

For the 45° snout configuration used in the experiments described in Chapter V, Sayer (1968, Appendix D) has shown that

$$\bar{X}(x) = \frac{x}{\sqrt{1 - \tan^2 \theta}} . \qquad (C\text{-}6)$$

Because $\theta \approx 166°$ in the experimental configuration used in this work, $\bar{X}(x) \approx 1.033\ x$. Hence, the approximation

$$\bar{X}(x) \approx x \qquad (C\text{-}7)$$

was used in the data analysis described in Chapter V, introducing uncertainties in the energy assignments of $\lesssim 1\%$. Equations C-1 through C-4 define the relationship between E_{inc} and E_{det} shown in Figure V-6 (p. 74).

For an infinitesimally thick target and monoenergetic beam, flux conservation requires that the intensity $I(E_{inc})$ scattered at the scattering center is related to the intensity in the detector $I'(E_{det})$ by

$$I'(E_{det}) = I(E_{inc}) \frac{dE_{inc}}{dE_{det}} = \frac{N}{E_{inc}^2} \frac{dE_{inc}}{dE_{det}} \cdot \frac{1}{S(E_{inc})} , \qquad (C\text{-}8)$$

where in the second step approximate Rutherford scattering is assumed. The constant N depends on the beam flux and the projectile-target system via the relationship for the Rutherford differential cross section. $S(E_{inc})$ is the stopping power of the target material.

A thick target can be modeled as a juxtaposition of many layers of thin targets. In that case summation of the contributions from all layers accessible in the thick target yields

$$I'(E_{det}) \approx \int_0^{E_{lab}} \frac{N}{E_{inc}^2} \cdot \frac{A_0(E_0)\, e^{-[\alpha(E_0)(E_{inc}-E_0)]^2}}{S(E_{inc})} \frac{dE_{inc}}{dE_{det}}\, dE_0 \,, \tag{C-9}$$

where E_0 denotes the average energy incident on each layer in the target and the Gaussian factor is inserted to describe phenomenologically the spreading of the distribution in the scattering process, with the spreading dependent on E_0 which is related to depth of penetration. The Gaussian is normalized by

$$A_0(E_0) = \frac{\alpha(E_0)}{\sqrt{\pi}} \,, \tag{C-10}$$

where $\alpha(E_0)$ is the energy-dependent width parameter.

From Figure V-6 (p. 74), the relation between the detector energy E_{det} and incident energy E_{inc} may be parametrized nicely by a piecewise-quadratic form

$$E_{inc} = aE_{det}^2 + bE_{det} + c \,. \tag{C-11}$$

Substitution of Eq. C-11 into Eq. C-9 results in

$$I'(E_{det}) \approx \frac{N}{E_{inc}^2} \frac{(2aE_{det} + b)}{S(E_{inc})} \int_0^{E_{lab}} \frac{\alpha(E_0)\, e^{-[\alpha(E_0)(E-E_0)]^2}}{\sqrt{\pi}}\, dE_0 \,. \tag{C-12}$$

The Gaussian width factor $\alpha(E_0)$ is estimated by assuming that the energy spread of the beam incident on the face of the target is

proportional to the beam energy E_{lab} (where the constant of proportionality depends on the characteristics of the accelerator used) and that the spreading of the beam energy within the target may be described by a quadratic relation in the energy loss $(E_{lab} - E_0)$. Adding these contributions in quadrature

$$\frac{1}{\alpha(E_0)} \approx \sqrt{(c_1 E_{lab})^2 + [c_3(E_{lab} - E_0)^2 + c_2(E_{lab} - E_0)]^2} , \quad \text{(C-13)}$$

where the constants c_1, c_2, and c_3 and the overall normalization N in Eq. C-9 are to be fixed phenomenologically. Because $S(E_{inc})$ is approximately constant over the range of incident energies sampled by the rare-earth targets used in the experiments, in the fits to the backscattered heavy-ion spectra used in the data analysis $S(E_{inc})$ was subsumed into the constant N with the assurance that the remaining parameters (c_1, c_2, and c_3) would account for any weak dependence on energy. Figure C-1 shows some examples of using this approach to calculate the thick-target backscatter spectrum.

More sophisticated treatments of the straggling process are discussed in the excellent monograph by H. Schmidt-Böcking (1978). Such treatments might become useful with the advent of better measurements for the stopping powers of heavy ions in materials and a more complete understanding of straggling processes. However, for precise determination of the ion-ion interaction potentials thin targets should be used.

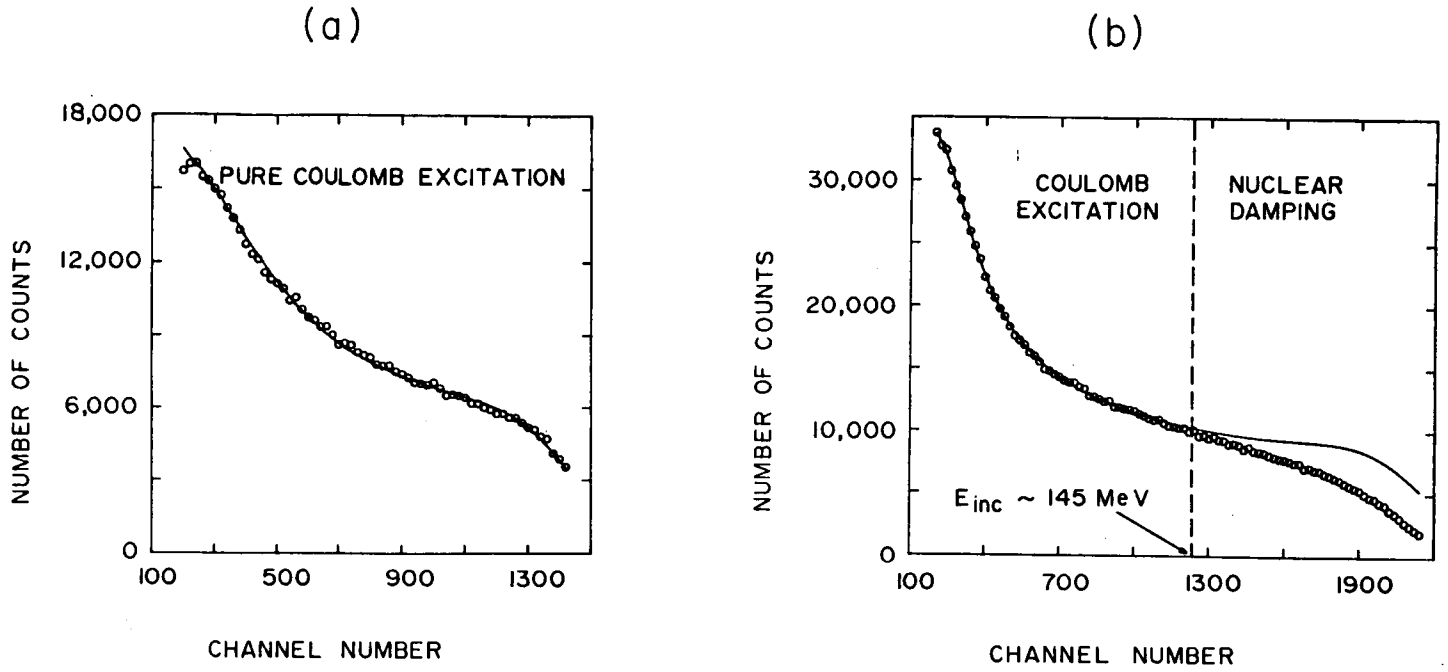


Figure C-1. Calculations of backscattered heavy-ion spectra for $^{40}Ar + ^{160}Gd$. Approximate Rutherford scattering as described in Appendix C was used. In (a) E_{LAB} = 122 MeV so that only Coulomb excitation (approximately Rutherford scattering) is possible over the energy range sampled. In (b) E_{LAB} = 160.7 MeV so that damping due to the imaginary part of the nuclear potential is important for energies greater than ~ 145 MeV, and the experimental data points fall below the curve calculated assuming approximate Rutherford scattering. As discussed in Chapter V the experimental excitation probabilities are determined with respect to the Rutherford cross section (calculated curve), normalized to the data in the pure Coulomb excitation (low energy) region.

APPENDIX D

SAFE-ENERGY FORMALISM

Neese and Guidry (1981) have devised a simple one-parameter formula which can be used to determine the "safe energy" for heavy-ion Coulomb excitation experiments involving deformed nuclei. This formula accounts for both projectile and target nucleus deformation effects and reproduces the onset of Coulomb-nuclear interference effects for a broad range of heavy-ion systems. [Note however, that the formula obtained by Neese and Guidry (1981) is not applicable to Coulomb reorientation experiments which involve extremely small effects so that nuclear forces must be excluded more rigorously. Spear et al. (1978) provide a prescription which is appropriate for reorientation experiments.]

In this approach the safe energy is defined to be that energy above which, for a given scattering angle, the differential cross section of any process in question deviates by $\geq$ 5% from that expected for pure Coulomb excitation. For excitation of rotational collective states, in the classical limit, this criterion is equivalent to averaging over all possible orientations of the rotor in the collision. Figure D-1 illustrates this concept for the general case where both collision partners exhibit axially symmetric deformations. Averaging over orientations sweeps out the two spheres indicated in Figure D-1. The scattering and excitation are assumed to be pure Coulomb and "safe" if the two spheres do not touch.

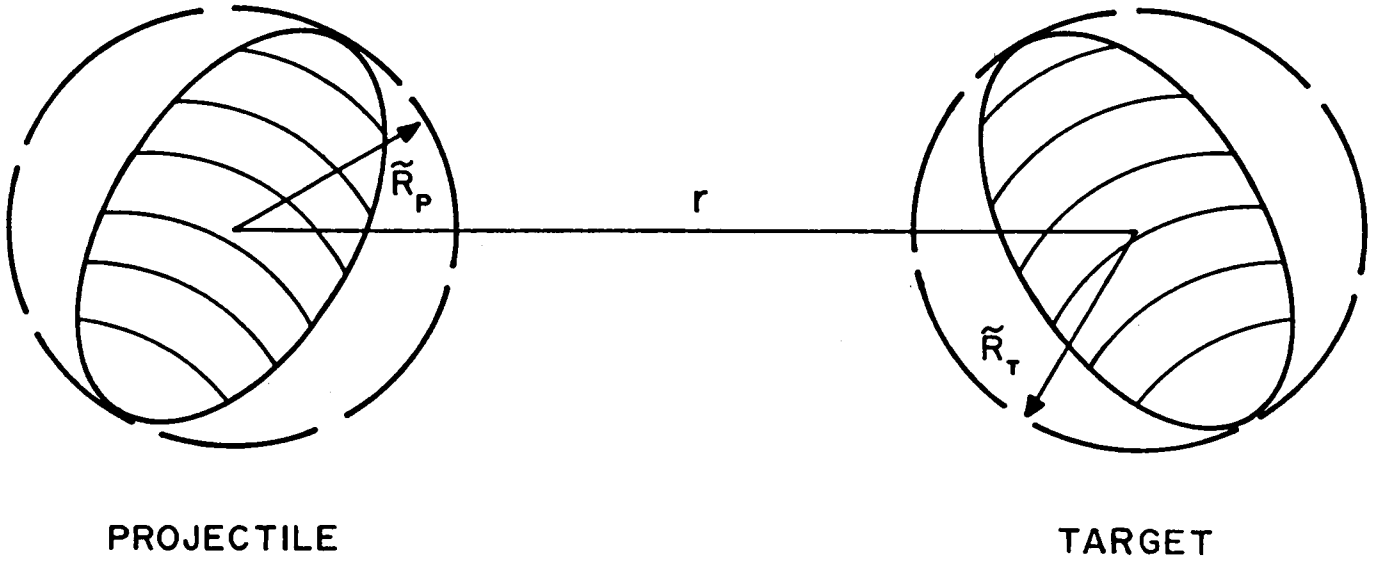


Figure D-1. Schematic diagram of the model used to construct the safe-energy formula. The energy is considered safe if the separation r remains sufficiently large that the spheres defined by the dashed lines never touch during the scattering event. In this figure $\tilde{R} = \tilde{R}_0 A^{1/3}$.

Assuming that the trajectory for which nuclear forces are first felt is approximately Rutherford, one may define the safe energy E^S_{LAB} by

$$E^S_{LAB} = B/\tilde{R}_0 \ , \tag{D-1}$$

where

$$B = 0.721 \ Z_p Z_t \left(\frac{(A_p + A_t)\left[1 + \csc\left(\frac{\theta_{CM}}{2}\right)\right]}{A_t[(1 + \gamma_p) A_p^{1/3} + (1 + \gamma_t) A_t^{1/3}]} \right) \ ; \tag{D-2}$$

$$\gamma = \text{Max} \left[\beta_2 Y_{20}(\chi) + \beta_4 Y_{40}(\chi)\right] \ ; \tag{D-3}$$

$$\theta_{CM} = \theta_{LAB} + \sin^{-1}\left(\frac{A_p}{A_t} \sin \theta_{LAB}\right) \ . \tag{D-4}$$

In these formulas the subscripts p and t denote projectile and target quantities with Z the atomic number and A the atomic mass number. The scattering angle in the center-of-mass system and in the laboratory system is denoted by θ_{CM} and θ_{LAB}, respectively. The $Y_{\lambda 0}$ are spherical harmonics of order λ and the β_λ are deformation parameters. The angle χ is a polar angle in the intrinsic frame.

Therefore the safe energy is determined by a single parameter $\tilde{R}_0$, assuming that approximate deformation parameters are known for the colliding ions. Figure D-2 shows a least-squares fit with Eq. D-1 to a number of heavy-ion systems using values of β_2 and β_4 commonly available in the literature. The best-fit value of the radius constant is $\tilde{R}_0$ = 1.506 ± 0.015 fm, and this reproduces the safe energy for a large amount of experimental data, with ions ranging from ^{16}O to ^{86}Kr as projectiles.

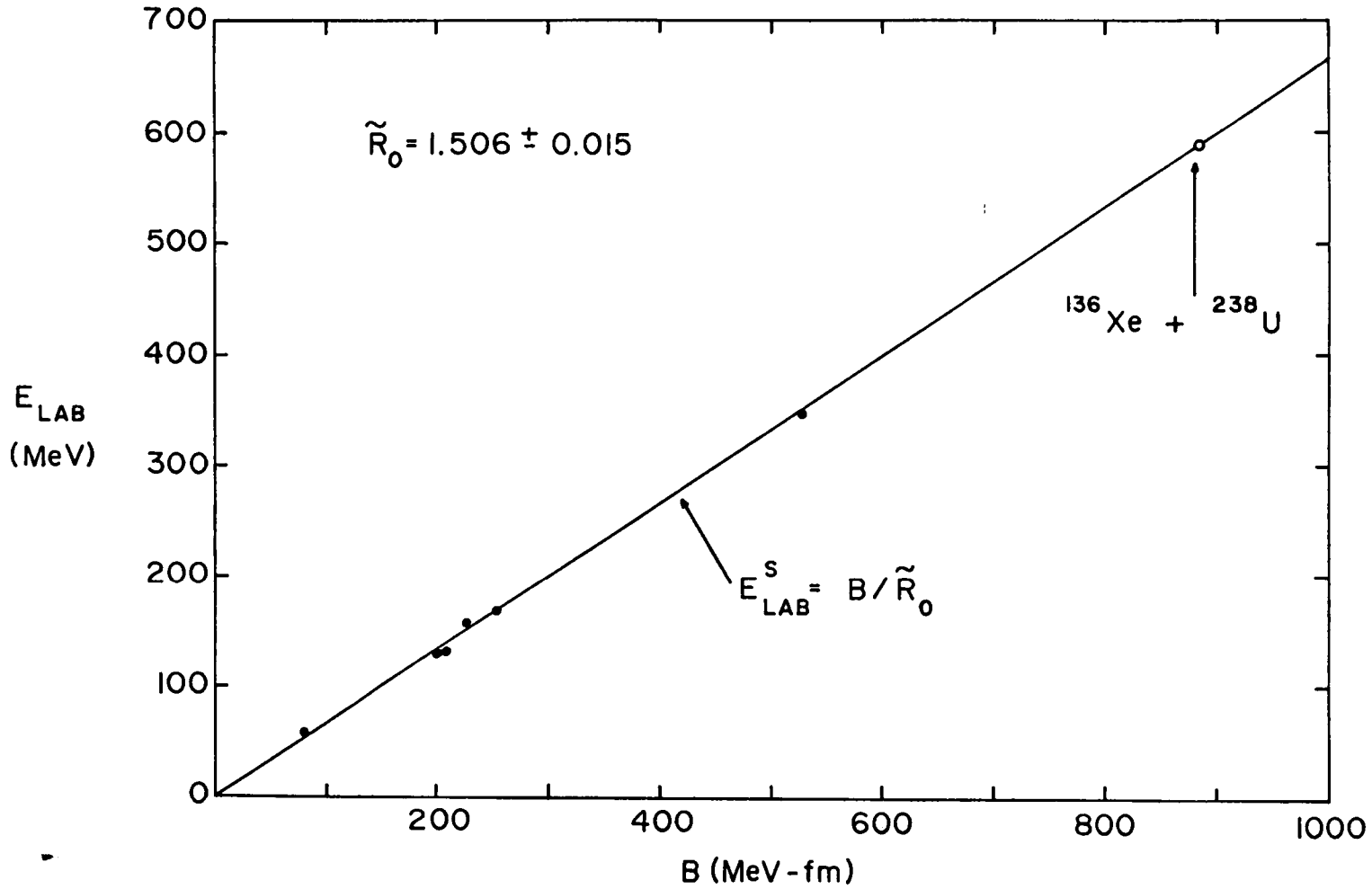


Figure D-2. Least-squares fit of some heavy-ion scattering data to Eq. D-1. The data points (closed circles) are from the work reported in this dissertation and the work reported by Guidry et al. (1978a). A prediction of the safe energy for backward scattering in the $^{136}Xe + ^{238}U$ system is indicated by the open circle.

An $\tilde{R}_0$ value $\sim$1.4-1.5 fm is common in diffraction models for sharp cutoff spherical nuclei. Therefore, this analysis suggests that, in determining safe energies for Coulomb excitation of rotational states, deformed nuclei behave approximately as sharp diffracting spheres with a diameter comparable to the length of the longest deformation axis.

The above analysis assumes that the ions move on classical trajectories. Therefore, quantum fluctuations of the order of the de Broglie wavelength for relative motion may be expected in the extracted safe distance. Such effects could play some role for lighter ions. For heavier ions such fluctuations can be ignored.

Another assumption in the derivation of Eq. D-1 is that the deflection function is monotonic—i.e., a single classical trajectory scatters to a given angle. If multiple trajectories scatter to the same angle without appreciable damping, the differential cross section may exhibit nuclear effects of sizable magnitude at even lower energies than those predicted by Eq. D-1, due to the sensitivity of the trajectory interference to subtle variations in the potential. In practice, this means that care should be exercised in using Eq. D-1 if one is dealing with forward scattering in the CM system.

Hence, Eq. D-1 with $\tilde{R}_0$ = 1.506 fm may be used to determine safe energies for multiple Coulomb excitation experiments. Although Coulomb-nuclear interference data for ions more massive than Kr is not yet available, the simple physical content of the model and the quality of the fit in Figure D-2 suggest that Eq. D-1 and Figure D-2 may be used for estimations involving more massive ions such as Xe and Pb (e.g., the $^{136}Xe + ^{238}U$ system shown in Figure D-2).

APPENDIX E

FEATURES OF THE CLSM COMPUTER CODE KULEXA

In Section III of Chapter VI, the coupled equations of motion for the model system were listed along with the corresponding initial conditions. These equations can be cast in dimensionless form by use of the dimensionless dynamical quantities $\hat{r}$, $\hat{p}_r$, $\hat{I}$, and $\hat{t}$ defined by

$$\hat{r} = \frac{r}{a} ; \tag{E-1}$$

$$\hat{p}_r = \frac{p_r}{m v_0} ; \tag{E-2}$$

$$\hat{I} = \frac{p_\chi}{\hbar} ; \tag{E-3}$$

$$\hat{t} = \frac{v_0 \, t}{a} . \tag{E-4}$$

In Eqs. E-1 through E-4, a is defined in Eq. VI-18, m is the reduced mass of the system, and v_0 is the initial relative velocity in the asymptotic region. Note that the dynamical variable χ is already dimensionless (its natural unit is the radian). The dimensionless Hamiltonian

$$\hat{H}(\hat{r},\hat{p}_r,\chi,\hat{I}) = \frac{H(r,p_r,\chi,p_\chi)}{m v_0^2} \tag{E-5}$$

can be written explicitly via substitution of the expressions for $\hat{r}$, $\hat{p}_r$, and $\hat{I}$.

The dimensionless equations of motion are:

$$\dot{\hat{r}} = \hat{p}_r \ ; \tag{E-6}$$

$$\dot{\hat{p}}_r = \frac{\hat{I}^2}{\eta_o \hat{r}^3} + \frac{1}{\hat{r}^2} + \frac{\bar{Q}_{A2}\bar{P}_2(\cos\chi)}{\hat{r}^4} + \frac{\bar{Q}_{A4}\bar{P}_4(\cos\chi)}{\hat{r}^6}$$

$$+ \frac{\kappa_{44} + \bar{\kappa}_{4B}\bar{P}_2(\cos\chi)}{\hat{r}^5} + \frac{\kappa_{66}}{\hat{r}^7} + \bar{q}_{NO}\frac{\exp[\rho\hat{r} - \bar{R}(\chi)]}{\{1 + \exp[\rho\hat{r} - \bar{R}(\chi)]\}^2} \ ; \tag{E-7}$$

$$\dot{\chi} = \left(\frac{\xi}{3} + \frac{1}{\eta_o \hat{r}^2}\right)\hat{I} \ ; \tag{E-8}$$

$$\dot{\hat{I}} = \left[\frac{Q_{B2}}{\hat{r}^3} + \frac{Q_{B24}}{\hat{r}^5}\right]\sin(2\chi) + \frac{Q_{B4}}{\hat{r}^5}\sin(4\chi) + \frac{\kappa_{IP}}{\hat{r}^4}\sin(2\chi)$$

$$+ [\bar{b}_2^R \sin(2\chi) + \bar{b}_4^R \sin(4\chi)]$$

$$\times \frac{\exp[\rho\hat{r} - \bar{R}(\chi)]}{\{1 + \exp[\rho\hat{r} - \bar{R}(\chi)]\}^2} \ . \tag{E-9}$$

The action equation (Eq. III-8) is replaced by

$$\hat{\Phi} = -[\eta_o \hat{r}\,\dot{\hat{p}}_r + \chi\,\dot{\hat{I}}] \ . \tag{E-10}$$

In Eqs. E-6 through E-10 the dot symbolizes differentiation with respect to the dimensionless time $\hat{t}$. Other parameters in these equations are defined as follows:

$$\eta_0 = \frac{Z_P Z_T e^2}{\hbar v_0} \quad \text{(Sommerfeld parameter)} ; \tag{E-11}$$

$$\bar{Q}_{A2} = \frac{3 Z_P Q_0^{(2)} e^2}{8\hbar v_0 \eta_0 a^2} ; \tag{E-12}$$

$$\bar{Q}_{A4} = \frac{5 Z_P Q_0^{(4)} e^2}{128\hbar v_0 \eta_0 a^2} ; \tag{E-13}$$

$$\kappa_{44} = - \frac{4k_1(1 + k_2)}{m v_0^2 a^4} ; \tag{E-14}$$

$$\bar{\kappa}_{4B} = - \sqrt{\frac{5}{\pi}} \frac{k_1 k_2 \beta_2}{m v_0^2 a^4} ; \tag{E-15}$$

$$\kappa_{66} = - \frac{6k_4}{m v_0^2 a^6} ; \tag{E-16}$$

$$\bar{q}_{NO} = - \frac{V_0}{a_R} \frac{a^2}{\eta_0 \hbar v_0} ; \tag{E-17}$$

$$\rho = \frac{a}{a_R} ; \tag{E-18}$$

$$\xi = \frac{3\hbar^2 \eta_0}{m v_0^2 d} \quad \text{(adiabaticity parameter)} ; \tag{E-19}$$

$$Q_{B2} = \frac{3Z_P Q_0^{(2)} e^2}{4\hbar v_0 a^2} ; \qquad \text{(E-20)}$$

$$Q_{B24} = \frac{5Z_P Q_0^{(4)} e^2}{16\hbar v_0 a^2} ; \qquad \text{(E-21)}$$

$$Q_{B4} = \frac{7}{2} Q_{B24} ; \qquad \text{(E-22)}$$

$$\kappa_{IP} = \frac{3\eta_0}{4} \bar{\kappa}_{4B} ; \qquad \text{(E-23)}$$

$$\bar{b}_2^R = \frac{3\eta_0 \bar{q}_{NO}}{4a\sqrt{\pi}} r_0^R A_T^{1/3} (\sqrt{5}\, \tilde{\beta}_2 + \frac{5}{4} \tilde{\beta}_4) ; \qquad \text{(E-24)}$$

$$\bar{b}_4^R = \frac{105\eta_0 \bar{q}_{NO} r_0^R A_T^{1/3} \tilde{\beta}_4}{32a\sqrt{\pi}} . \qquad \text{(E-25)}$$

All parameters not explicitly defined above are defined in Chapter III, Chapter VI, and Appendix A.

Note that, in general, the polarization potential deformation parameter β_2 (see Eq. E-15) can be different from the potential deformation parameter $\bar{\beta}_2$ (see Eq. VI-6). The fits to the experimental excitation functions reported in Section IV of Chapter VI were made with β_2 set equal to experimental measurements of the nuclear quadrupole deformation parameter available in the literature.

The functions $\bar{P}_2(\cos \chi)$, $\bar{P}_4(\cos \chi)$, and $\bar{R}(\chi)$ specified in Eqs. E-7 and E-9 are defined as follows:

$$\bar{P}_2(\cos\chi) = 3\cos(2\chi) + 1 \; ; \tag{E-26}$$

$$\bar{P}_4(\cos\chi) = 35\cos(4\chi) + 20\cos(2\chi) + 9 \; ; \tag{E-27}$$

$$\bar{R}(\chi) = R_{AUX} + \tilde{\beta}_2 \bar{P}_2(\cos\chi) + \tilde{\beta}_4 \bar{P}_4(\cos\chi) \; , \tag{E-28}$$

where

$$R_{AUX} = \frac{r_0^R}{a_R}\left[A_P^{1/3} + A_T^{1/3}\left(1 - \frac{\bar{\beta}_2^2 + \bar{\beta}_4^2}{4\pi}\right)\right] \; ; \tag{E-29}$$

$$\tilde{\beta}_2 = \frac{r_0^R A_T^{1/3} \bar{\beta}_2}{8a_R}\sqrt{\frac{5}{\pi}} \; ; \tag{E-30}$$

$$\tilde{\beta}_4 = \frac{3r_0^R A_T^{1/3} \bar{\beta}_4}{128a_R\sqrt{\pi}} \; . \tag{E-31}$$

Care should be taken to avoid confusion between the parameters β_2, $\bar{\beta}_2$, $\bar{\beta}_4$, $\tilde{\beta}_2$, and $\tilde{\beta}_4$.

The absorption factor (Eq. VI-11) was calculated from the relation

$$A = \exp(-\mu) \; , \tag{E-32}$$

where

$$\dot{\mu} = \eta_0 \hat{\dot{p}}_r \, \mathfrak{Im}(Z) \; . \tag{E-33}$$

In Eq. E-33, the complex variable Z is defined by

$$Z = \text{sign}(\hat{p}_r)\sqrt{\hat{p}_r^{\,2} + i\,\hat{W}}\ , \tag{E-34}$$

where

$$\hat{W} = -\frac{2W_0\, f_I(r,\chi)}{mv_0^{\,2}} \tag{E-35}$$

with $f_I(r,\chi)$ defined in Eq. VI-5.

This somewhat exotic parametrization of the equations of motion was necessary for numerical reasons. Because the equations of motion are integrated numerically, repetitious calculations must be avoided in the derivative subroutine to improve the computational speed. The above parametrization approximately halved the computation time.

The initial conditions for the integration, in terms of the dimensionless variables, were

$$\hat{r} = 60\ ; \tag{E-36}$$

$$\hat{p}_r = -\sqrt{1 - \frac{2}{60}} = -\sqrt{\frac{29}{30}}\ ; \tag{E-37}$$

$$\chi = \chi_0\ , \tag{E-38}$$

where $\chi_0\ \varepsilon[-5°,95°]$ in 5° steps;

$$\hat{I} = 0\ ; \tag{E-39}$$

$$\Phi = 0\ ; \tag{E-40}$$

$$\mu = 0\ . \tag{E-41}$$

Thus, for each projectile energy the final dynamical quantities were calculated as table functions of the 21 initial orientation angles.

These functions were approximated by piecewise application of Newton's six-point forward difference formula (Abramowitz and Stegun, 1972). The roots of the quantum number function (where $I(\chi_0) = I + 1/2$) and χ_{max}, the value of χ_0 corresponding to the maximum of the quantum number function, were obtained by the interval-halving technique.

An important modification of the root-search subroutine must be mentioned, because it has a bearing on the excitation probabilities calculated at energies where the nuclear potential has a strong influence on the quantum-number function, especially at low angles. As the projectile energy increases, the quantum-number function begins to show a steep negative dip for low values of χ_0 because of the strong nuclear countertorque. As the projectile energy is increased further, the quantum-number function often exhibits some very large amplitude oscillations at low angles. Because of this behavior, more than two roots can be found for a given spin state (most notably for the low-spin states). The version of the CLSM formalism employed in this work was designed to handle at most two roots for classically allowed transitions and one for classically forbidden transitions. However, to a good approximation, the roots in the anomalous region of the quantum-number function make a negligible contribution to the excitation probabilities for three reasons.

1. The $\sin \bar{\chi}_k$ term in the numerator of the definition of the probability amplitudes $\bar{p}_k$ (Eq. III-9) is small for small values of $\bar{\chi}_k$.

2. The slope of the quantum-number function which appears in the denominator of Eq. III-9 is very large for the roots in the anomalous region.

3. Because of the strong influence of the nuclear force in the anomalous region, the damping factor (Eq. E-32) suppresses contributions from such roots.

Logic was incorporated into KULEXA's root-search subroutine to discriminate against roots in the anomalous region and to ignore them in the calculation of the final excitation probabilities. The actual calculation of the excitation probabilities made use of an approximate form of Eq. III-7, in which

$$|\mathrm{Ai}'(-\xi)| \approx |\sqrt{\xi}\ \mathrm{Bi}(-\xi)| \ , \qquad \text{(E-42)}$$

where Bi is the Airy function of second kind and ξ is defined in Eq. III-10. For cases in which this term is significant in Eq. III-7, the approximation (Eq. E-42) is excellent (Massmann, 1975).

VITA

Richard Earl Neese was born in Sumter, South Carolina, on March 12, 1953. Because of his father's career in the United States Air Force, he spent his early years in a variety of places: South Carolina, France, England, Minnesota, South Carolina (a second time), and Georgia. In 1971 he graduated second in his class from Valdosta High School in Valdosta, Georgia. He attended the Georgia Institute of Technology as a National Merit Scholar and was graduated magna cum laude with a Bachelor of Science degree in Physics in the summer of 1975. He was awarded a Georgia Institute of Technology Presidential Fellowship and began graduate study in physics. In the summer of 1976 he was awarded a Master of Science degree in Physics from Georgia Tech. He then transferred to The University of Tennessee, Knoxville, to work toward a Doctor of Philosophy degree with a major in physics.

He is a member of the American Physical Society, Phi Kappa Phi, and Sigma Pi Sigma. He is a former president of The University of Tennessee chapter of Sigma Pi Sigma.

The author is married to the former Kathy-Jo Stackley of Hazlehurst, Georgia.